

Hydrologic controls on vegetation: from leaf to landscape

by

Giulia Vico

Department of Civil and Environmental Engineering  
Duke University

Date: \_\_\_\_\_

Approved:

\_\_\_\_\_  
Amilcare Porporato, Supervisor

\_\_\_\_\_  
John D. Albertson

\_\_\_\_\_  
Gabriel G. Katul

\_\_\_\_\_  
Miguel A. Medina

\_\_\_\_\_  
Sari Palmroth

Dissertation submitted in partial fulfillment of  
the requirements for the degree of Doctor  
of Philosophy in the Department of  
Civil and Environmental Engineering in the Graduate School  
of Duke University

2009

ABSTRACT

Hydrologic controls on vegetation: from leaf to landscape

by

Giulia Vico

Department of Civil and Environmental Engineering  
Duke University

Date: \_\_\_\_\_

Approved:

\_\_\_\_\_  
Amilcare Porporato, Supervisor

\_\_\_\_\_  
John D. Albertson

\_\_\_\_\_  
Gabriel G. Katul

\_\_\_\_\_  
Miguel A. Medina

\_\_\_\_\_  
Sari Palmroth

An abstract of a dissertation submitted in partial fulfillment of  
the requirements for the degree of Doctor  
of Philosophy in the Department of  
Civil and Environmental Engineering in the Graduate School  
of Duke University

2009

Copyright by  
Giulia Vico  
2009

## **Abstract**

Topography, vegetation, nutrient dynamics, soil features and hydroclimatic forcing are inherently coupled, with feedbacks occurring over a wide range of temporal and spatial scales. Vegetation growth may be limited by soil moisture, nutrient or solar radiation availability, and in turn influences both soil moisture and nutrient balances at a point. These dynamics are further complicated in a complex terrain, through a series of spatial interactions. A number of experiments has characterized the feedbacks between soil moisture and vegetation dynamics, but a theoretical framework linking short-term leaf-level to interannual plot-scale dynamics has not been fully developed yet. Such theory is needed for optimal management of water resources in natural ecosystems and for agricultural, municipal and industrial uses. Also, it complements the current knowledge on ecosystem response to the predicted climate change.

In this dissertation, the response of vegetation dynamics to unpredictable environmental fluctuations at multiple space-time scales is explored in a modeling framework from sub-daily to interannual time scales. At the hourly time scale, a simultaneous analysis of photosynthesis, transpiration and soil moisture dynamics is carried out to explore the impact of water stress on different photosynthesis processes at the leaf level, and the overall plant activity. Daily soil moisture and vegetation dynamics are then scaled up to the growing season using a stochastic model accounting for daily

to interannual hydroclimatic variability. Such a stochastic framework is employed to explore the impact of rainfall patterns and different irrigation schemes on crop productivity, along with their implications in terms of sustainability and profitability. To scale up from point to landscape, a probabilistic representation of local landscape features (i.e., slope and aspect) is developed, and applied to assess the effects of topography on solar radiation. Finally, a minimalistic ecosystem model, including soil moisture, vegetation and nutrient dynamics at the year time scale, is outlined; when coupled to the proposed probabilistic topographic description, the latter model can serve to assess the relevance of spatial interactions and to single out the main biophysical controls responsible for ecohydrological variability at the landscape scale.

# Contents

Abstract .....	iv
List of Tables .....	ix
List of Figures .....	x
Acknowledgments .....	xvii
1 Introduction.....	1
2 Modelling C <sub>3</sub> and C <sub>4</sub> photosynthesis under water-stressed conditions .....	6
2.1 Introduction.....	6
2.2 Model formulation .....	8
2.2.1 Metabolic limitations to photosynthesis under drought.....	10
2.2.2 Diffusive limitations to photosynthesis under drought .....	19
2.3 Results and discussion.....	23
2.3.1 CO <sub>2</sub> assimilation rate and leaf water potential.....	26
2.3.2 Soil moisture dry-down.....	31
2.4 Conclusions .....	34
3 Traditional and micro-irrigation with stochastic soil moisture .....	36
3.1 Introduction.....	36
3.2 Model formulation .....	40
3.2.1 Rainfed agriculture (no irrigation).....	44
3.2.2 Continuous irrigation (modern micro-irrigation) .....	47
3.2.3 Concentrated applications (traditional irrigation) .....	49

3.3	Constant losses under well-watered conditions .....	52
3.3.1	Soil moisture probability function at steady state .....	52
3.3.2	Mean soil water balance and required irrigation volumes .....	57
3.3.3	Frequency of irrigation .....	61
3.3.4	Comparison of irrigation schemes for different crops and climatic conditions 62	
3.4	Discussion and conclusions .....	66
4	From rainfed agriculture to stress-avoidance irrigation: optimizing crop yield and net profit under intra- and inter-annual stochastic hydrologic variability.....	68
4.1	Introduction.....	68
4.2	Model formulation .....	71
4.2.1	Soil water balance.....	71
4.2.2	Generalized traditional irrigation.....	76
4.3	Average crop yield .....	82
4.3.1	Crop water productivity functions.....	82
4.3.2	Economic analysis .....	86
4.4	Interannual variability of crop yield.....	91
4.4.1	Interannual variability of rainfall amount and timing.....	91
4.4.2	Impact of rainfall interannual variability on crop yield and choice of irrigation scheme .....	92
4.5	Discussion and conclusions .....	95
5	Probabilistic description of topographic slope and aspect.....	98
5.1	Introduction.....	98

5.2	Theory .....	103
5.2.1	Definitions and preliminaries.....	103
5.2.2	Slope.....	108
5.2.3	Aspect .....	111
5.3	Models of derivatives of elevation.....	114
5.4	Distributions of slope.....	119
5.5	Distributions of aspect.....	123
5.6	Statistics of solar radiation over the landscape .....	127
5.7	Conclusions .....	133
6	Towards a spatially-implicit minimalistic model of ecosystem dynamics .....	136
6.1	Ecosystem dynamics and the role of topography.....	136
6.2	Minimalistic model coupling water, nitrogen and vegetation dynamics.....	141
6.2.1	Soil water balance.....	142
6.2.2	Vegetation dynamics .....	143
6.2.3	Soil nutrient dynamics.....	144
6.3	Upscaling to the landscape.....	146
7	Conclusions and future developments.....	149
Appendix A.	CO <sub>2</sub> assimilation model .....	153
Appendix B.	Soil water balance and transpiration flux in the plant.....	158
Appendix C.	Hydroclimatic fluctuations and interannual ecosystem productivity	162
References	.....	174
Biography	.....	195

## List of Tables

Table 2.1: Parameter values common to C <sub>3</sub> and C <sub>4</sub> functional types. ....	13
Table 2.2: Species-specific parameters. Simulations relative to <i>Amarathus retroflexus</i> and <i>Panicum coloratum</i> are performed with the same parameters as <i>Sorghum bicolour</i> . ....	17
Table 5.1: Summary of parameters and results relative to the four case studies. As detailed in the text, parameters $b_x$ and $b_y$ in Eqs. (58) and (59) are equal to $\mu_{\hat{\sigma}_x, h}$ and $\mu_{\hat{\sigma}_y, h}$ respectively. The relative entropy is estimated from the observed aspect field using 64 partitions. ....	103

## List of Figures

Figure 2.1: Impact of leaf water potential,  $\psi_L$ , on two key metabolic processes for C<sub>3</sub> and C<sub>4</sub> species: a) maximum carboxylation rate,  $V_{c,max}$ ; b) relative activity of PEP carboxylase,  $\eta_P(\psi_L)$ . Experimental data (symbols) are fitted to the respective vulnerability curves (Eq. (2); Table 2.1 and Table 2.2). Source of data: *Helianthus annuus* L.: Tezara et al. (1999, 2002; see text for details); *Saccharum* sp.: Du et al. (1996); *Sorghum bicolor* L. cultivars (filled box: 1063 ICSV; filled triangles, MIGSOR): ContourAnsel et al. (1996)..... 12

Figure 2.2: Impact of leaf water potential,  $\psi_L$ , on photochemical quantum yield of PSII,  $\phi_{PSII}(\psi_L)$  (Eq. (2)): experimental data (symbols) and fitted vulnerability curves (Table 2.2) for a) two C<sub>3</sub> species, and b) four C<sub>4</sub> species (in this case, the line represents the result of fitting all the point together). Source of data: a) Lu and Zhang (1998; filled triangles), Lu and Zhang (1999; open triangles), Pankovic et al. (1999; boxes); b) Ghannoum et al. (2003). ..... 16

Figure 2.3: Normalized C<sub>3</sub> assimilation rate as a function of leaf water potential when the different limitations to photosynthesis are gradually added: water-stress reduced stomatal conductance (Eq. (4)) but infinite mesophyll conductance ( $\alpha_m \gg 1$ ) and no metabolic limitations (dashed line), stomatal and mesophyll conductances only (diffusive limitation; dash-dotted line), and diffusive and metabolic limitations (full model; solid line). The species-specific parameters refer to *Helianthus annuus* (Table 2.2); all the other parameters are listed in Table 2.1 environmental conditions are as those described in Gimenez et al. (1992). ..... 25

Figure 2.4: Normalized C<sub>3</sub> assimilation rate as a function of leaf water potential,  $\psi_L$ , for a range of parameters of the stomatal and mesophyll conductance models: a) the decrease rate of  $R_c$  with  $\psi_L$ ,  $\chi$  (Eq. (4)), varies in the range 0 (i.e., Norman model; dashed line) to 0.16 MPa<sup>-1</sup>; b) the ratio between mesophyll and stomatal conductances,  $\alpha_m$ , varies in the range 1.15 to 4.15, and assimilation is normalized with respect to values obtained for  $\alpha_m \rightarrow \infty$  (dashed line). The species-specific parameters refer to *Helianthus annuus* (Table 2.2); all the other parameters are listed in Table 2.1; environmental conditions are as those described in Gimenez et al. (1992). ..... 26

Figure 2.5: Modelled  $A = A(\psi_L)$ , normalized by well-watered assimilation rate, compared to measured data (symbols) for C<sub>3</sub> (left column) and C<sub>4</sub> species (right column) that cease assimilation around -2 MPa. Species-specific parameters are as in Table 2.2; all

the other parameters are listed in Table 2.1. Environmental conditions are chosen equal to the conditions in the corresponding experiments (see sources of data for details), hence two different environmental conditions are used in a). Data: a) filled boxes refer to SH cultivar, filled triangles to Sungro cultivar; open boxes and open triangles are relative to VPD=1 kPa and VPD=2.5 kPa respectively b) *Triticum aestivum*: Siddique et al. (2000); c) *Sorghum bicolor* L. cultivars: ContourAnsel et al. (1996); d) *Amarathus retroflexus* Ward et al. (1999). ..... 28

Figure 2.6: Modelled  $A = A(\psi_L)$ , normalized by well-watered assimilation rate, compared to measured data (symbols) for C<sub>3</sub> *Agropyron smithii* (a) and C<sub>4</sub> *Bouteloua gracilis* (b). Species-specific parameters are as in Table 2.2; all the other parameters are listed in Table 2.1. Environmental conditions are chosen equal to the conditions in the corresponding experiments (see sources of data for details)..... 29

Figure 2.7: Modelled relative assimilation rate as a function of soil moisture compared to data measured in C<sub>3</sub> and C<sub>4</sub> plants (panels a, b respectively). Environmental conditions are set in accordance to experimental conditions (see data sources for details); coherently, soil parameters refer to sandy loam for *Helianthus annuus* and *Bouteloua gracilis*, and to loam for *Panicum coloratum* (for values of soil parameters see, e.g., Rodriguez-Iturbe and Porporato 2004); all the other parameters are listed in Table 2.1 and table 2.2, with the exception of  $\alpha_m$  which was set equal to 4.15 for the simulations on left panel to defer the occurrence of numerical instabilities to lower soil moisture values; to cover the whole soil moisture range, deep infiltration and direct soil evaporation (Eq. (91)) were set to 0. Source of data: a) *Helianthus annuus*, Turner et al. ((1985); soil moisture is derived from the measured extractable soil water assuming zero extractable soil water at s=0.2 and 100% extractable soil water at soil saturation). b) *Panicum coloratum*, Seneweera et al. (2001); *Bouteloua gracilis*, Morgan et al. ((1998); averages across water and CO<sub>2</sub> treatments)..... 32

Figure 2.8: Soil moisture dynamics (black lines) and cumulative normalized assimilation (grey lines) during a 19 day dry-down in C<sub>3</sub> *Helianthus annuus* for two different soils: solid lines, loamy sand; dashed lines, loam (for values of soil parameters see, e.g., Rodriguez-Iturbe and Porporato 2004). All the parameters are as in Figure 2.7a, with the exception of non-zero deep infiltration..... 33

Figure 3.1: Example of soil moisture time series for rainfed agriculture (dotted line), micro-irrigation (solid line), and traditional irrigation (dashed line). Soil is sandy loam, with  $n = 0.43$ ,  $Z_r = 25$  cm (Rodriguez-Iturbe and Porporato 2004),  $s^* = 0.3$  and  $s_1 = 0.7$ . Average precipitation depth is  $\alpha = 15$  mm with interception parameters

$\Delta = 1 \text{ mm}$  and  $\kappa = 0.9$ , and rainfall frequency  $\lambda = 0.15 \text{ day}^{-1}$ . Evapotranspiration rate is  $E_{\max} = 0.45 \text{ cm day}^{-1}$ . ..... 43

Figure 3.2: Examples of steady state probability density functions of soil moisture under different rainfall amounts and patterns, relative to the two irrigation schemes (micro-irrigation, solid lines; traditional irrigation, dashed lines); the case of no irrigation is reported for reference (dotted lines). Left: constant mean event depth ( $\alpha = 15 \text{ mm}$ , with increasing  $\lambda$  and  $R_{tot}$  as indicated). Right: constant total growing season precipitation ( $R_{tot} = 400 \text{ mm}$ , with different combinations of  $\lambda$  and  $\alpha$ , as indicated). All the other parameters are as in Figure 3.1. .... 55

Figure 3.3: Average soil moisture (a, b) and long term soil water balance (c, d) under different rainfall amounts and timing, for (left) increasing total rainfall  $R_{tot}$  and fixed mean event depth ( $\alpha = 15 \text{ mm}$ ), and (right) fixed total growing season rainfall depth ( $R_{tot} = 400 \text{ mm}$ ) and variable  $\lambda$  and  $\alpha$ , for rainfed agriculture (dotted lines), micro-irrigation (solid lines) and traditional irrigation (dashed lines). In a) and b) dash-dotted lines represent  $s^*$ . In c) and d) irrigation volumes ( $V$ ) are compared to deep percolation and runoff losses ( $LQ$ );  $LQ$  for rainfed agriculture (dotted lines) is plotted for reference. All the components of the water balance are expressed as volumes per unit area, i.e. depths. All the other parameters are as in Figure 3.1. .... 57

Figure 3.4: Irrigation frequency requirements under different rainfall amounts and timing, for a) increasing total rainfall depth but fixed mean event depth ( $\alpha = 15 \text{ mm}$ ), and b) fixed total growing season rainfall depth ( $R_{tot} = 400 \text{ mm}$ ) for micro-irrigation (solid lines) and traditional irrigation (dashed lines). All the other parameters are as in Figure 3.1. .... 60

Figure 3.5: Difference in required irrigation volumes between traditional and micro-irrigation,  $V_t - V_m$  (units are meters of applied water per growing season), as a function of a) rainfall amount and pattern (here represented by mean event depth,  $\alpha$ , and frequency of events,  $\lambda$ ), and b) crop water requirements (here represented by maximum transpiration rate,  $E_{\max}$ , and point of incipient stomatal closure,  $s^*$ ). Dashed lines in a) represent combinations of  $\alpha$  and  $\lambda$  leading to the same total precipitation over the growing season,  $R_{tot}$ , as indicated. All the other parameters are as in Figure 3.1. .... 64

Figure 4.1: Example of soil moisture time series for two choices of the parameters  $\tilde{s}$  and  $\hat{s}$ ; soil moisture temporal evolution for rainfed agriculture is reported for reference

(dotted line), as well as  $s^* = 0.3$  (thin horizontal lines). Soil is sandy loam with  $n=0.43$ ,  $Z_r = 25$  cm (Rodriguez-Iturbe and Porporato 2004);  $s_1 = 0.7$ . Average precipitation depth is  $\alpha = 15$  mm and rainfall frequency  $\lambda = 0.15$  day<sup>-1</sup>. Evapotranspiration rate is  $E_{\max} = 0.45$  cm day<sup>-1</sup>..... 75

Figure 4.2: Example of steady state probability density functions of soil moisture relative to different choices of the parameters  $\tilde{s}$  and  $\hat{s}$ , as indicated. As a term of comparison, the soil moisture pdf for rainfed agriculture is represented (dotted lines), as well as the case of micro-irrigation (solid line in b)). Note that the vertical axes scale differ in a) and b); also, in b) the atom of probability in  $\hat{s}=0.25$  (thick vertical line) is not to scale. All the other parameters are as in Figure 4.1. .... 79

Figure 4.3: Irrigation volumes as a function of intervention point  $\tilde{s}$ , for different choices of irrigation parameter  $\hat{s}$  (from top to bottom,  $\hat{s}$  increases from 0.2 to 0.7). As reference the case of micro-irrigation is plotted as well (dotted line). The thin vertical line discriminate deficit irrigation (on the left) and over-irrigation (on the right). All the other parameters are as in Figure 4.1. .... 81

Figure 4.4: Observed crop yields as a function of total seasonal transpiration and fitted model for a) *Triticum aestivum* (open symbols and dotted line: Karam et al. (2009),  $r^2=0.70$ ; other symbols and solid line: Kang et al. (2002),  $r^2=0.66$ ) and b) *Zea mays* (dark symbols and line: Payero et al. (2006),  $r^2=0.91$ ; gray symbols and dotted line: Igbadun et al. (2007),  $r^2=0.72$ ). Different symbols refer to different irrigation treatments, consisting in a) maintenance of lower, intermediate or high soil water content, and b) irrigation withdrawal over different growth period (see sources of data for more details on irrigation treatments)..... 85

Figure 4.5: Net income as a function ‘intervention’ soil moisture  $\tilde{s}$  for a) different irrigation schemes (micro-irrigation: solid lines; traditional irrigation with  $\hat{s}=0.4$  and  $\hat{s}=0.6$ : dashed and dotted lines respectively) and water costs (gray lines refer to income for higher water costs), and b) different rainfall amounts ( $R_{tot} = 337$  mm and 168 mm for black and gray lines respectively) and timing ( $\lambda = 0.3$  and  $0.1$  day<sup>-1</sup> for dashed and dotted lines respectively).  $c_c = 0.05$  arbitrary units kg<sup>-1</sup>, while  $c_w = 35$  arbitrary units m<sup>-1</sup> ha<sup>-1</sup> (except for gray lines in a) where  $c_w = 53$  arbitrary units m<sup>-1</sup> ha<sup>-1</sup>). In a) total rainfall parameters are  $\alpha = 15$  mm and  $\lambda = 0.15$  day<sup>-1</sup>; in b) only the case of traditional irrigation with  $\hat{s} = 0.4$  is depicted. The growing season is supposed to last 150 days. All the other parameters are as in Figure 4.1. .... 88

Figure 4.6: Probability density functions of a) average crop yield and b) irrigation volume for different values of  $\tilde{s}$ , once rainfall interannual variability is included. Rainfall parameters are those of Mahanattan, eastern Kansas ( $a_\alpha = 21.8$ ,  $b_\alpha = 1.90$  mm<sup>-1</sup>,  $a_\lambda = 27.4$ ,  $b_\lambda = 91.9$  day; black lines) and SGS LTER, northern Colorado ( $a_\alpha = 15.3$ ,  $b_\alpha = 2.56$  mm<sup>-1</sup>,  $a_\lambda = 6.35$ ,  $b_\lambda = 20.3$  day; gray lines) (Appendix C). All the other parameters are as in Figure 4.1. In a) the average crop yield pdfs for rainfed agriculture are plotted for reference (dotted lines)..... 93

Figure 5.1: Case studies: i) south-western Colorado Rocky Mountains, ii) Smoky Mountains at the North Carolina-Tennessee border, iii) Flint Hills in north-eastern Kansas, and iv) Ozark Mountains in north-western Arkansas. Covered areas range from 1500 to 3100 km<sup>2</sup>, with boundaries independent of river network structure, and elevation differences between 564 to 2250 m. DEM data source is the USGS National Elevation Dataset (NED), with nominal horizontal resolution of 1 arc-second (approximately 30 meters along the Equator); elevations are resolved to the meter..... 102

Figure 5.2: Impact of trends and degrees of anisotropy on slope and aspect distribution in the simple case of uniformly-distributed partial derivatives on an elliptical domain. From left to right columns contain the contour plots of the joint pdf  $p(\partial_x h, \partial_y h)$ , and the corresponding  $p_S(S)$  and  $p_\alpha(\alpha)$ . Rows from top to bottom explore the effects of anisotropy only (a), trend only (b), and their combination (c). In panel (a)  $a$  and  $b$  are the major and minor semi-axes of the elliptic domain of the partial derivative distributions, while  $c$  represents the radius of the domain in the isotropic case. In panel (b),  $\mu_{\partial_x h}$  and  $\mu_{\partial_y h}$  represents the means of  $\partial_x h$  and  $\partial_y h$  respectively, which correspond to the trend. .... 109

Figure 5.3: Comparison between observed derivatives in orthogonal directions and assumed marginal distributions for the four case studies (Figure 5.1) both in linear scale (main plots) and semi-logarithmic scales (insets, to enhance tail behavior). The different lines represent the theoretical pdf's under different assumptions on the distribution of the first partial derivatives: Gaussian joint pdf (solid lines), Laplace joint pdf (dashed) and Pearson type VII joint pdf (dotted). Pdf parameters have been estimated directly from the fields of partial derivatives and are listed in Table 5.1; given the nature of the observed partial derivatives in the Smoky Mountain area, no attempt has been made to fit the Pearson type VII marginal distributions in this case. Derivative values are obtained assuming a nominal resolution of 30 m, despite the differences in site latitudes. .... 113

Figure 5.4: Comparison with data of derived slope pdf's including trend and correlation between first derivatives. Lines and plots are as in Figure 5.3..... 122

Figure 5.5: Comparison with data of derived aspect pdf's including trend and correlation between first derivatives. Lines as in Figure 5.4..... 125

Figure 5.6: Mean (left column) and standard deviation (right column) of instantaneous direct solar radiation as a function of the partial-derivative standard deviation,  $\sigma_{\partial_x, \partial_y, h}$  for three days. Modeled quantities (lines) refer to an isotropic landscape with no trend and Gaussian-distributed partial derivatives. Symbols represent direct solar radiation mean and standard deviation, estimated by applying Eq. (76) to each pixel for the four case studies. All lines refer to 38° of latitude N, while the latitude of case studies varies from 35.3 to 39.1° (Figure 5.1). In each plot lines from dark grey to light grey refer to 6 am, 8 am, 10 am, 12 noon local apparent time..... 129

Figure 5.7: Daily evolution of solar-irradiance standard deviation: lines (every 20 days) correspond to different days, from the winter solstice (dashed light grey line) through the spring equinox (dashed dark grey line) to the summer solstice (dashed black line). In the inset, maximum daily irradiance standard deviation (dashed line) and time at which such maximum is reached (solid line) as a function of DOY. As in Figure 5.6, the landscape, located at 38°N, is assumed to be isotropic with no trend and Gaussian distributed partial derivatives. The partial derivative standard deviation is set to 0.35 m m<sup>-1</sup>..... 131

Figure C.1: Growing season (April to September) rainfall regime at Manhattan, KS (39°12' N, 96°35' W; coop. id. 144972; data available online at [www.ncdc.noaa.gov](http://www.ncdc.noaa.gov)). Daily precipitation during a very dry (a) and a very wet (b) growing season. (c) Time series of mean depth of rainfall events,  $\alpha$  (mean 11.4 mm, standard deviation, s.d., 2.4 mm); (e) mean rate of storm arrival,  $\lambda$  (mean 0.30 1/d, s.d. 0.06 1/d); (g) total rainfall during the growing season,  $P$  (mean 612.4 mm, s.d. 180.3 mm). Frequency distribution and fitted two-parameter gamma distributions of  $\alpha$  (d) and  $\lambda$  (f) (parameters:  $a_{\alpha}=21.8$ ,  $b_{\alpha}=1.90$  1/mm;  $a_{\lambda}=27.4$ ,  $b_{\lambda}=91.9$  d). (h) Frequency distribution of total precipitation,  $P$ , and corresponding theoretical model (solid line); the pdf obtained assuming no interannual variability is also plotted for comparison (dashed line)..... 164

Figure C.2: Pdf of rainfall depths (a), and interarrival times (b), obtained as superstatistics of daily and interannual variability (continuous lines); comparison with the exponential pdf corresponding to no interannual variability (dotted lines), and observed frequency distributions at Manhattan, KS (closed symbols). (c) Pdf of the

duration of periods of plant water stress at Manhattan, KS: Monte Carlo simulation (closed symbols); fitted Pareto distribution (continuous line); pdf obtained with no interannual variability (open symbols). The parameters of the stochastic soil moisture model (Laio et al. 2001) are: soil type is silty loam ( $n=0.47$ ,  $s_H=0.14$ ,  $s_w=0.16$ ,  $s^*=0.35$ ,  $s_{fc}=0.59$ ,  $K_s=33$  cm/d,  $b=5$ ,  $E_w=0.01$  cm/d) and maximum vegetation transpiration is  $E_{max}=0.45$  cm/d. .... 167

Figure C.3: Time series of ANPP (stars) and estimated ANPP at KNZ LTER site, KS (a), and SGS LTER site, CO (b). Estimated ANPP is obtained with a multiple regression model using only the total rainfall over the growing season,  $P$  (open symbols), and including also the mean event depth,  $\alpha$ , and the mean interval between rainfall events,  $1/\lambda$  (close symbols). At KNZ the linear regression using the total precipitation resulted in  $r^2=0.40$  ( $237+0.30P+\xi$ ;  $\sigma_\xi=85$  g/m<sup>2</sup>), while the multiple linear regression improved  $r^2$  up to 0.47 ( $437-6.2\alpha-41\lambda^{-1}+0.32P+\xi$ ;  $\sigma_\xi=84$  g/m<sup>2</sup>). At SGS the linear regression with  $P$  yielded  $r^2=0.27$  ( $40+0.27P+\xi$ ;  $\sigma_\xi=35$  g/m<sup>2</sup>), while the multiple linear regression gave  $r^2=0.53$  ( $173+28\alpha-40\lambda^{-1}-0.29P+\xi$ ;  $\sigma_\xi=31$  g/m<sup>2</sup>). The random deviation from the linear regression,  $\xi$ , is practically Gaussian distributed, with zero mean and standard deviation  $\sigma_\xi$ . At both sites, the growing season is assumed to last from the beginning of April to the end of September. Annual ANPP data collected at KNZ and SGS LTER sites are available online at <http://intranet.lternet.edu/cgi-bin/anpp.pl> (PI: A.K. Knapp and M.D. Smith) (Knapp and Smith 2001). Note that in order to obtain meaningful statistics for KNZ we used rainfall records from Manhattan, KS, located approximately 12 km north of the LTER site. Daily rainfall records for SGS LTER site are available on line at <http://sgs.cnr.colostate.edu>. .... 170

Figure C.4: Normalized mean ANPP under different rainfall scenarios corresponding to changes in interannual variability for constant mean rainfall totals, at KNZ (continuous line) and at SGS (dashed line). The hypothetical rainfall scenarios are generated such that the means of  $\alpha$  and  $\lambda$ ,  $\bar{\alpha}$  and  $\bar{\lambda}$ , are modified in opposite ways in order to keep the mean total precipitation constant,  $\bar{P} = \bar{\alpha} \bar{\lambda}$ . Thus values of the parameter  $k = \bar{\alpha}_{projected} / \bar{\alpha}_{current}$  higher than one correspond to increased mean intensity and reduced mean frequency of rainfall events, and vice versa for  $k < 1$ . The ANPP is obtained by means of the multiple regression models of Figure C.3 that employ the annual mean depth of rainfall events  $\alpha$ , the annual mean rainfall frequency  $\lambda$ , and the cumulative precipitation during the growing season  $P$ . .... 171

## **Acknowledgments**

This research was supported by the Office of Science, Biological and Environmental Research Program (BER), U.S. Department of Energy, through the Great Plains Regional Center of the National Institute for Global Environmental Change (NIGEC) under grant DE-FG02-95ER62083; the U.S. National Science Foundation under grants EAR-0628432 and EAR-0635787; the U.S. Department of Agriculture, through the Agricultural Research Service of Temple, TX, under grant USDA-58-6206-7-029.

# 1 Introduction

The 2009 Global Climate Change Impacts report recommends, as part of its concluding agenda, to both “expand our understanding of climate change impacts” and “extend understanding on how society can adapt to climate change” (Karl et al. 2009, p. 153). Both are daunting tasks, because of the number of feedbacks among climate, vegetation and anthropogenic activities, and the variety of temporal and spatial scales involved. The main focus of this dissertation is the impact of hydroclimatic variability on vegetation dynamics at multiple temporal and spatial scales.

At a given point in space, the fundamental variables driving vegetation dynamics are solar radiation, soil moisture and nutrient supply (e.g., Lambers et al. 1998). In turn, at the sub-daily time scale, vegetation controls soil moisture depletion through transpiration (Hsiao 1973, Leuning 1995, Nilsen and Orcutt 1998, Daly et al. 2004a). The cumulative effects of vegetation dynamics are apparent at longer time scales, ranging from differences in soil moisture evolution during a single dry-down (Morison and Gifford 1984, Kalapos et al. 1996, Morgan et al. 1998, Seneweera et al. 2001, Grassi and Magnani 2005) to differences in plant productivity between subsequent growing seasons (Robertson 1974, Lauenroth and Sala 1992, McCaig 1997, Knapp and Smith 2001, Porporato et al. 2006). An understanding of vegetation response to water availability and its daily to interannual variability is also crucial for managing water resources for agricultural productivity, profitability and sustainability. With the increase in

population, and hence food and fiber demand, along with biofuels, the necessity of a careful and optimal water resource allocation may become even more pressing, especially when the predicted climate change is factored in (Gleick 2003, Jury and Vaux 2007). In fact, climate change, with its compound effects of altered rainfall regime (e.g., Easterling et al. 2000), and elevated atmospheric CO<sub>2</sub> and temperature, is expected to impact the productivity, composition, and distribution of terrestrial ecosystems.

While a wealth of experimental results are available in the literature, a modeling framework bridging across the relevant scales is not fully developed yet. With the aim of improving currently available models, the first part of this dissertation describes vegetation responses to soil moisture dynamics from hourly to interannual time scales.

Despite the observed impact of water stress on photosynthesis, the most used models of CO<sub>2</sub> assimilation do not directly account for it (Farquhar et al. 1980, Collatz et al. 1991, Collatz et al. 1992, Chen et al. 1994, von Caemmerer 2000). This is a significant limitation to model prognostic capabilities in particular when the predicted increase in drought occurrence is considered. In Chapter 2 (based on Vico and Porporato 2008), an extension of existing models of CO<sub>2</sub> assimilation is presented, to explicitly include the various metabolic and diffusive limitations to photosynthesis ascribed to water stress. Extensive comparison with data shows that the model is suitable to describe the reduction in CO<sub>2</sub> assimilation rate with decreasing leaf water potentials in various species. A simultaneous analysis of photosynthesis, transpiration and soil moisture

dynamics provides a more physiological basis to the often-used upscaled (e.g., daily) semi-empirical relationships between soil moisture and plant assimilation and transpiration rate (Dingman 1994, Rodriguez-Iturbe and Porporato 2004). Such relationships are crucial for many ecohydrological applications, among which the exploration of the impact of rainfall patterns and irrigation practices on agricultural productivity, which are discussed Chapters 3 and 4. This application bridges the gap between theoretical and applied research, by including the water management aspect into the picture.

In Chapters 3 and 4, the focus is on water allocation for agricultural purposes, a highly non-trivial task given the unpredictability of rainfall and the numerous soil-plant atmosphere interactions. In Chapter 3 (based on Vico and Porporato 2009a), two idealized irrigation schemes are analyzed: a traditional scheme consisting in the application of fixed water volumes that bring soil moisture to field capacity, and a micro-irrigation scheme continuously supplying water to avoid plant water stress. This analysis is carried on by means of a simplified soil water balance (Rodriguez-Iturbe et al. 1999), including rainfall occurrence as a stochastic process and irrigation as a state dependent event. The analytically obtained steady-state soil moisture probability density function allows determining required irrigation frequency and volumes along with water lost in runoff and deep infiltration for the two irrigation schemes, as a function of climate, soil and vegetation parameters. In Chapter 4 the same theoretical

framework is expanded by considering a more general irrigation scheme and including the often observed rainfall interannual variability (Appendix C, based on Porporato et al. 2006). The model is then employed to determine the optimal irrigation practices regarding water use and crop yield, as well as net income. While stress-avoidance micro-irrigation in theory represents the optimal irrigation practice for profitability and water loss minimization, such a fine-tuned irrigation may be difficult to apply in practice (English et al. 2002, Jones 2004). The inclusion of rainfall interannual variability makes the proposed model a useful tool for long-term water management and strategic irrigation choices, as it provides the probability distributions of crop yield, net income and required irrigation volumes. As such, it allows determining the degree of risk stemming from rainfall interannual variability, in terms of probability of obtaining a certain minimum net income.

Interactions among climate, soil moisture and vegetation are further complicated when landscape heterogeneities are taken into account, as topographic position strongly influences the amount of solar radiation reaching canopy and soil (e.g., Dubayah et al. 1990, Oliphant et al. 2003). In Chapter 5 (based on Vico and Porporato 2009b), the effects of topographic features on direct solar radiation input are explored in a stochastic framework. A simple yet realistic probabilistic description of local slope and aspect as a function of properties of the field of elevation changes is proposed and tested against observed slope and aspect histograms for four different landscapes across the

continental USA. Different classes of models of elevation changes are considered, for which the theoretical distributions of slope and aspect are obtained. The features of the obtained distributions are related to large-scale landscape structures, such as regional trends and anisotropy, and their influence on mean and variance of solar radiation is explored for different times of the day and days of the year.

In addition to the effect of slope and aspect on the energy balance, topography also influences water and nutrient availability, and hence ecosystem dynamics (e.g., Mahler et al. 1979, Moore et al. 1993, Florinsky and Kuryakova 1996, Florinsky et al. 2004). To study these compound effects a minimalistic ecosystem model is outlined in Chapter 6. The goal is to develop a parsimonious model, including the most relevant interactions among soil moisture, vegetation and nutrient dynamics, and accounting for topographic effect through a spatially implicit, probabilistic approach.

## **2 Modelling C<sub>3</sub> and C<sub>4</sub> photosynthesis under water-stressed conditions**

This chapter is based on the article Vico G. and A. Porporato (2008), Modelling C<sub>3</sub> and C<sub>4</sub> photosynthesis under water-stressed conditions, *Plant and Soil*, 313, 187-203.

### **2.1 Introduction**

Modelling plant response to droughts is essential to predict ecosystem productivity in face of increased growing season droughts and more intense convective rainfall events predicted by climate-change scenarios (Groisman et al. 1999, Easterling et al. 2000). Despite the wealth of experimental studies showing both diffusive limitations (i.e., reduction of stomatal and mesophyll conductances) and metabolic limitations, the main physiological processes responsible for photosynthetic impairment are still a matter of controversy (Griffiths and Parry 2002). An improved understanding of the physiological bases of photosynthesis down-regulation, especially in relation to water deficit is highly desirable.

A number of models of photosynthesis account for the impact of plant water stress on stomatal conductance (e.g., Jarvis 1976, Tardieu and Davies 1993, Dewar 2002, Gao et al. 2002, Diaz-Espejo et al. 2006). In contrast, reduction of the mesophyll conductance and metabolic limitations due to water stress are seldom considered in detail. Some models have used empirical soil-moisture or leaf-water-potential functions to

correct the obtained CO<sub>2</sub> assimilation rate but have not discussed the complex physiology of plant photosynthesis at low water availability (e.g., Foley et al. 1996, Daly et al. 2004a). In other models (Amthor 1994, e.g., Sellers et al. 1996), the maximum carboxylation rate is reduced under water stress conditions, while the other processes involved in photosynthesis are supposed not to be affected. Here we review experimental results available in the literature relative to several processes involved in plant photosynthesis and use them to formulate a model describing the impact of water availability on photosynthesis at the sub-daily (e.g., hourly) time scale. We aim at a more physiological justification of the empirical functions linking assimilation and transpiration rates to soil moisture dynamics, frequently used in ecohydrology and micrometeorology. Despite its numerous parameters, the resulting model allows us to analyze and compare the effect of water stress on different components of the plant activity and plant physiology. We hope that this in turn will be useful to formulate hypotheses for detailed experiments as well as to simulate transpiration and photosynthesis under water stress for those species for which data are available.

To proceed quantitatively, we include the metabolic limitations in well-known models of photosynthesis in C<sub>3</sub> and C<sub>4</sub> species (originally proposed by Farquhar et al. (1980), and Berry and Farquhar (1978)), through a set of empirical functions of leaf water status calibrated on available data. The C<sub>3</sub> and C<sub>4</sub> photosynthesis models are then coupled to stomatal and mesophyll conductance models accounting for diffusive

limitations to photosynthesis. The photosynthesis and conductance models are finally embedded into a model of the soil-plant-atmosphere continuum (SPAC) to compute photosynthesis and transpiration rates during dry-down conditions.

## **2.2 Model formulation**

A simple yet realistic way to describe photosynthesis is based on recognizing the presence of different limiting factors, which impact the activities of the plant at the photosynthesis level. After the seminal work of Farquhar et al. (1980), CO<sub>2</sub> assimilation in C<sub>3</sub> species has been extensively modelled as the minimum of two potential capacities, respectively driven by available CO<sub>2</sub> ( $A_C$ ) and solar radiation ( $A_J$ ),

$$A_{net} = \min(A_C, A_J) - R_d, \quad (1)$$

where  $R_d$  is the total mitochondrial respiration. The same model structure has also been used for C<sub>4</sub> plants (Collatz et al. 1992, Chen et al. 1994, von Caemmerer and Furbank 1999). The details are summarized in Appendix A.

The CO<sub>2</sub> assimilation model of Eq. (1) is based on the assumption of well-watered conditions. The impact of extended dry periods on CO<sub>2</sub> assimilation is typically only included as reductions in soil-root-plant and stomatal conductances. However, experimental observations show that, besides stomatal limitations (e.g., Chaves 1991, Cornic 2000, Flexas et al. 2004a, Buckley 2005), also ‘non-stomatal’ effects play an important role in limiting plant carbon assimilation under water stress (e.g., Polley et al. 1992, Lawlor 1995, Tezara et al. 1999, Lawlor 2002, Lawlor and Cornic 2002, Ghannoum

et al. 2003). The 'non-stomatal' effects include both a possible limiting mesophyll conductance (e.g., Grassi and Magnani 2005), and a truly metabolic component, involving decreased availability and/or activity of enzymes at low levels of water potentials (e.g., Gimenez et al. 1992, Tezara et al. 1999, Parry et al. 2002). In the case of C<sub>4</sub> plants, limitations at the biochemical level may also involve effects on the CO<sub>2</sub> concentrating mechanism (Du et al. 1996). Several authors show that under mild stress CO<sub>2</sub> assimilation rate is mainly impaired by diffusive limitations, which reduce CO<sub>2</sub> availability to photosynthesis (Flexas et al. 2004b, Grassi and Magnani 2005). However, as leaf water potential is further depleted, metabolic limitations to CO<sub>2</sub> assimilation also become important (e.g., Kaiser 1987, Lawlor 2002), and should be considered. It should be noted that the extent of metabolic *vs.* stomatal and mesophyll conductance limitations to photosynthesis under water stress is still a matter of debate (e.g., Griffiths and Parry 2002 and references therein), which has been fuelled in part by the discrepancies among different studies (as shown by Flexas and Medrano (2002)) and the difficulties in comparing experimental results for different species, plant conditions before water stress, methods of stress imposition, and presence of simultaneous stress factors (e.g., Kaiser 1987, Chaves 1991).

### **2.2.1 Metabolic limitations to photosynthesis under drought**

To account for the metabolic limitations, we modified the CO<sub>2</sub> assimilation model detailed in Appendix A, by including empirical corrections describing the ‘vulnerability’ to water stress of the processes involved in photosynthesis. Although relative water content, cell volume or stomatal opening might be more appropriate indicators of plant water status (Chaves 1991, Lawlor 2002, Ghannoum et al. 2003), here we use leaf water potential,  $\psi_L$  (as in Tezara et al. (1999)), for it allows us to represent both plant and soil water status on a common physical basis and clearly define water fluxes within the SPAC. Such a choice makes our model best suited to describe species with anisohydric behaviour (Tardieu and Simonneau 1998).

As detailed below, experimental data show that, among the processes involved in photosynthesis, maximum rate of carboxylation, electron transport rate and relative reduction in the activity of CO<sub>2</sub> concentrating mechanism (in C<sub>4</sub> species) are the ones most affected by plant water status (Du et al. 1996, Lu and Zhang 1998, 1999, Tezara et al. 1999, Tezara et al. 2002, Ghannoum et al. 2003). Under mild stress these processes appear to be almost insensitive to changes in leaf water status, while a further decrease in leaf water potential results in significant changes down to a point where the activity is practically ceased. To describe this behaviour, we chose the following three-parameter, Weibull-type vulnerability curve

$$f_i(\psi_L) = a_i \exp\left[-\left(\frac{-\psi_L}{d_i}\right)^{b_i}\right]. \quad (2)$$

This functional form is used to represent the impact of  $\psi_L$  on maximum carboxylation rate (i.e.,  $f_i(\psi_L) = V_{c,\max}(\psi_L)$ ; Eq. (83)), quantum yield of electron flow (i.e.,  $f_i(\psi_L) = \phi_{PSII}(\psi_L)$ ; Eq. (87)), and C<sub>4</sub>-cycle activity (i.e.,  $f_i(\psi_L) = \eta_P(\psi_L)$ ; Eq. (84)). Simpler functions, such as linear or exponential forms, would not account for the observed relative unresponsiveness under mild stresses, and would possibly lead to unrealistic values of plant activity under extreme water stress. Furthermore, Eq. (2) has been previously used to describe the impact of cavitation on xylem conductance (Sperry et al. 2002) (Eq. (90)).

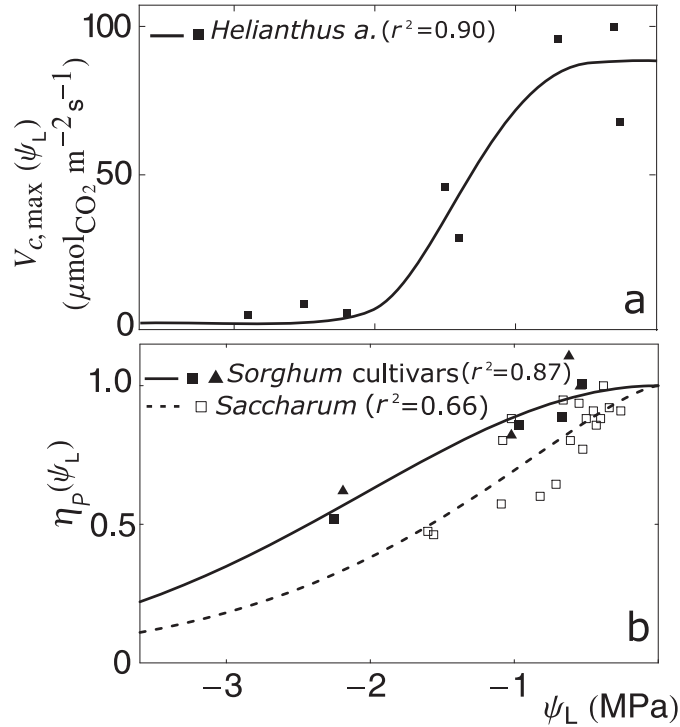


**Figure 2.1:** Impact of leaf water potential,  $\psi_L$ , on two key metabolic processes for  $C_3$  and  $C_4$  species: a) maximum carboxylation rate,  $V_{c,max}$ ; b) relative activity of PEP carboxylase,  $\eta_P(\psi_L)$ . Experimental data (symbols) are fitted to the respective vulnerability curves (Eq. (2); Table 2.1 and Table 2.2). Source of data: *Helianthus annuus* L.: Tezara et al. (1999, 2002; see text for details); *Saccharum* sp.: Du et al. (1996); *Sorghum bicolor* L. cultivars (filled box: 1063 ICSV; filled triangles, MIGSOR): ContourAnsel et al. (1996).

**Table 2.1:** Parameter values common to C<sub>3</sub> and C<sub>4</sub> functional types.

Parameter	Value	Description
$R_{AI}$ (m <sup>2</sup> m <sup>-2</sup> )	5.6	Root Area Index (Eq. (89))
$L_{AI}$ (m <sup>2</sup> m <sup>-2</sup> )	2	Leaf Area Index
$\omega$ (-)	4	Parameter driving root response to soil moisture
$g_{p,max}$ (m s <sup>-1</sup> MPa <sup>-1</sup> )	1.3·10 <sup>-7</sup> [1]	Xylem conductance when no cavitation occurs (Eq. (90))
$b_c$ (-)	1.1	Parameter in Eq. (90)
$d_c$ (MPa)	1.1	Parameter in Eq. (90)
$g_{bs}$ (mmol m <sup>-2</sup> s)	13	Conductance between bundle sheath and mesophyll
$\kappa_A$ (-)	0.95	Curvature factor (Eq. (82))
$\kappa_\phi$ (-)	0.95 [2]	Curvature factor (Eq. (86))
$K_C$ (μmol mol <sup>-1</sup> )	302 [2]	Michelis-Menten coefficient for CO <sub>2</sub> (Eq. (83))
$K_O$ (μmol mol <sup>-1</sup> )	256 [2]	Michelis-Menten coefficient for O <sub>2</sub> (Eq. (83))
$o$ (mol mol <sup>-1</sup> )	0.210	Intercellular O <sub>2</sub> concentration (Eq. (83))
$P_a$ (Pa)	1.013·10 <sup>5</sup>	Atmospheric air pressure
$\rho_a$ (kg m <sup>-3</sup> )	1.2	Air density
$g_b$ (m s <sup>-1</sup> )	0.2 [3]	Leaf boundary layer conductance (per ground area)
$g_a$ (m s <sup>-1</sup> )	0.1 [3]	Atmospheric conductance (per ground area)
$g_s$	1.6 g <sub>s,CO2</sub> [3]	Stomatal conductance (per leaf area)
$g_{b,CO2}$	$g_b/1.46$ [3]	Leaf boundary layer conductance to CO <sub>2</sub>
$g_{a,CO2}$	$g_a$ [3]	Atmospheric conductance to CO <sub>2</sub>
$\alpha_m$ (-)	1.65 [4]	Leaf internal CO <sub>2</sub> conductance dependence on g <sub>s,CO2</sub> in C <sub>3</sub> (C <sub>4</sub> ) species
$V_{P,max,ww}$ (μmol m <sup>-2</sup> s <sup>-1</sup> )	120 [5]	Maximum PEP carboxylase under well-watered conditions
$b_P$ (-)	1.98 [6]	Parameter of the PEP relative activity function $\eta_P(\psi_L)$
$d_P$ (MPa)	2.92 [6]	Parameter of the PEP relative activity function $\eta_P(\psi_L)$
$V_{Pr}$ (μmol m <sup>-2</sup> s <sup>-1</sup> )	80 [5]	PEP regeneration rate (Eq. (84))
$K_P$ (μmol mol <sup>-1</sup> )	80 [5]	Michelis-Menten coefficient for C <sub>4</sub> species (Eq. (84))

[1] Kocacinar and Sage (2003); [2] Leuning (1995); [3] Jones (1992); [4] value obtained from fitting of the data measured in *Nicotiana tabacum* (Galmes et al. 2006); [5] von Caemmerer (2000); [6] value obtained from fitting of data measured in *Sorghum bicolor* (Figure 2.1b)

### Maximum carboxylation rate

The mechanism and extent of the impact of water stress on maximum carboxylation rate,  $V_{c,max}$ , is still controversial. On the one hand, a reduction in Rubisco capacity to fix CO<sub>2</sub> in water-stressed conditions has been observed in both C<sub>3</sub> and C<sub>4</sub> species (Du et al. 1996, Massacci et al. 1996, Tezara et al. 1999), thus suggesting a depletion of  $V_{c,max}$  under water stress. On the other hand, recent interpretations (Flexas et al. 2006a, Galmes et al. 2006) of the dependence of net assimilation,  $A_{net}$ , upon intercellular air CO<sub>2</sub> partial pressure,  $c_i$ , (i.e.,  $A_{net}$  vs.  $c_i$  curve) showed a substantial independence of maximum carboxylation rate from water stress when a finite mesophyll conductance,  $g_m$ , is considered (as suggested by Ethier and Livingston 2004).

In our model we consider the decreases of both  $V_{c,max}$  and mesophyll conductance under water stress, as discussed here and below. To avoid any uncertainty related to *in vitro* measurements of Rubisco activity (Rogers et al. 2001), we fitted Eq. (1) to  $A_{net}$  vs.  $c_i$  curves observed under different  $\psi_L$ . However, the simultaneous estimate of  $V_{c,max}$  and  $g_m$ , which is required when including the latter, often leads to implausible results or even fails, due to the presence of several local minima and flat regions in the function to be minimized (Dubois et al. 2007). To circumvent this problem, we performed several conditional least square fittings of  $A_{net}$  vs.  $c_i$  data, by assuming each time a different value for  $g_m$  in the range of those observed experimentally (e.g., Warren and Adams (2006),

Table 2.1). When plotted against the assumed values of  $g_m$ , the fitted values of  $V_{c,max}$  exhibit a plateau, thus allowing us to estimate the value of  $V_{c,max}$  within a 10% range. We applied this procedure to data measured in C<sub>3</sub> *Helianthus annuus*, repeating it for the different available  $\psi_L$  (Gimenez et al. 1992, Tezara et al. 1999, Tezara et al. 2002). The obtained values for  $V_{c,max}$  are plotted against  $\psi_L$  in Figure 2.1a, and are used to determine the parameters  $a_V=V_{c,max,ww}$  (representing the value of  $V_{c,max}$  under well-watered conditions),  $b_V$  and  $d_V$  of the vulnerability curve (Eq. (2)) by least square fitting (Table 2.2). *Helianthus annuus* data are adequately described by the chosen vulnerability curve (Figure 2.1a). Moreover, the general shape is in agreement with the corrections used by other authors (e.g., Amthor 1994, Sellers et al. 1996), and the obtained value for  $V_{c,max,ww}$  is in the range of values reported by e.g. Wullschleger (1993) for this species. In absence of other species-specific data, the obtained decrease in  $V_{c,max}$  was extended to other C<sub>3</sub> species, once  $V_{c,max,ww}$  was substituted by species-specific values (e.g., Wullschleger 1993).

In the case of C<sub>4</sub> species, the impact of the CO<sub>2</sub> concentration mechanism further complicates the expression to be fitted, thus making the  $A_{net}$  vs.  $C_i$  curve fitting even more problematic. As a first approximation, we used the same vulnerability curve of *Helianthus annuus* after  $V_{c,max,ww}$  was substituted by values observed in C<sub>4</sub> species (as summarized in Table 2.2).

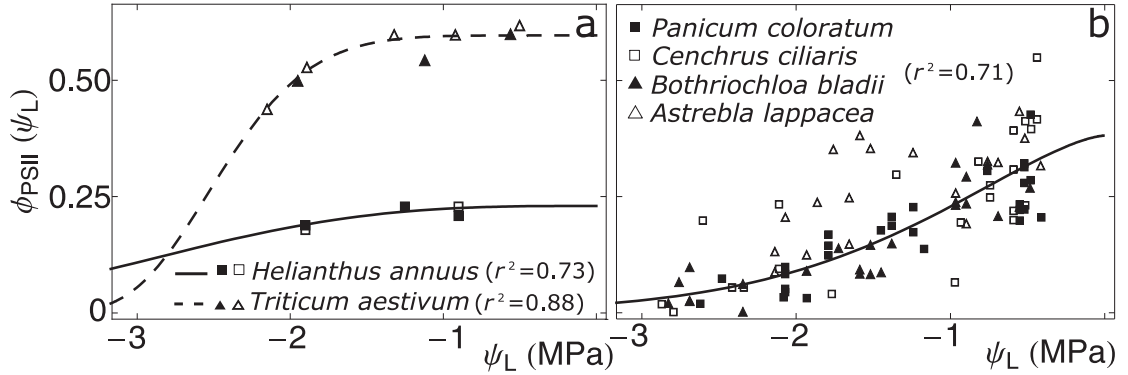


**Figure 2.2:** Impact of leaf water potential,  $\psi_L$ , on photochemical quantum yield of PSII,  $\phi_{PSII}(\psi_L)$  (Eq. (2)): experimental data (symbols) and fitted vulnerability curves (Table 2.2) for a) two C<sub>3</sub> species, and b) four C<sub>4</sub> species (in this case, the line represents the result of fitting all the point together). Source of data: a) Lu and Zhang (1998; filled triangles), Lu and Zhang (1999; open triangles), Pankovic et al. (1999; boxes); b) Ghannoum et al. (2003).

### Electron transport rate

Experimental results show that a decrease in  $\psi_L$  is paralleled by a decrease in electron transport rate,  $J$ , caused by a decrease in photochemical quantum yield,  $\phi_{PSII}$  (Lu and Zhang 1998, 1999, Tezara et al. 2002, Ghannoum et al. 2003). The vulnerability curve in Eq. (2) is again flexible enough to describe the observed responses of  $\phi_{PSII}$  to  $\psi_L$  (Figure 2.2). Parameters  $a_\phi = \phi_{PSII,ww}$  (i.e., photochemical quantum yield under well-watered conditions),  $b_\phi$  and  $d_\phi$  estimated by least square fitting of Eq. (2) to observed values (Lu and Zhang 1998, 1999, Pankovic et al. 1999, Ghannoum et al. 2003) are summarized in Table 2.2. For the sake of simplicity, we used a single vulnerability curve for C<sub>4</sub> species, obtained by fitting the data of the four species, despite the apparent

species-specificity of such response (possibly due to different energy requirements of C<sub>4</sub> sub-pathways; (Ehleringer and Pearcy 1983)).

**Table 2.2:** Species-specific parameters. Simulations relative to *Amarathus retroflexus* and *Panicum coloratum* are performed with the same parameters as *Sorghum bicolor*.

Parameter	C <sub>3</sub> species			C <sub>4</sub> species	
	<i>Helianthus</i>	<i>Triticum</i>	<i>Agropyron</i>	<i>Sorghum</i>	<i>Bouteloua</i>
$a_V = V_{c,max,ww}$ ( $\mu\text{mol m}^{-2} \text{s}^{-1}$ )	88 <sup>[1]</sup>	83 <sup>[2]</sup>	88 <sup>[1]</sup>	39 <sup>[3]</sup>	39 <sup>[3]</sup>
$b_v$ (-)	3.8 <sup>[1]</sup>	3.8 <sup>[1]</sup>	3.8	3.8 <sup>[1]</sup>	3.8
$d_v$ (MPa)	1.52 <sup>[1]</sup>	1.52 <sup>[1]</sup>	3	1.52 <sup>[1]</sup>	3
$J_{max}$ ( $\mu\text{mol m}^{-2} \text{s}^{-1}$ )	213 <sup>[2]</sup>	132 <sup>[2]</sup>	230 <sup>[1]</sup>	180 <sup>[3]</sup>	180 <sup>[3]</sup>
$\phi_{PSII,ww}$ (-)	0.23 <sup>[4]</sup>	0.59 <sup>[5]</sup>	0.23 <sup>[5]</sup>	0.38 <sup>[6]</sup>	0.38 <sup>[6]</sup>
$b_\phi$ (-)	3.2 <sup>[4]</sup>	6.2 <sup>[5]</sup>	3.2 <sup>[5]</sup>	1.50 <sup>[6]</sup>	1.50 <sup>[6]</sup>
$d_\phi$ (MPa)	3.0 <sup>[4]</sup>	2.6 <sup>[5]</sup>	3.0 <sup>[5]</sup>	1.56 <sup>[6]</sup>	1.56 <sup>[6]</sup>
$\Gamma^*$ ( $\mu\text{mol mol}^{-1}$ )	40	42	50	10 <sup>[7]</sup>	10 <sup>[7]</sup>
$\chi$ (MPa <sup>-1</sup> )	0.12	0.08 <sup>[8]</sup>	0.12	0.08	0.04

<sup>[1]</sup> *Helianthus annuus* data fitting (Figure 2.1a); <sup>[2]</sup> Wullschleger (1993); <sup>[3]</sup> Collatz et al. (1992); <sup>[4]</sup> *Helianthus annuus* data fitting (Figure 2.2a); <sup>[5]</sup> *Triticum aestivum* data fitting (Figure 2.2a); <sup>[6]</sup> C<sub>4</sub> species data fitting (Figure 2.2b); <sup>[7]</sup> Jones (1992); <sup>[8]</sup> fitting of *Triticum aestivum* data presented by Kalapos et al. (1996).

### CO<sub>2</sub> concentrating mechanism

Water stress may reduce the activity of the C<sub>4</sub>-cycle and thus  $V_{P,max}$  (Eq. (84)). As already in the case of  $V_{c,max}$ , the literature reports contrasting experimental evidence regarding the impact of water stress on the CO<sub>2</sub> concentrating mechanism among different C<sub>4</sub> species. For example, for *Sorghum bicolor* Massacci et al. (1996) concluded that drought does not affect CO<sub>2</sub> concentrating mechanism, while for the same species

ContourAnsel et al. (1996) showed a marked impact of water stress on C<sub>4</sub>-cycle enzyme activity despite almost constant enzyme amounts. In contrast, a decrease in enzyme amount was observed in *Saccharum* sp. (Du et al. 1996).

Since in most models the C<sub>4</sub>-cycle has been assumed to be controlled solely by PEP carboxylase (e.g., Berry and Farquhar 1978, Collatz et al. 1992, von Caemmerer and Furbank 1999), here we focused on the impact of plant water status on this enzyme only, and accounted for the vulnerability of maximum PEP carboxylase,  $V_{P,\max}$  (Eq. (84)), by means of an empirical function,  $\eta_P(\psi_L)$ , describing the dependence of relative activity of PEP carboxylase on  $\psi_L$  (Eq. (2), with parameters  $a_P=1$ ,  $b_P$  and  $d_P$  to be fitted). In absence of more specific data, we assumed that a reduction of PEP carboxylase will similarly affect C<sub>4</sub>-cycle activity. Available experimental data relative to two species are compared to fitted  $\eta_P(\psi_L)$  curves in Figure 2.1b.

### Other parameters potentially impacted by leaf water status

Leaf CO<sub>2</sub> compensation point,  $\Gamma^*$ , has been recently shown to be mainly independent of leaf water status since specificity for Rubisco is mainly unchanged by water stress (Galmes et al. 2006). Similar conclusion can be reached by observing the  $A_{net}$  vs.  $c_i$  curves at low  $c_i$  values (such as those in Gimenez et al. 1992, Tezara et al. 1998, Tezara et al. 1999). Hence, no correction factor for this parameter was included in the model.

On the contrary, the scarce data available suggest that the respiration rate,  $R_d$ , decreases with decreasing leaf water potential (Flexas et al. 2006a). Since respiration has been widely represented as a fraction (generally 2%) of maximum carboxylation rate under well watered conditions (e.g., among many others, Collatz et al. 1992, Chen et al. 1994, von Caemmerer and Furbank 1999, von Caemmerer 2000), we assumed that  $R_d$  decreases similarly to  $V_{c,max}$  (Figure 2.1a).

### **2.2.2 Diffusive limitations to photosynthesis under drought**

In what follows, we discuss the modelling of the impacts of leaf water stress on vapour and CO<sub>2</sub> diffusivity, which in turn affect both leaf water status and CO<sub>2</sub> availability at the photosynthetic site. The following modelling assumptions are a compromise between simplicity and realism, and can be relaxed, if necessary, to improve realism of the overall predictions without changing the previous water stress-photosynthesis model.

### Stomatal conductance model

CO<sub>2</sub> assimilation rate is linked to CO<sub>2</sub> concentration gradient between atmosphere ( $c_a$ ) and stomatal cavity ( $c_i$ ) by Fick's law

$$A = g_{sba,CO_2}(c_a - c_i), \quad (3)$$

where  $g_{sba,CO_2}$  is the series of stomatal ( $g_{s,CO_2}$ ), leaf boundary layer ( $g_{b,CO_2}$ ) and atmospheric ( $g_{a,CO_2}$ ) conductances to CO<sub>2</sub> (cuticular conductance is here neglected). To fully characterize the system, Eq. (3) requires an additional equation relating such conductances to other variables. As a first approximation,  $g_{b,CO_2}$  and  $g_{a,CO_2}$  are assumed to be constant (Table 2.1). As for  $g_{s,CO_2}$ , a variety of stomatal functions have been proposed, differing in level of detail and ability to account for stomatal closure under leaf water stress and other factor possibly relevant to stomatal functioning, such as solar radiation, vapour pressure deficit (VPD) and abscisic acid (ABA) dynamics (e.g., Jarvis 1976, Norman 1982, Tardieu and Davies 1993, Leuning 1995, Dewar 2002, Gao et al. 2002, Buckley et al. 2003, Tuzet et al. 2003). Since, as discussed below, available data are mainly collected from plants growing under controlled conditions (i.e., constant air temperature, air humidity and irradiance during the day), the dependence of stomatal dynamics on environmental conditions may be regarded as of secondary importance for our current scope. Hence, we chose the simplest stomatal function among those available in the literature, the Norman model, which is based on experimental observations that stomatal conductance appears to be regulated so that a nearly constant

$R_c=c_i/c_a$  is maintained (e.g., Wong et al. 1979, Pearcy and Ehleringer 1984). Under well watered conditions, such ratio only depends on the plant functional type, with higher values in C<sub>3</sub> plants (Wong et al. 1979, Jones 1992). Nevertheless, a reduction of  $c_i/c_a$  under moderate water stress has been observed in some C<sub>3</sub> and C<sub>4</sub> species (e.g., *Triticum aestivum* in Kalapos et al., (1996), *Hordeum vulgare* in Lal et al., (1996) and *Sorghum bicolor* in Williams et al. (2001)), but not in others (e.g., *Amarathus cruentus* and *Zea mays*; Lal and Edwards (1996)). As drought becomes more severe, a subsequent increase in  $c_i/c_a$  has also been observed in some experiments, both in C<sub>3</sub> (e.g., *Vicia faba* in Lal et al. (1996), *Abutilon theoprastris* in Luo (1991)) and C<sub>4</sub> (e.g., *Saccharum* sp. in Du et al. (1996), *Panicum coloratum* in Seneweera et al. (2001)) species: such an increase has been explained either by the presence of non-stomatal limitations (e.g., Luo 1991, Du et al. 1996) or by patchy stomatal closure (e.g., Chaves 1991, Flexas et al. 2004a). As a first approximation, we accounted for such variability by introducing a linear dependence of  $R_c$  on  $\psi_L$ ,

$$R_c(\psi_L) = R_{c,ww} - \chi |\psi_L|. \quad (4)$$

Experimental data suggest values for  $R_{c,ww}$  of 0.7 and 0.4 for C<sub>3</sub> and C<sub>4</sub> species respectively (Wong et al. 1979, Jones 1992), while  $\chi$  is in the range 0.08 to 0.12 MPa<sup>-1</sup> (see, e.g., data in Kalapos et al. (1996)); note that when  $\chi = 0$  Eq. (4) reduces to the Norman model. Thanks to its simplicity, this model is robust to numerical instabilities that may occur with other stomatal models (e.g., Leuning model; see Zhan et al. (2003)).

Clearly, the simple dependence of  $R_c$  on  $\psi_L$  in Eq. (4) might be easily substituted by more complex behaviours. The effects of possible increases in  $R_c$  under severe stress will be considered in future contributions.

### Mesophyll conductance model

Leaf water stress may cause a decrease in the mesophyll conductance, i.e. the conductance of the path from the stomatal cavity to the mesophyll (e.g., O'Toole et al. 1976, Hanson and Hitz 1982 and references therein, Grassi and Magnani 2005). Unfortunately, however, the mechanisms that down-regulate mesophyll conductance under drought are not completely known (Warren and Adams 2006), although mesophyll and stomatal conductances appear to be co-regulated under water stress (Flexas et al. 2004b) and there are some indications of a linear relation between them under soil water deficit in several species (Centritto et al. 2003, Galmes et al. 2006, 2007, Warren 2008). In absence of more detailed data, on these empirical bases, we assumed  $g_m = \alpha_m g_s$ , from which CO<sub>2</sub> concentration in the mesophyll follows as  $c_m = c_i - A/g_m$ . The parameter  $\alpha_m$  appears to differ among species, ranging between 0.77 and 2.31 (Galmes et al. 2006, Warren 2008); it should be noted that to avoid unrealistic results  $\alpha_m$  and  $\chi$  shall be chosen in such a way that  $\alpha_m > R_c(\psi_L)^{-1} - 1$ .

## 2.3 Results and discussion

We first analyzed the impact of decaying leaf water potential on plant activity. Since most experiments are performed in controlled environments with constant air humidity and temperature, we limited our analysis to fixed atmospheric conditions. To fully assess plant response to water stress, leaf water status was then coupled to soil moisture evolution (Appendix B) thus obtaining the decrease of assimilation rate with soil water availability during a dry-down. Model results were compared to experimental data relative to a variety of species.

Simulation parameters are summarized in Table 2.1 and Table 2.2. For C<sub>3</sub> plants, the species-specific  $V_{c,max,ww}$  and  $J_{max}$  reported in Wullschleger (1993) were used; for C<sub>4</sub> plants, given the scarcity of available data, as a first approximation  $V_{c,max,ww}$  and  $J_{max}$  were assumed to be equal for all species. As for the impact of water stress on metabolic processes (Eq. (2)), when possible parameter sets were chosen among those available for the species under analysis (this was the case of parameters for *Helianthus annuus*, and some for *Sorghum bicolor* and *Triticum aestivum*). When data for the species under analysis were not available, we chose parameter sets among those determined for other species (Figure 2.1 and Figure 2.2) in such a way to maximize the agreement between data points and model results. It should be noted, however, that the only available parameter set regarding the impact of water stress on  $V_{c,max}$  was the one for the relatively stress-sensitive C<sub>3</sub> *Helianthus annuus* (Figure 2.1a), which is clearly not adequate for

some more stress-resistant species. Thus, for stress-resistant species, we assumed a decrease in  $V_{c,max}$  with decreasing  $\psi_L$  slower than the one observed in *Helianthus annuus*. Such an assumption is justified by the absence of more specific data and by uncertainties in determining the impact of water stress on this parameter (e.g., Tezara et al. 1999, Flexas et al. 2006b). Finally, environmental conditions (i.e., atmospheric CO<sub>2</sub> concentration  $c_a$ ; air temperature  $T_a$ ; air humidity  $q_a$ ; shortwave irradiance  $\phi_{sw}$ ; direct soil evaporation  $E_v$ ) and soil parameters (i.e., average root depth  $Z_r$ ; soil porosity  $n$ ; saturated hydraulic conductivity  $K_{sat}$ ; soil water potential at saturation  $\bar{\psi}_s$ ; exponent of soil retention curve  $b$ ; see Appendix B) were set equal to those in the corresponding experimental setup.

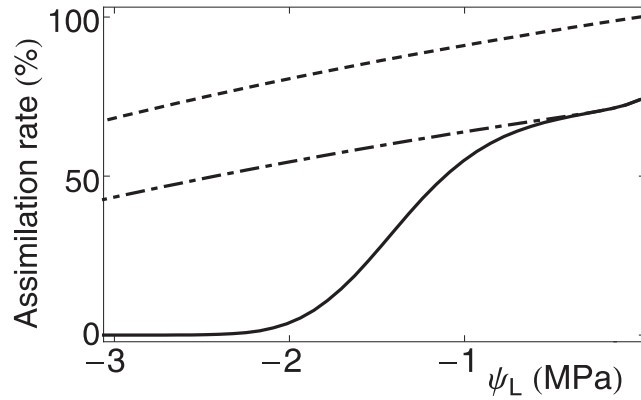


**Figure 2.3:** Normalized C<sub>3</sub> assimilation rate as a function of leaf water potential when the different limitations to photosynthesis are gradually added: water-stress reduced stomatal conductance (Eq. (4)) but infinite mesophyll conductance ( $\alpha_m \gg 1$ ) and no metabolic limitations (dashed line), stomatal and mesophyll conductances only (diffusive limitation; dash-dotted line), and diffusive and metabolic limitations (full model; solid line). The species-specific parameters refer to *Helianthus annuus* (Table 2.2); all the other parameters are listed in Table 2.1 environmental conditions are as those described in Gimenez et al. (1992).

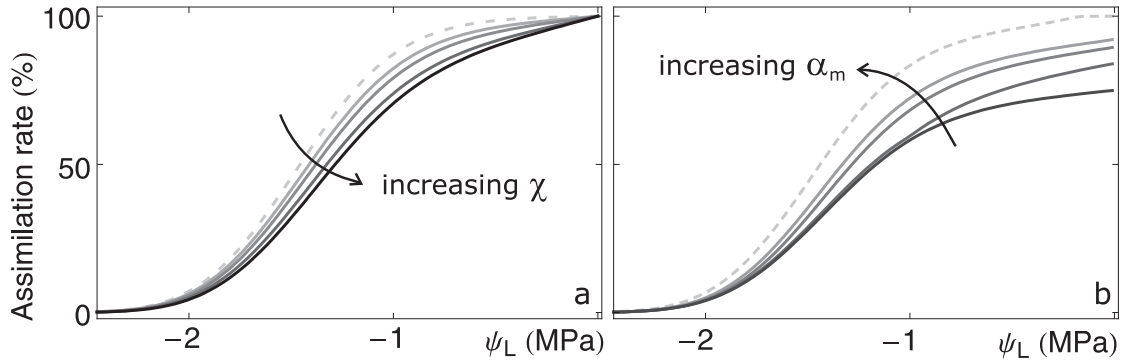


**Figure 2.4:** Normalized  $C_3$  assimilation rate as a function of leaf water potential,  $\psi_L$ , for a range of parameters of the stomatal and mesophyll conductance models: a) the decrease rate of  $R_c$  with  $\psi_L$ ,  $\chi$  (Eq. (4)), varies in the range 0 (i.e., Norman model; dashed line) to  $0.16 \text{ MPa}^{-1}$ ; b) the ratio between mesophyll and stomatal conductances,  $\alpha_m$ , varies in the range 1.15 to 4.15, and assimilation is normalized with respect to values obtained for  $\alpha_m \rightarrow \infty$  (dashed line). The species-specific parameters refer to *Helianthus annuus* (Table 2.2); all the other parameters are listed in Table 2.1; environmental conditions are as those described in Gimenez et al. (1992).

### 2.3.1 $\text{CO}_2$ assimilation rate and leaf water potential

In this section, we first assess the contribution of different limitations to net assimilation as a function of leaf water potential, and then compare results of the full model to experimental data.

To evaluate the ability of the model to predict the role of different limitations, we compared the assimilation rate as a function of leaf water potential when such limitations are gradually added. We first considered the impact of the sole stomatal conductance, then we combined mesophyll and stomatal conductances (i.e., diffusive

limitations), and finally employed the full model with both diffusive and metabolic limitations. As shown in Figure 2.3 for C<sub>3</sub> *Helianthus annuus*, at high leaf water potentials the main limitation to assimilation rate is diffusive, while, as water stress progresses, the metabolic limitation becomes more and more relevant, in agreement with several experimental observations (e.g., Kaiser 1987, Lawlor 2002, Flexas et al. 2004b, Grassi and Magnani 2005). We also performed a sensitivity analysis on the parameters of the diffusive limitation models, i.e.  $\chi$  and  $\alpha_m$ , by comparing the resulting assimilation rates at different  $\psi_L$  predicted by the full model (Figure 2.4 for C<sub>3</sub> species). As expected, in C<sub>3</sub> species, a faster decrease in stomatal CO<sub>2</sub> (i.e., a higher  $\chi$ ; Eq. (4)) results in a decreased photosynthetic rate; such an effect is particularly relevant at mild water stress, while it tapers off under extreme stress, when assimilation rate is depleted mainly by metabolic limitations (Figure 2.4a). For reference the case of the Norman model ( $\chi = 0$ ) is reported as well (dashed line). A similar pattern is observed in C<sub>4</sub> species (not shown), since  $\chi$  sets the availability of CO<sub>2</sub> in the stomatal cavity, and cannot be offset by the C<sub>4</sub>-cycle. As for mesophyll conductance, in C<sub>3</sub> species lower values of  $\alpha_m$  (i.e., a lower mesophyll conductance) result in a decreased assimilation rate even under well watered conditions and a higher sensitivity to decreasing  $\psi_L$ , due to the overall lower availability of CO<sub>2</sub> at the photosynthetic site (Figure 2.4b). For reference the case of  $\alpha_m \rightarrow \infty$ , corresponding to the often employed assumption of  $c_i=c_m$ , is reported as well

(dashed line). The impact of  $\alpha_m$  is less relevant in C<sub>4</sub> species (not shown), because the CO<sub>2</sub> concentrating mechanism is able to partially offset the changes in  $\alpha_m$ .

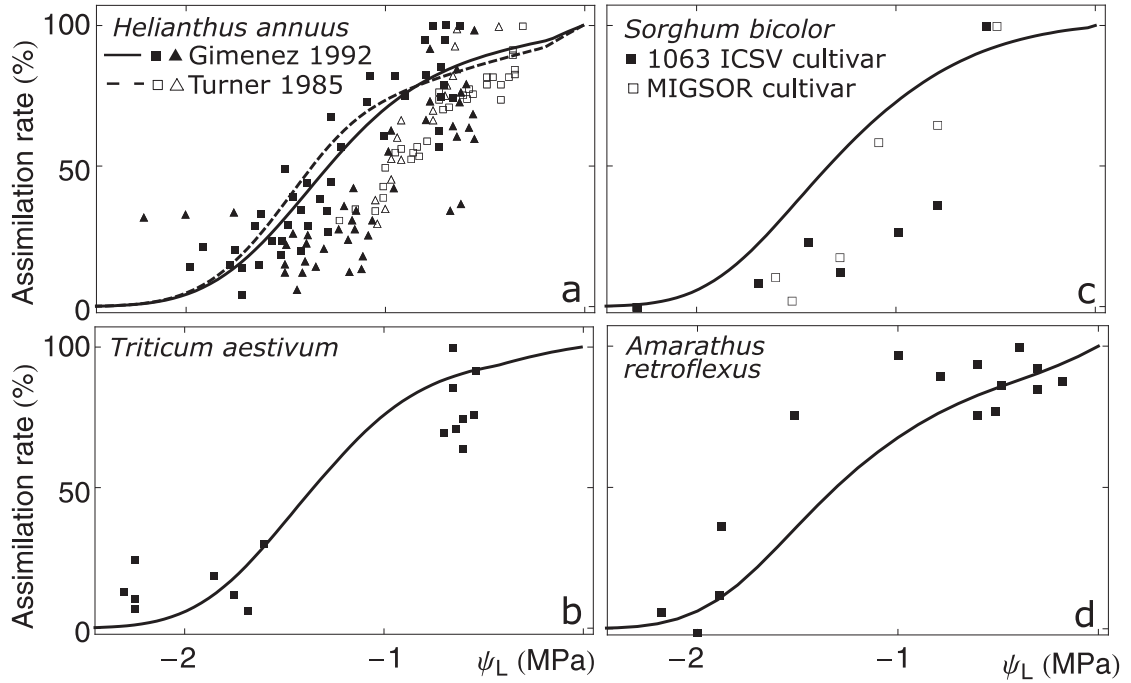


**Figure 2.5:** Modelled  $A = A(\psi_L)$ , normalized by well-watered assimilation rate, compared to measured data (symbols) for C<sub>3</sub> (left column) and C<sub>4</sub> species (right column) that cease assimilation around -2 MPa. Species-specific parameters are as in Table 2.2; all the other parameters are listed in Table 2.1. Environmental conditions are chosen equal to the conditions in the corresponding experiments (see sources of data for details), hence two different environmental conditions are used in a). Data: a) filled boxes refer to SH cultivar, filled triangles to Sungro cultivar; open boxes and open triangles are relative to VPD=1 kPa and VPD=2.5 kPa respectively b) *Triticum aestivum*: Siddique et al. (2000); c) *Sorghum bicolor* L. cultivars: ContourAnsel et al. (1996); d) *Amaranthus retroflexus* Ward et al. (1999).

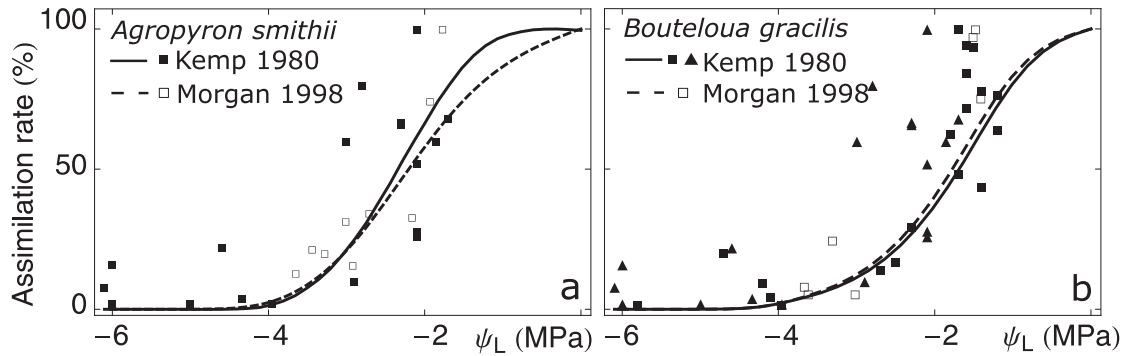


**Figure 2.6:** Modelled  $A = A(\psi_L)$ , normalized by well-watered assimilation rate, compared to measured data (symbols) for  $C_3$  *Agropyron smithii* (a) and  $C_4$  *Bouteloua gracilis* (b). Species-specific parameters are as in Table 2.2; all the other parameters are listed in Table 2.1. Environmental conditions are chosen equal to the conditions in the corresponding experiments (see sources of data for details).

Modeled results for net assimilation rate as a function of leaf water potential, accounting for both diffusive and metabolic limitations (Eq. (1) to (4) and (82) to (87)), were compared with experimental data for various  $C_3$  and  $C_4$  species (Figure 2.5 and Figure 2.6). Regardless of functional type, experimental results show that some species cease assimilation already at  $\psi_L \cong -2$  MPa (Figure 2.5), while others are able to cope with leaf water potentials as low as -4 MPa without completely halting assimilation (Figure 2.6): crop species are the most vulnerable to low leaf water potentials. Moreover, among species that practically cease assimilation at similar leaf water potentials, there are differences in the way in which this takes place. For example, assimilation rate in *Amarathus retroflexus* is reduced to 50% at  $\psi_L \cong -1.7$  MPa (Figure 2.5d), while a similar reduction is already apparent in *Sorghum* cultivars at  $\psi_L \cong -0.8$  MPa (Figure 2.5c). A

comparison of datasets relative to the same species shows intra-specific variability, which may be at least partially explained by differences in cultivars (Figure 2.5c) or other factors in independent experiments, such as nutrient availability or leaf age (Figure 2.5a).

Among the most stress-sensitive plants (Figure 2.5), data measured in C<sub>3</sub> *Helianthus annuus* and *Triticum aestivum* are reasonably well described by the proposed model, when using the dependence of  $V_{c,max}$  on  $\psi_L$  observed in *Helianthus annuus* (Figure 2.1a) and their respective species-specific dependences of quantum yield on  $\psi_L$  (Figure 2.2a). For C<sub>4</sub> species, the model captures the overall decrease in assimilation rate and the leaf water potential values at which photosynthesis practically ceases, but it is not adequate at intermediate levels of  $\psi_L$ , due at least in part to scarcity of species-specific data.

For more stress-resistant species, we assumed a slower decrease in  $V_{c,max}$  with decreasing  $\psi_L$  than the one observed in *Helianthus annuus* (Table 2.2). The obtained model is then able to describe the main features of the decrease in  $A$  with  $\psi_L$  in C<sub>3</sub> *Agropyron smithii* and C<sub>4</sub> *Bouteloua gracilis* (Figure 2.6), in particular leaf water potential at which assimilation is practically ceased. However, the impact of mild water stress on assimilation rate is slightly overestimated by the model: this could possibly be improved once specific data become available.

### 2.3.2 Soil moisture dry-down

The previous analysis showed marked differences among species in reduction of assimilation rate with decreasing leaf water potential. It should be emphasized that, since  $\psi_L$  depends on soil water conditions through the SPAC dynamics, a full assessment of plant response to water stress must include the simultaneous analysis of soil moisture evolution and plant transpiration. To this purpose, assimilation and stomatal models described above were coupled to a soil moisture balance equation (Eq. (91)). The latter was solved numerically in an explicit form and the resulting temporal evolution of soil moisture was used to determine the other variables representing the SPAC. We focused on long dry-down periods starting from well-watered conditions, and obtained the hourly soil moisture dynamics and daily total assimilation during a dry-down.

Modelled daily assimilation and transpiration rates decrease monotonically with water stress, in agreement with observations (e.g., Federer 1982), and clearly underline the existence of different regimes in plant-water interactions (Figure 2.7). At high soil water levels, an unstressed regime is characterized by daily assimilation and transpiration rates that are not affected by soil moisture (well-watered conditions). Below a relatively narrow range of soil moisture in which plant activity progressively worsens, a stressed regime is evident with almost completely halted CO<sub>2</sub> assimilation.

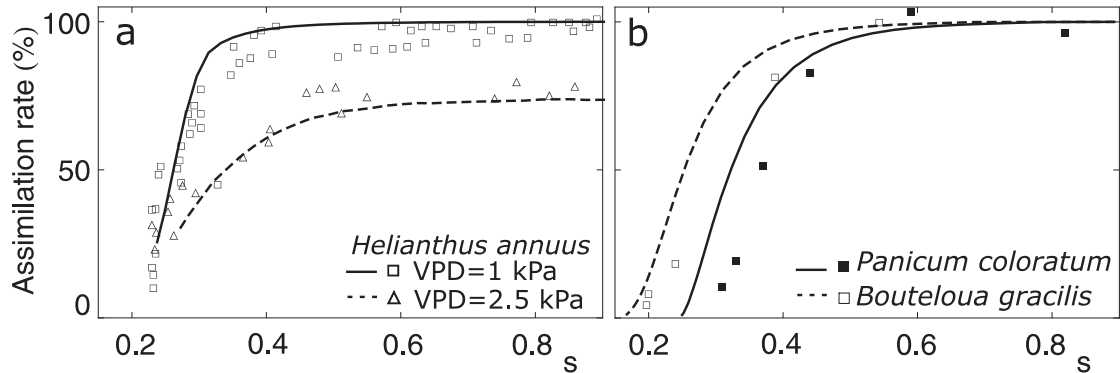


**Figure 2.7:** Modelled relative assimilation rate as a function of soil moisture compared to data measured in C<sub>3</sub> and C<sub>4</sub> plants (panels a, b respectively). Environmental conditions are set in accordance to experimental conditions (see data sources for details); coherently, soil parameters refer to sandy loam for *Helianthus annuus* and *Bouteloua gracilis*, and to loam for *Panicum coloratum* (for values of soil parameters see, e.g., Rodriguez-Iturbe and Porporato 2004); all the other parameters are listed in Table 2.1 and table 2.2, with the exception of  $\alpha_m$  which was set equal to 4.15 for the simulations on left panel to defer the occurrence of numerical instabilities to lower soil moisture values; to cover the whole soil moisture range, deep infiltration and direct soil evaporation (Eq. (91)) were set to 0. Source of data: a) *Helianthus annuus*, Turner et al. ((1985); soil moisture is derived from the measured extractable soil water assuming zero extractable soil water at  $s=0.2$  and 100% extractable soil water at soil saturation). b) *Panicum coloratum*, Seneweera et al. (2001); *Bouteloua gracilis*, Morgan et al. ((1998); averages across water and CO<sub>2</sub> treatments).

The modelled relationship between soil moisture and assimilation rate were then compared to experimental data independent of those employed in model calibration (Figure 2.7). Model results well describe data for C<sub>3</sub> *Helianthus annuus* under both VPD conditions (despite VPD not being explicitly included in stomatal model), capturing the soil moisture at which CO<sub>2</sub> assimilation begins to be seriously impacted by water stress (Figure 2.7a); however, due to numerical instabilities we were unable to prolong the

simulation to reach the point at which assimilation is completely halted. Fewer data were available for model calibration for C<sub>4</sub> species, and this probably explains why the model captures the onset of stress, but slightly overestimates CO<sub>2</sub> assimilation at low soil moisture (Figure 2.7b).

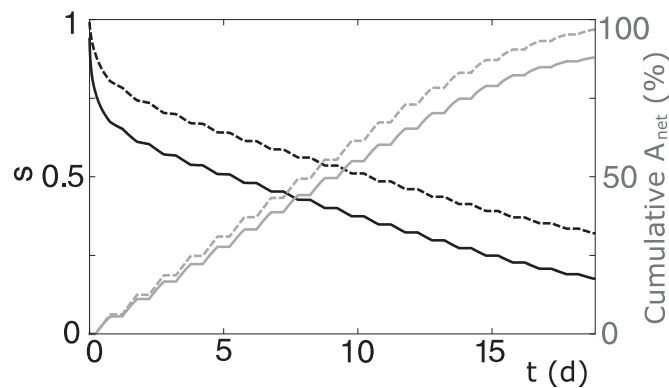


**Figure 2.8:** Soil moisture dynamics (black lines) and cumulative normalized assimilation (grey lines) during a 19 day dry-down in C<sub>3</sub> *Helianthus annuus* for two different soils: solid lines, loamy sand; dashed lines, loam (for values of soil parameters see, e.g., Rodriguez-Iturbe and Porporato 2004). All the parameters are as in Figure 2.7a, with the exception of non-zero deep infiltration.

To further investigate the impact of different environmental conditions, the model was used to estimate soil moisture dynamics and cumulative assimilation for *Helianthus annuus* assuming two different soil types over a 19-day dry-down (Figure 2.8). While soil moisture is constant at night (direct soil evaporation was neglected in this example), during the day losses by plant water uptake are significant and clearly related to soil features. The depletion of soil moisture is considerably faster in sandy soil

all the other variables being the same (Figure 2.8, dark solid line): early during the dry down, such difference is due to higher deep infiltration typical of coarser soils (Eq. (91)); later on, when leakage becomes negligible, water losses are mainly controlled by SPAC. The interplay between soil water potential and soil root conductivity results in lower  $\psi_L$  in coarser soil, thus explaining the lower cumulative net assimilation (Figure 2.8). Even when deep infiltration is prevented (as it was the case in Figure 2.7), soil moisture depletion is faster in coarser soils because of the higher soil-root conductance (Eq. (89)), but the differences between soil types are less marked (not shown).

## **2.4 Conclusions**

The proposed model integrates the dependences on leaf water status of individual processes involved in photosynthesis, and predicts the resulting CO<sub>2</sub> assimilation rate as a function of leaf water potential. Coupling such assimilation model to the SPAC allowed us to describe plant activity during a dry-down. The obtained CO<sub>2</sub> assimilation rates as a function of leaf water potential and soil moisture are in good agreement with independent data.

Despite its complexity, the model was successfully employed to assess which limitation mechanism is most controlling at different degrees of water stress. As such, it may also serve as a tool to investigate the impact of environmental conditions and soil characteristics on assimilation rates in situations which may be difficult to reproduce in

*ad hoc* experiments, as well as a mean to test different hypotheses and guide the development of new detailed experiments. Moreover, the results from the present model help to provide a more physiological basis to upscaled (e.g., daily) semi-empirical relationships, used in stochastic ecohydrologic models to represent the interrelationship between soil moisture and plant dynamics (Dingman 1994, Daly et al. 2004b, Rodriguez-Iturbe and Porporato 2004).

Future applications will be used to interpret the reported shifts in C<sub>3</sub> and C<sub>4</sub> dominance patterns, crop productivity, and response to CO<sub>2</sub> increase and hydroclimatic variability (Collatz et al. 1998, Sage et al. 1999, Sage and Kubien 2003). In fact, when cumulated over longer periods (e.g., a growing season), the observed differences in assimilation rate response to leaf water potential and in rate of water use efficiency can produce non negligible effects in the soil water balance and ecosystem productivity. However, a long-term assessment of the response of plant productivity to water stress will require a full coupling with environmental condition (i.e., the inclusion of the feedbacks between plant activity and atmospheric boundary layer).

### **3 Traditional and micro-irrigation with stochastic soil moisture**

This chapter is based on the manuscript Vico G. and A. Porporato, Irrigation with stochastic soil moisture, *Water Resources Research*, under revision.

#### **3.1 Introduction**

Globally, irrigated agriculture is the primary user of freshwater, accounting for nearly 85% of total water consumption (Jury and Vaux 2007), and 40% of the total food production derives from irrigated agriculture (Feres and Soriano 2007). Agriculture-related water demand is expected to increase in the near future, in face of foreseen alterations of rainfall regime due to climate change, and increased food, fiber and biofuel demands. Irrigation scheduling is part of the complex problem of water-resource optimization (English et al. 2002). Sustainable irrigation must harmoniously balance the concurring water demands for industrial and municipal uses, and the needs for natural ecosystems, especially in water-limited regions. Water resources managers are interested in knowing in advance the water demand for agriculture, in relation to the different irrigation practices and crop types, to allocate water for irrigation purposes and to plan investments for maintenance and improvements of irrigation systems. On the other hand, farmers are interested in maximizing profits by maximizing crop yield while

minimizing irrigation costs. These tasks, however, are highly complicated by rainfall intermittency and unpredictability.

Irrigation has the function of supplementing natural rainfall, to meet crop water requirements, i.e. to avoid plant water stress and the ensuing reduction in crop yield and/or quality. Demand-based irrigation often relies on soil water balance calculations or on directly tracking soil moisture or plant water status (Jones 2004) to determine the right amount and timing of water to be supplied. As the root zone dries out and plant water potential is lowered, plants respond with a number of adjustments (e.g., changes in patterns of resource allocation, CO<sub>2</sub> assimilation and respiration reduction, stomatal closure; see, e.g., Hsiao (1973), Porporato et al. (2001)), which often result in reduced crop productivity. The onset of water stress can reasonably be associated with the soil moisture level at incipient stomatal closure,  $s^*$ , a threshold that in general depends on soil and plant characteristics (Hsiao 1973, Porporato et al. 2001). If soil moisture further decreases, permanent wilting and total loss of yield may occur.

We will focus here on stress-avoidance irrigation, although a minor stress level may be acceptable when water supply is limited (English 1990), or even desirable for quality purposes of specific products (e.g., some fruit trees and vines; Fereres and Soriano (2007) and references therein). This so-called deficit irrigation is analyzed in Chapter 4. Traditional practices by furrow, sprinkler or flood irrigation typically consist of repeated, infrequent but massive applications of water that fill the root zone up to

field capacity (loosely defined here as the point where drainage from the root zone becomes significant). Ideally, unless time scheduling constraints are present or in case of reduced water availability, such applications are done just before soil moisture hits stress level. Conversely, modern irrigation principles advocate a more finely-tuned irrigation, by means of micro-irrigation techniques (e.g., drip irrigation, micro-sprinklers or subsurface emitters; Hillel (2004)), in which water is supplied continuously to avoid water stress, at the same time minimizing the water use and water losses through runoff and deep percolation associated to high soil moisture levels. Reduced water losses also result in reduced leaching of soluble chemicals (e.g., pesticides and fertilizers), but may also increase the risk of soil salinization (Bras and Seo 1987) or reduce recharge to groundwater and related streams (English et al. 2002).

We analyze theoretically these two different forms of irrigation, and compare them in terms of total water volumes and frequency under conditions of stochastic rainfall. Specifically the two contrasting irrigation schemes are idealized as follows: i) a modern micro-irrigation scheme with continuous supply of water which maintains the root-zone soil moisture just above the stress level, and ii) a traditional irrigation scheme, consisting in concentrated applications of water, when soil moisture reaches the same stress level, that bring soil moisture back to field capacity.

We offer exact analytical solutions for random timing and amounts of rainfall. Differently from other irrigation analyses that considered total irrigation needs over the

average growing season (e.g., English et al. (2002) and references therein), processes are resolved here at the daily level. Such time scale is intermediate between sub-daily irrigation models for daily management at the farm level (e.g., California Irrigation Management Irrigation System), and seasonal models, for long-term resource management and infrastructure planning at the regional scale (English 1990). Although simplified, our approach is physically based and takes into account the most important source of uncertainty in soil moisture variability (i.e., rainfall) with a stochastic approach. The soil moisture model used here builds upon previous stochastic soil moisture models employed in ecohydrology (Rodriguez-Iturbe et al. 1999, Rodriguez-Iturbe and Porporato 2004). Within the vast literature on irrigation, this contribution may provide a valuable alternative to the more sophisticated, but fully numerical, optimization schemes that include the effect of stochastic rainfall variability (see, among many others, Bras and Cordova (1981), Georgiou and Papamichail (2008), Protopapas and Georgakakos (1990), Zhang and Oweis (1999) and references therein). The analytical solutions presented here clearly show the role of the different parameters and the relationships among the main soil, vegetation and climate characteristics. Our results suggest that traditional irrigation requires larger amounts of water than micro-irrigation; the extra amount of water is lost to runoff and deep percolation. Furthermore, transpiration rate and rainfall patterns are the main drivers of irrigation requirements. Hence, despite its simplicity, the proposed model may offer guidance for water

infrastructure planning, crop selection, and choice of irrigation scheme, well tailored to regional climatic features.

The two idealized irrigation schemes are optimal in the sense that they avoid crop water stress while minimizing water losses by percolation and runoff. Furthermore, they cover the two extremes cases of continuous and fully concentrated irrigation. A generalized traditional irrigation scheme, including deficit irrigation, will be pursued in Chapter 4. We assume that plant productivity is not nutrient limited and do not discuss salinity problems. Moreover, we only consider statistically steady-state conditions for time-homogeneous vegetation and climatic conditions during the growing season. The impact of such simplified hypothesis will be described in detail.

### **3.2 Model formulation**

Assuming negligible lateral soil moisture fluxes, the water balance averaged over the root zone reads

$$nZ_r \frac{ds(t)}{dt} = R(t) + I(s, t) - ET(s) - LQ(s, t). \quad (5)$$

where  $n$  is soil porosity,  $Z_r$  is the active soil depth (where most of the roots are located),  $s$  is the relative soil moisture,  $s = (\theta - \theta_r)/n$ , with  $\theta$  volumetric soil moisture and  $\theta_r$  the residual water content (here assumed to coincide with wilting point for simplicity). Note that here  $s$  represents the plant-accessible water ( $\theta_r/n$  ranging between 0.08 and 0.19 for loamy sand and loam respectively; Laio et al. (2001)).

The inputs to the soil moisture balance are rainfall and irrigation. Rainfall  $R(t)$  is modeled as instantaneous events occurring according to a marked Poisson process of rate (mean frequency of rainfall events)  $\lambda$ , and with exponentially distributed depths with mean  $\alpha$  (Rodriguez-Iturbe et al. 1999, Rodriguez-Iturbe and Porporato 2004).  $R(t)$  may be purged of canopy interception, which reduces both the frequency of effective rainfall and its depth (Rodriguez-Iturbe et al. 1999, Daly et al. 2008). Accordingly, rainfall process is censored,  $\lambda' = \lambda e^{-\Delta/\alpha}$ , where  $\Delta$  is the crop-dependent rainfall depth threshold below which no rainfall reaches the ground (Rodriguez-Iturbe et al. 1999), and the mean rainfall depth is reduced as  $\alpha' = \kappa\alpha$  (Daly et al. 2008). Irrigation is a state-dependent input as its timing and amount typically depend on soil moisture status. Two different schemes will be analyzed in the next sections.

The main soil water losses are accounted for in Eq. (5):  $ET(s)$  is the rate of loss of soil moisture due to evapotranspiration (ET), and  $LQ(s,t)$  combines deep infiltration and runoff losses. Daily ET is assumed to vary in time only through soil moisture. While for most of the analytical results reported below the specific form of  $ET(s)$  is not important, in the quantitative applications of Sec. 3.3, a piecewise linear dependence on soil moisture will be assumed (Rodriguez-Iturbe et al. 1999, Rodriguez-Iturbe and Porporato 2004). To preserve analytical tractability, the impacts of day-to-day variability on transpiration rate to be ascribed to plant growth and variable environmental conditions (chiefly, air temperature and humidity, and solar radiation) are neglected.

While environmental conditions in general have a secondary effect if compared to the impact of rainfall-induced soil moisture variability, plant growth during the growing season may be more relevant, in particular when annual crops are considered. In fact, even though transpiration rate per unit leaf area may remain substantially constant over the entire growing season under constant soil moisture conditions, transpiration rate per unit ground area ( $ET(s)$ ) is altered by changes in leaf area index. Nevertheless, to keep analytical tractability, the dependence of transpiration rate on soil moisture,  $ET(s)$ , will be assumed to be constant in time, and interpreted as an average value over the growing season. Deep infiltration and runoff losses,  $LQ(s, t)$ , are also treated here in a simplified manner, as in Milly (2001) and Porporato et al. (2004). Accordingly, they are assumed to take place instantaneously (at the daily time scale) whenever soil moisture reaches a threshold  $s_1$ , typically around soil field capacity or slightly above it. Thus, when (effective) rainfall exceeds the available storage capacity,  $nZ_r(s_1 - s)$ , any excess is immediately lost as runoff and deep infiltration. In vegetated ecosystems and in agricultural fields, where the mechanism of rainfall-excess runoff production is dominant and soil tends to be well drained, this assumption, which allows analytical tractability, is quite realistic (see also Rigby and Porporato (2006)).

The water balance in Eq. (5) will be used to investigate the impact of different irrigation schemes on soil moisture probability distribution at steady state, and the requirements of such schemes in terms of irrigation frequency and water volumes. As a

term of comparison, the case of rainfed agriculture (i.e., no irrigation) will be discussed first. The irrigation schemes are assumed to be activated when the onset-of-stress threshold  $s^*$  is reached (i.e., a stress-avoidance irrigation is performed). Evapotranspiration and mean rainfall depth will be normalized by  $nZ_r$ , as  $\rho(s) = ET(s)/nZ_r$  and  $\gamma = \alpha'/nZ_r$ , respectively.

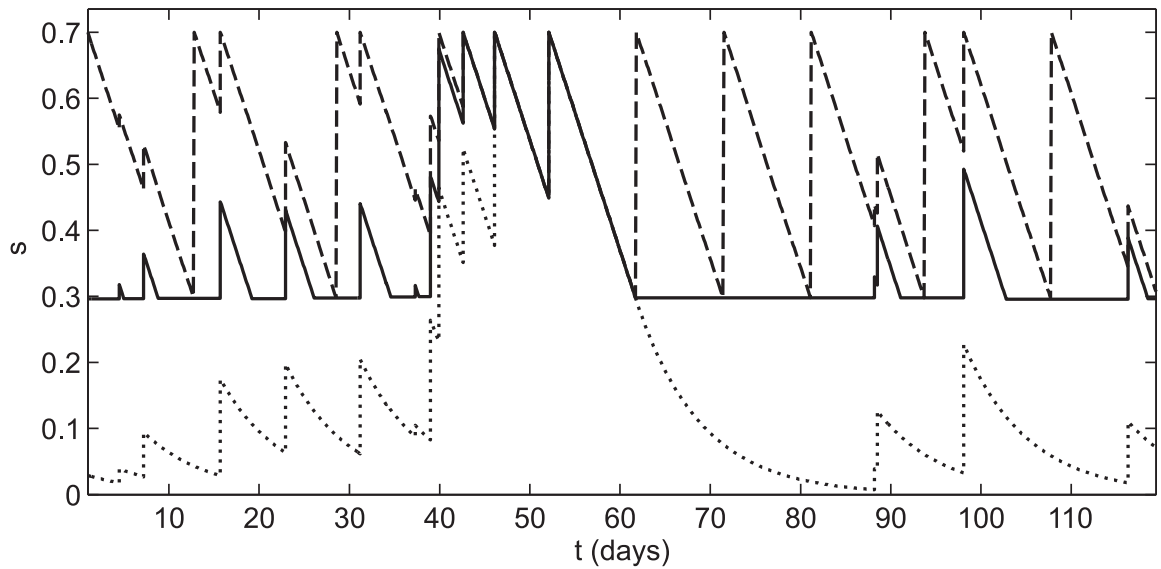


**Figure 3.1:** Example of soil moisture time series for rainfed agriculture (dotted line), micro-irrigation (solid line), and traditional irrigation (dashed line). Soil is sandy loam, with  $n = 0.43$ ,  $Z_r = 25$  cm (Rodriguez-Iturbe and Porporato 2004),  $s^* = 0.3$  and  $s_1 = 0.7$ . Average precipitation depth is  $\alpha = 15$  mm with interception parameters  $\Delta = 1$  mm and  $\kappa = 0.9$ , and rainfall frequency  $\lambda = 0.15$  day<sup>-1</sup>. Evapotranspiration rate is  $E_{\max} = 0.45$  cm day<sup>-1</sup>.

Examples of numerically generated soil moisture time series under the two schemes are compared in Figure 3.1, where the case of no irrigation (the so-called rainfed agriculture) is also shown.

### 3.2.1 Rainfed agriculture (no irrigation)

In the absence of irrigation, the previous nonlinear stochastic differential equation for the soil water balance, describing the soil moisture evolution at the daily level, has been extensively analyzed in previous contributions (Rodriguez-Iturbe and Porporato 2004, and references therein). Figure 3.1 (dotted line) shows a realization of the stochastic soil moisture process during a growing season: plants are water stressed whenever soil moisture is below the point of incipient stomatal closure,  $s^*$ . The evolution of the probability density function (pdf) of soil moisture for  $0 < s \leq s_1$  is described by the master or Chapman-Kolmogorov equation (Rodriguez-Iturbe et al. 1999, Rodriguez-Iturbe and Porporato 2004)

$$\frac{\partial}{\partial t} p(s, t) = \frac{\partial}{\partial s} [\rho(s)p(s, t)] - \lambda' p(s, t) + \lambda' \int_0^s p(u, t) f(s - u, u) du, \quad (6)$$

where  $f(y, s)$  is the pdf of the soil moisture jumps due to the difference between the instantaneous rainfall and the runoff and percolation events, i.e.

$$f(y, s) = \gamma e^{-\gamma y} + \delta(y - s_1 + s) e^{-\gamma(s_1 - s)} \quad (\text{Porporato et al. 2004, Rodriguez-Iturbe and Porporato 2004}).$$

Because of our simplified treatment of runoff and deep infiltration, the

soil moisture process is bounded at  $s_1$ . Also, due to the specific form of  $f(y, s)$ , Eq. (6) can also be written in the form (Daly and Porporato 2006b)

$$\frac{\partial}{\partial t} p(s, t) = -\frac{\partial}{\partial s} J(s, t), \quad (7)$$

where the probability current  $J(s, t)$  is

$$J(s, t) = -\rho(s)p(s, t) + \lambda \int_0^s e^{-\gamma(s-u)} p(u, t) du. \quad (8)$$

A general solution of either Eq. (6) or Eqs. (7) and (8) presents serious mathematical difficulties. We focus here on steady state conditions, i.e.  $\partial p(s, t)/\partial t = 0$ , in which case the probability current is constant (see Eq. (7)). In particular, for rainfed agriculture,  $J(s) = 0$  and the effect of the bound is reduced to a renormalization of the steady state pdf in the unbounded case (Rodriguez-Iturbe et al. 1999), i.e.,

$$p(s) = \frac{C}{\rho(s)} \exp\left(-\gamma s + \lambda \int_{s^*}^s \frac{du}{\rho(u)}\right), \quad (9)$$

for  $0 < s \leq s_1$ . Note that the lower boundary of the integral inside the exponential can be absorbed in the normalization constant and it is thus arbitrary. The normalization constant  $C$  in Eq. (9) is such that

$$\int_0^{s_1} p(u) du = 1. \quad (10)$$

We will also make use of the cumulative probability function,

$$P(s) = \int_0^s p(u) du, \quad (11)$$

which gives the average fraction of time spent by the process below  $s$  during a homogeneous growing season, as a function of soil, climate and vegetation characteristics.

The frequency and durations of the excursions of the soil moisture process below and above a generic threshold  $s = \xi$  have been obtained before (Porporato et al. 2001, Rodriguez-Iturbe and Porporato 2004). The frequency of downcrossings is

$$\nu_{\xi}^{\downarrow} = \rho(\xi)p(\xi), \quad (12)$$

which at steady state equals the frequency of upcrossings. The mean time between a downcrossing and the subsequent upcrossing (i.e., the time spent by the process below the same threshold) is

$$\bar{T}_{\xi}^{\downarrow} = \frac{P(\xi)}{\rho(\xi)p(\xi)}, \quad (13)$$

from which the time spent by the process above the threshold follows as

$$\bar{T}_{\xi}^{\uparrow} = \frac{1 - P(\xi)}{\rho(\xi)p(\xi)}. \quad (14)$$

### 3.2.2 Continuous irrigation (modern micro-irrigation)

With the micro-irrigation typical of modern intensive agriculture, irrigation is turned on when soil moisture reaches the onset-of-stress level  $s^*$ . The rate of irrigation is such that soil moisture is maintained constant and equal to  $s^*$  until the next (effective) rainfall event takes place. Water application rate is therefore constant and equal to the evapotranspiration losses at  $s^*$ , i.e.  $I_m = ET(s^*) = nZ_r \rho(s^*)$  (the quantities referring to micro-irrigation will be indicated with a subscript  $m$  hereafter). An example of the typical time evolution of soil moisture for this irrigation is illustrated in Figure 3.1 (solid line). Since soil moisture stays for a finite time at the prescribed level  $s^*$ , the soil moisture pdf is of the mixed type, with an atom of probability,  $p_0$ , at  $s^*$ , and a continuous part,  $p_m(s)$ , for  $s^* < s \leq s_1$ .

Mathematically, the irrigation rate that exactly compensates the losses at a given  $s^*$  is equivalent to setting the overall loss function  $\rho(s)$  to zero for  $s \leq s^*$ . Thus, formally the problem becomes equivalent to a Takacs waiting-time process upper-bounded at  $s_1$  (Rodriguez-Iturbe and Porporato 2004), and the master equation is more conveniently solved by splitting it into a part for the continuous distribution  $p_m(s)$ ,

$$\begin{aligned} \frac{\partial}{\partial t} p_m(s, t) = & \frac{\partial}{\partial s} [\rho(s) p_m(s, t)] - \lambda' p_m(s, t) + \lambda' \int_0^s p_m(u, t) f(s-u, u) du \\ & + \lambda' p_0(t) f(s-s^*, s^*), \end{aligned} \quad (15)$$

and a part for the atom of probability in  $s^*$ ,

$$\frac{d}{dt} p_0(t) = -\lambda' p_0(t) + \rho(s^*) p_m(s^*, t). \quad (16)$$

The master equation (Eq. (15)), apart from a multiplication constant, admits the same solution as the master equation relative to rainfed agriculture (Eq. (6)). In fact, as also seen intuitively comparing solid and dashed lines to dotted one in Figure 3.1, the relative fraction of time spent by the process between any two soil moisture levels is not changed by the presence of the atom of probability in  $s^*$ . This fact implies that only the normalization constant is changed. As a result, the continuous part of the pdf becomes

$$p_m(s) = \frac{C_m}{\rho(s)} \exp\left(-\gamma s + \lambda' \int_s^s \frac{du}{\rho(u)}\right). \quad (17)$$

The normalization constant  $C_m$  can be obtained by imposing

$$1 - p_0 = \int_s^{s_1} p(u) du. \quad (18)$$

To obtain the atom probability, we first note that, at steady state, Eq. (16) becomes an equality between the rate of upcrossings and that of downcrossings at  $s^*$  (see Eq. (12)),

i.e.  $\lambda' p_0 = \rho(s^*) p_m(s^*)$ , which gives

$$p_0 = \frac{\rho(s^*) p_m(s^*)}{\lambda'} = \frac{C_m}{\lambda'} e^{-\gamma s^*}. \quad (19)$$

The fraction of time in which micro-irrigation is performed is  $p_0$ . Since during this time irrigation balances ET, the volume per unit area needed for micro-irrigation in a growing season of duration  $T_{seas}$  is

$$V_m = nZ_r \rho(s^*) p_0 T_{seas}. \quad (20)$$

The frequency and durations of irrigation may be derived from the crossing properties of the process, with threshold  $\xi = s^*$ . Hence, the mean frequency of irrigation is

$$\nu_m = \lambda' p_0, \quad (21)$$

and the average number of irrigation occurrence during the growing season is  $\lambda' p_0 T_{seas}$ .

Similarly to Eq. (13), the mean duration of each micro-irrigation treatment is

$$\bar{T}_{s^*,m}^\downarrow = \frac{P_m(s^*)}{\rho(s^*) p_m(s^*)} = \frac{p_0}{\lambda' p_0} = \lambda'^{-1}, \quad (22)$$

in agreement with the memoryless property of the Poisson process (the second equality follows from balance of upcrossings and downcrossings, and from Eq. (19)). The mean time during which no irrigation is applied is

$$\bar{T}_{s^*,m}^\uparrow = \frac{1 - P_m(s^*)}{\rho(s^*) p_m(s^*)} = \frac{1 - p_0}{\lambda' p_0}. \quad (23)$$

### 3.2.3 Concentrated applications (traditional irrigation)

Traditional irrigation typically foresees the concentrated delivery (instantaneous, at the daily time scale) of fixed water volumes when soil moisture reaches  $s^*$ . A numerically generated realization of the stochastic soil moisture process is shown in Figure 3.1 (dashed line). The applied amount of water is such that soil moisture is brought to  $s_1$  (or slightly higher in case of salinity control). While this form of irrigation

may be less efficient than micro-irrigation (see Sec. 3.3.2), it is an optimum scheme among the ones that use concentrated applications, and is equally or more effective than fixed-schedule irrigation. According to this scheme, the soil moisture process jumps to  $s_1$  with probability 1, whenever it reaches  $s^*$  during a dry-down. No atom of probability forms at the boundaries  $s^*$  and  $s_1$ , as at neither ends does soil moisture process spend a finite amount of time. At steady state, the loss of trajectories at  $s^*$  and their re-injection at  $s_1$  alter the balance of upcrossings and downcrossing, so that the probability current  $J$  is no longer zero but constant and equal to  $J^* = -\rho(s^*)p(s^*)$ , as follows from Eq. (8) evaluated at  $s = s^*$ . Accordingly, Eq. (8) becomes

$$J^* = -\rho(s)p_t(s) + \lambda' \int_{s^*}^s e^{-\gamma(s-u)} p_t(u) du, \quad (24)$$

where the quantities referring to traditional irrigation are indicated with the subscript  $t$ . Multiplying Eq. (24) by  $e^{\gamma s}$  and differentiating with respect to  $s$  yield a first-order linear differential equation, the solution of which reads

$$p_t(s) = -\frac{\exp\left(-\gamma(s-s^*) + \lambda' \int_{s^*}^s \frac{du}{\rho(u)}\right)}{\rho(s)} \left[ C_t + \gamma J^* \int_{s^*}^s \exp\left(\gamma(u-s^*) - \lambda' \int_{s^*}^u \frac{dy}{\rho(y)}\right) du \right]. \quad (25)$$

Combining Eqs. (24) and (25), it is easy to show that  $J^* = C_t$ , where the normalization constant  $C_t$  is such that

$$\int_{s^*}^{s_1} p_t(u) du = 1. \quad (26)$$

The frequency of concentrated irrigation treatments is the same as the frequency of downcrossings of  $s^*$ , i.e.  $-J^*$ , since arriving at  $s^*$  always triggers an irrigation event.

In other words, the probability of an effective rainfall events at  $s = s^*$  is  $\lambda' dt$  while that of irrigation is 1, so that the infinitesimal frequency of upcrossings due to rainfall does not contribute to the overall frequency. Hence, the frequency of traditional irrigation is

$$v_t = \rho(s^*) p_t(s^*). \quad (27)$$

In terms of irrigation volumes, each irrigation treatment supplies volume (per unit area)  $nZ_r(s_1 - s^*)$ . The total volume needed during a growing season is given by the volume of the single treatment ( $nZ_r(s_1 - s^*)$ ) multiplied by the number of applied treatments ( $v_t T_{seas}$ ), i.e.,

$$V_t = nZ_r(s_1 - s^*) \rho(s^*) p_t(s^*) T_{seas}. \quad (28)$$

The mean time between treatments is equal to the average time spent above  $s^*$ ,

$$\bar{T}_{s^*,t}^\uparrow = \frac{1}{\rho(s^*) p_t(s^*)}, \quad (29)$$

which follows from Eq. (14), considering that  $P_t(s^*) = 0$ . The mean duration of each (instantaneous) treatment is clearly zero.

### 3.3 Constant losses under well-watered conditions

The previous general solutions are now applied to a piecewise linear function with constant losses under well-watered conditions (Rodriguez-Iturbe et al. 1999). Empirical evidence, especially for monocultures, shows a roughly linear dependence of evapotranspiration on soil moisture from basically zero at wilting point (here  $s = 0$ , for simplicity) up to a maximum level  $E_{\max}$  at the point of incipient stomatal closure ( $s^*$ ), and then constant and equal to  $E_{\max}$  for higher soil moisture values (i.e., under well-watered conditions).  $E_{\max}$  depends on type of plant, soil and climate, and can be conveniently estimated using the Penman-Monteith equation (Rodriguez-Iturbe and Porporato 2004) or available experimental data. Introducing  $\eta = E_{\max} / (nZ_r)$ , the loss function is thus

$$\rho(s) = \begin{cases} \eta \frac{s}{s^*}, & 0 \leq s < s^* \\ \eta, & s^* \leq s \leq s_1. \end{cases} \quad (30)$$

#### 3.3.1 Soil moisture probability function at steady state

For rainfed agriculture and for the above described losses, with appropriate substitutions and integrations, Eq. (9) becomes

$$p(s) = \begin{cases} \frac{C}{\eta} \left( \frac{s}{s^*} \right)^{\frac{\lambda'}{\eta} s^* - 1} e^{-\gamma s}, & 0 \leq s < s^* \\ \frac{C}{\eta} e^{-\frac{\lambda'}{\eta} s^*} e^{-s \left( \gamma - \frac{\lambda'}{\eta} \right)}, & s^* \leq s \leq s_1. \end{cases} \quad (31)$$

The normalizing constant  $C$  is obtained by imposing Eq. (10), and reads

$$C = \left\{ \frac{e^{-\gamma s^*} - e^{-\gamma s_1 + \frac{\lambda'}{\eta} (s_1 - s^*)}}{\eta \gamma - \lambda'} + \frac{s^*}{\eta} (\gamma s^*)^{-\frac{\lambda'}{\eta} s^*} \left[ \Gamma \left( \frac{\lambda'}{\eta} s^* \right) - \Gamma \left( \frac{\lambda'}{\eta} s^*, \gamma s^* \right) \right] \right\}^{-1}, \quad (32)$$

where  $\Gamma \left( \frac{\lambda'}{\eta} s^*, \gamma s^* \right) = \int_{\gamma s^*}^{\infty} u^{\frac{\lambda'}{\eta} s^* - 1} e^{-u} du$  is the incomplete gamma function (Abramowitz

and Stegun 1965).

For micro-irrigation the pdf of  $s$  is formally equivalent to the case of rainfed agriculture (Eq. (31)) for  $s \geq s^*$ , i.e.,

$$p_m(s) = \frac{C_m}{\eta} e^{-\frac{\lambda'}{\eta} s^*} e^{-s \left( \gamma - \frac{\lambda'}{\eta} \right)}. \quad (33)$$

The atom of probability, obtained by solving Eq. (16), has the same form of the general solution (Eq. (19))

$$p_0 = \frac{C_m}{\lambda'} e^{-\gamma s^*}, \quad (34)$$

while the normalization constant is obtained by imposing Eq. (18)

$$C_m = \frac{\eta \gamma - \lambda'}{\eta \gamma \lambda'^{-1} e^{-\gamma s^*} - e^{-\gamma s_1} e^{\frac{\lambda'}{\eta} (s_1 - s^*)}}. \quad (35)$$

Conversely, for traditional irrigation the pdf of  $s$  reads

$$p_t(s) = C_t \left[ \frac{\lambda'}{\eta} e^{-\left(\gamma - \frac{\lambda'}{\eta}\right)(s-s^*)} - \gamma \right], \quad (36)$$

where

$$C_t = \left\{ \frac{\lambda'}{\eta\gamma - \lambda'} \left[ 1 - e^{-\left(\gamma - \frac{\lambda'}{\eta}\right)(s_1 - s^*)} \right] - \gamma(s_1 - s^*) \right\}^{-1}. \quad (37)$$

Some examples of steady state soil moisture pdf for both rainfed and irrigated agriculture are shown in Figure 3.2, under different rainfall conditions. The pdfs have drastically different shapes and modes. The mode lies below  $s^*$  for rainfed agriculture, at  $s^*$  for micro-irrigation, and at  $s_1$  for traditional irrigation. However, under higher total rainfall depths, the mode can shift above  $s^*$  for both rainfed conditions and micro-irrigation. Furthermore, as expected, irrigation results in higher probabilities at higher soil moisture levels. This fact is particularly evident in the case of traditional irrigation, because it provides larger irrigation volumes (see Sec. 3.3.2).

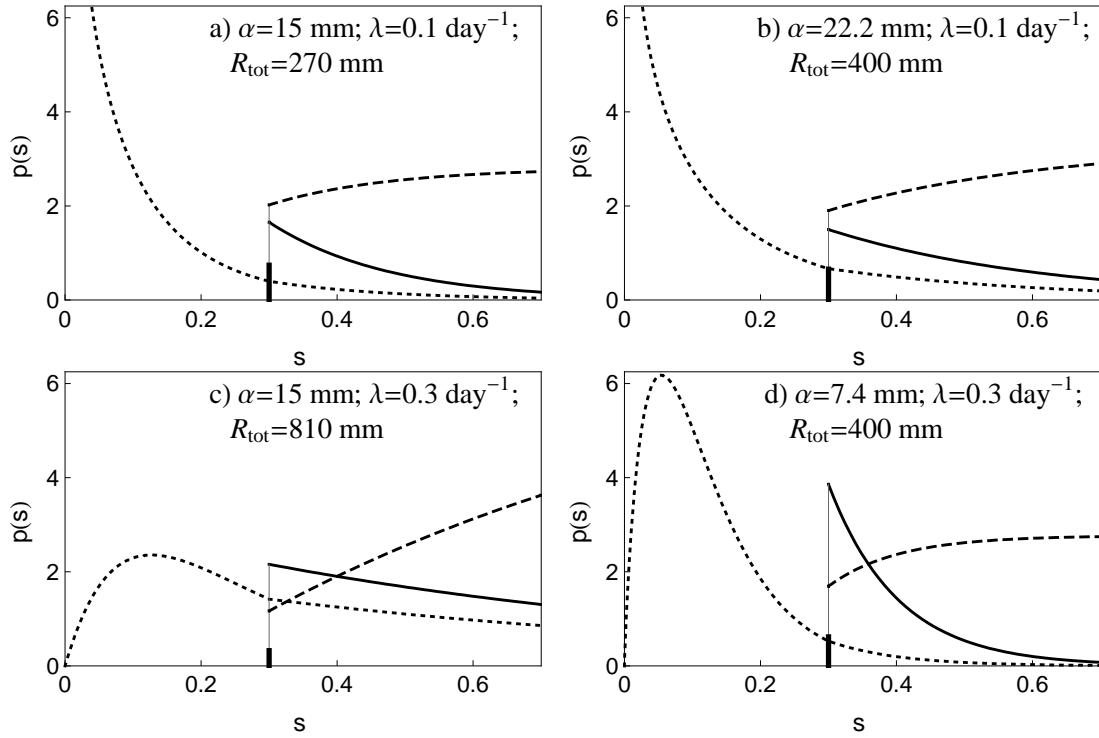


**Figure 3.2:** Examples of steady state probability density functions of soil moisture under different rainfall amounts and patterns, relative to the two irrigation schemes (micro-irrigation, solid lines; traditional irrigation, dashed lines); the case of no irrigation is reported for reference (dotted lines). Left: constant mean event depth ( $\alpha = 15$  mm, with increasing  $\lambda$  and  $R_{tot}$  as indicated). Right: constant total growing season precipitation ( $R_{tot} = 400$  mm, with different combinations of  $\lambda$  and  $\alpha$ , as indicated). All the other parameters are as in Figure 3.1.

The impact of rainfall regime is assessed by analyzing two cases: i) increasing the total rainfall per growing season  $\langle R \rangle T_{seas} = \alpha \lambda T_{seas}$  by changing storm frequency,  $\lambda$ , while keeping  $\alpha$  fixed (Figure 3.2a, c)); and ii) keeping fixed total amount of rainfall during the growing season, while altering  $\alpha$  and  $\lambda$  (Figure 3.2b, d)). In the first case, an increase in storm frequency,  $\lambda$ , with fixed mean event depth (Figure 3.2, left column) shifts the mode of the probability distribution toward higher  $s$ , a clear consequence of

the increased total seasonal precipitation. The shape of the distribution is also modified. For rainfed and micro-irrigated agriculture, an increase in  $\lambda$  and the consequent increase in total precipitation result in a more uniform distribution of  $s$ , while for traditional irrigation the more frequent storms require fewer irrigation treatments and increase the time spent at  $s$  levels near  $s_1$ .

The case of constant total precipitation (Figure 3.2, right column) clarifies the impact of rainfall timing and amounts. Infrequent and intense events tend to produce low soil moisture levels because of increase losses by percolation and deep infiltration (Figure 3.2b)); similarly, very frequent and light events favor canopy interception with a consequent reduction of total effective rainfall (Figure 3.2d)). For micro-irrigation (solid lines in Figure 3.2), smaller but frequent events contribute to maintain soil moisture not far above  $s^*$  (Figure 3.2d)), while infrequent events delivering higher amounts of water result in a more uniform probability distribution between  $s^*$  and  $s_1$  (Figure 3.2b)). Conversely, for traditional irrigation frequent but small events counteract the impact of irrigation water applications, thus increasing the time the system spends at intermediate soil moisture levels (Figure 3.2d), dashed lines).

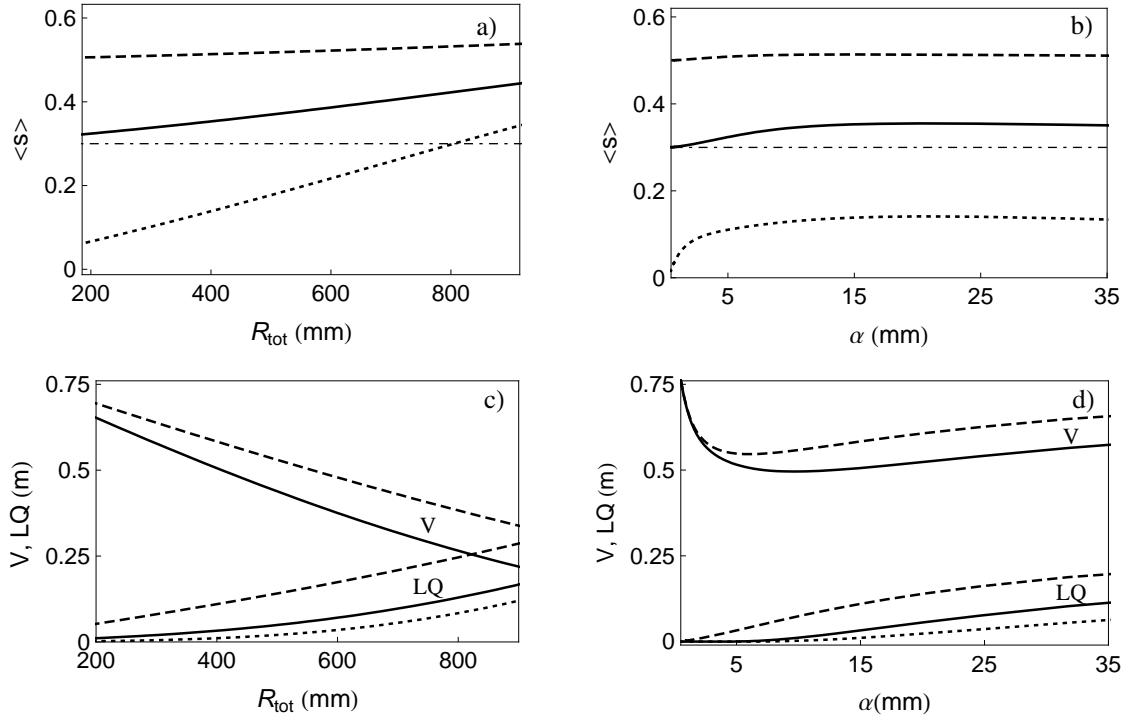


**Figure 3.3:** Average soil moisture (a, b) and long term soil water balance (c, d) under different rainfall amounts and timing, for (left) increasing total rainfall  $R_{tot}$  and fixed mean event depth ( $\alpha = 15$  mm), and (right) fixed total growing season rainfall depth ( $R_{tot} = 400$  mm) and variable  $\lambda$  and  $\alpha$ , for rainfed agriculture (dotted lines), micro-irrigation (solid lines) and traditional irrigation (dashed lines). In a) and b) dash-dotted lines represent  $s^*$ . In c) and d) irrigation volumes ( $V$ ) are compared to deep percolation and runoff losses ( $LQ$ );  $LQ$  for rainfed agriculture (dotted lines) is plotted for reference. All the components of the water balance are expressed as volumes per unit area, i.e. depths. All the other parameters are as in Figure 3.1.

### 3.3.2 Mean soil water balance and required irrigation volumes

Mean soil moisture can be easily computed from the analytical soil moisture pdf's. As expected, micro-irrigation maintains the mean soil moisture closer to  $s^*$  than any other treatment, but always above it (Figure 3.3a, b)), thus guaranteeing minimum

water use while avoiding plant water stress. Traditional irrigation tends to maintain a higher mean soil moisture, while for rainfed agriculture the mean can be below stress for low total rainfalls.  $\langle s \rangle$  is not significantly impacted by mean event depth, except at very low values of  $\alpha$ , when effective rainfall is minimal due to interception and  $\langle s \rangle$  goes to zero for rainfed agriculture and to  $s^*$  for micro-irrigation (Figure 3.3b)).

The mean soil water balance is of great interest too, given its links to volumes of water needed for irrigation purposes, and percolation losses, which are related to leaching of soluble chemicals, soil salinization and groundwater recharge. The different components of the water balance are the long-term averages of the respective components of the soil moisture balance at the daily time scale (Eq. (5)), i.e.

$$\langle R' \rangle + \langle I \rangle = \langle ET \rangle + \langle LQ \rangle . \quad (38)$$

The inputs to the system are rainfall (minus interception),  $\langle R' \rangle = \alpha' \lambda'$ , and irrigation,  $\langle I \rangle$ , if any. Total input is partitioned into evapotranspiration,  $\langle ET \rangle = \int_0^{s_1} \rho(u)p(u)du$ , and runoff and deep infiltration losses,  $\langle LQ \rangle$ . Considering the soil water balance for a growing season of duration  $T_{seas}$ , the total rainfall is  $R_{tot} = \alpha \lambda T_{seas}$  resulting in a total effective rainfall input  $R'_{tot} = \alpha' \lambda' T_{seas}$ , while irrigation volume is  $\langle I \rangle T_{seas}$ , i.e.  $V_m$  or  $V_t$  (as obtained through Eqs. (20) and (28) respectively), and water losses  $LQ = \langle LQ \rangle T_{seas}$ . Note that volumes of water are expressed in terms of volumes per unit area, i.e. depths.

Figure 3.3c) and d) compare irrigation volumes to runoff and deep percolation losses under different total rainfall amounts (but fixed mean event rate  $\alpha$ ; Figure 3.3c)) and rainfall timing (fixed total rainfall amount, with increasing  $\alpha$  and decreasing  $\lambda$ ; Figure 3.3d)). In the first case, as expected, the higher the total rainfall amounts over the growing season, the lower the water volumes needed for irrigation purposes but the higher the amount of water lost to runoff and deep infiltration (Figure 3.3c)), and interception (not shown). In contrast, in the second case (constant total growing season precipitation), irrigation water requirements slightly increase with increasing mean event depth, with the exception of very small rainfall depths. In fact, for small event depths, interception significantly decreases effective rainfall, thus enhancing water demand and reducing runoff and deep infiltration. For intermediate to high event depths, for higher  $\alpha$  more water is lost to runoff or deep percolation with respect to the case of frequent and small events (Figure 3.3d)) for both rainfed and irrigated soils.

As also apparent from Figure 3.3c) and d), under realistic parameters for soil features and evaporative demand,  $V_i - V_m \geq 0$ , i.e. the micro-irrigation scheme requires smaller volumes of water than traditional irrigation under all climatic conditions. It should be noted that with the adopted constant evapotranspiration function above  $s^*$  (Eq. (30)), the same amount of water is transpired by crops subjected to the two irrigation schemes, in spite of the expected disparity in average soil moisture (Figure 3.3a) and b)). Thus, the difference between the mean soil water balances for the two

irrigation schemes is totally compensated by increased deep percolation and runoff for traditional irrigation, i.e.

$$V_t - V_m = \langle LQ_t \rangle - \langle LQ_m \rangle. \quad (39)$$

Eq. (39) explains why the differences in water requirements between irrigation schemes are slightly more marked towards higher total rainfall depths (Figure 3.3c) and infrequent but deep events (i.e., for high values of  $\alpha$  in Figure 3.3d). It should be noted that, as expected, even such a fine-tuned irrigation as micro-irrigation results in higher water losses than rainfed agriculture (Figure 3.3c) and d), compare solid lines to dotted ones). In fact, at higher average soil moistures it is more likely that a rainfall event exceeds the soil storage capacity  $nZ_r(s_1 - s)$ , which explains why water lost under traditional irrigation is higher than the one for micro-irrigation.

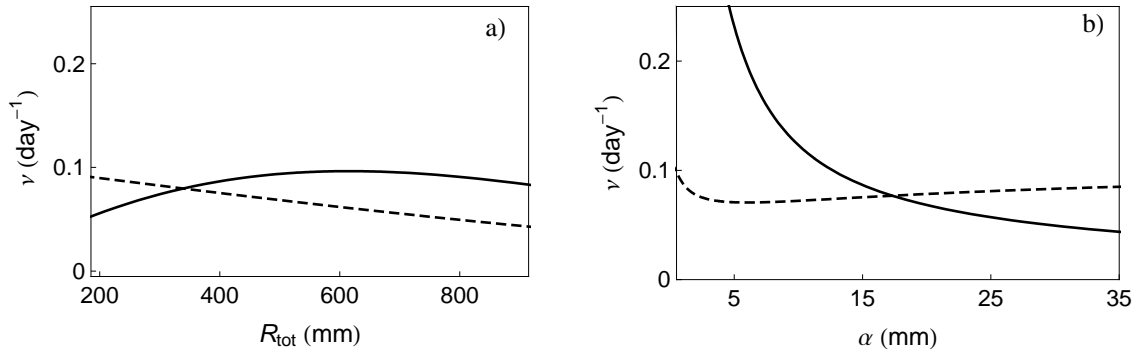


**Figure 3.4:** Irrigation frequency requirements under different rainfall amounts and timing, for a) increasing total rainfall depth but fixed mean event depth ( $\alpha = 15$  mm), and b) fixed total growing season rainfall depth ( $R_{\text{tot}} = 400$  mm) for micro-irrigation (solid lines) and traditional irrigation (dashed lines). All the other parameters are as in Figure 3.1.

### 3.3.3 Frequency of irrigation

Frequency and duration of each irrigation treatment may also be relevant for water infrastructure planning and irrigation management. For traditional irrigation, the frequency of irrigation completely defines the process, while for micro-irrigation, both frequency and duration of each treatment play a role: in fact, micro-irrigation may last for several days under dry spells, hence the frequency of treatment initiation may decline, while duration (and applied volumes) are high. (The mean duration of each micro-irrigation treatment is completely determined by rainfall frequency (see Eq. (22)).

When total rainfall is increased while  $\alpha$  is kept constant (Figure 3.4a)), the frequency of irrigation decreases monotonically for traditional irrigation, not only because the amount of total precipitation during the growing season is increased, but also because more frequent rainfall events result in soil moisture reaching the threshold  $s^*$  less often. For micro-irrigation, the dependence of  $\nu_m$  on rainfall amounts and frequency is more complex. Maximum irrigation frequency is observed for intermediate  $R_{tot}$  (such maximum occurs at higher values of  $R_{tot}$  for lower mean event depths; not shown). In contrast, low  $R_{tot}$  (i.e., low  $\lambda$ ) require longer periods of continuous irrigation, which translates in lower irrigation frequency, while at the other extreme, frequent rainfall events (and higher total rainfall amounts) result in an overall higher soil moisture, and less frequent irrigation applications.

When total growing season rainfall is kept constant while average rainfall depth increases (Figure 3.4b)), frequency of irrigation monotonically decreases with  $\alpha$  for micro-irrigation, while it slightly increases for traditional irrigation. For micro-irrigation, frequent but small rain events only produce small departures above  $s^*$  which are quickly nullified by evapotranspiration losses, and this triggers frequent (but short) irrigation periods. In contrast, the rainfall regime has a less marked and opposite impact on traditional irrigation frequency, which decreases towards low  $\alpha$ , because frequent but small rainfall events help delay the need of irrigation.

### **3.3.4 Comparison of irrigation schemes for different crops and climatic conditions**

Thanks to its analytical tractability, the proposed model clearly shows the dependence of irrigation requirements on the main crop and soil features, as well as hydroclimatic parameters. As such, our model represents a tool to identify crop ( $E_{\max}$ ,  $s^*$ ,  $Z_r$ ) and soil ( $s_1$ ,  $s^*$ ,  $n$  and  $Z_r$ ) features that result in the most sustainable and profitable irrigation scheme under given climatic conditions.

A sensitivity analysis (not shown) suggests that, for realistic values of the parameters, maximum transpiration rate,  $E_{\max}$ , and rainfall statistics,  $\alpha$  and  $\lambda$ , are the main drivers of irrigation needs, followed by the interception parameters, while the incipient stress point,  $s^*$ , and soil features play a secondary role. As expected, the

higher the rainfall interception and plant requirements in terms of transpiration rates and stress avoidance, the larger the volumes required for irrigation. An increase in frequency of traditional irrigation  $\nu_t$  is observed for increasing plant interception and transpiration demands, while the dependence of  $\nu_m$  on such parameters is more complex, because higher irrigation requirements may result in either more frequent or less frequent (but longer) micro-irrigation treatments depending on the rainfall pattern (Sec. 3.3.3). Overall the impact of interception parameters on frequency of irrigation is less marked than on volumes of irrigation. Moreover, traditional irrigation is more sensitive to plant water demands than micro-irrigation. The sensitivity of irrigation needs to plant water demand is also impacted by rainfall amount and timing, but in opposite ways for traditional and micro-irrigation: the higher the rainfall amount or storm frequency, the stronger the dependence of irrigation volumes and frequency on  $E_{\max}$  for micro-irrigation, the weaker for traditional irrigation.

The response of irrigation needs to soil properties is mainly driven by the amount of water potentially lost to deep percolation and runoff. Consequently, soil types with higher field capacity (and hence  $s_1$ ) require less frequent irrigation treatments with smaller volumes. For similar reasons, deeper active soils (i.e., higher  $Z_r$ ) tend to have smaller irrigation needs, particularly for traditional irrigation. It is also interesting to analyze the combined effect of soil thresholds: for micro-irrigation, water volumes and application frequency required for plant stress avoidance are independent

of soil features, as long as  $s_1 - s^*$  is constant. This fact has significant implications concerning possible soil amendments for better water use. In fact, since both soil thresholds tend to increase with diminishing soil particle size, for micro-irrigation an addition of sand or loam may not alter the irrigation requirements as significantly as it might be expected. This is clearly not the case for rainfed agriculture or traditional irrigation, for which higher  $s^*$  and  $s_1$  result in lower average soil moisture levels and higher irrigation demands.

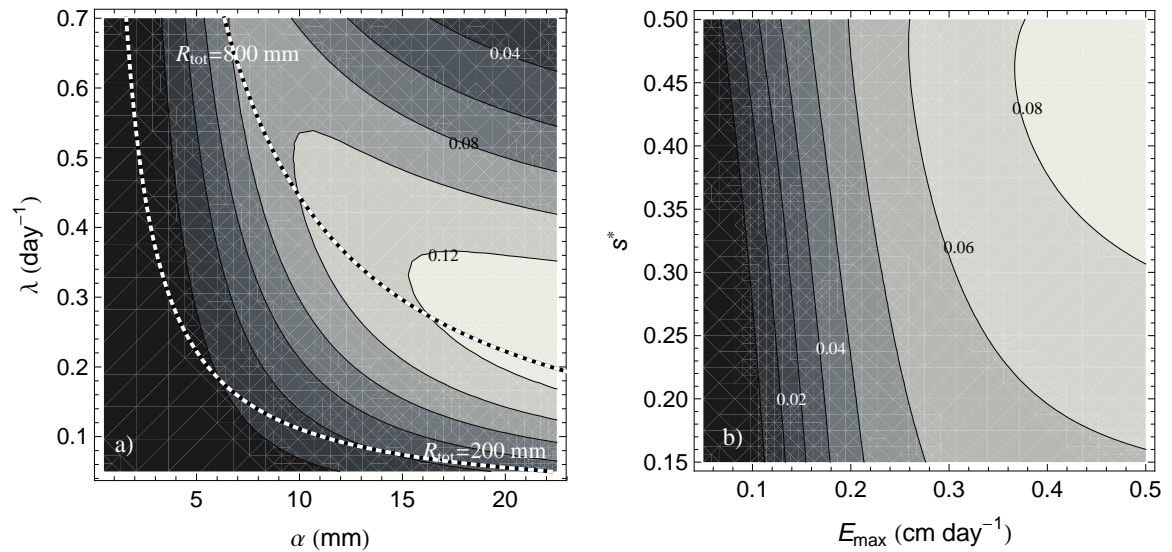


**Figure 3.5:** Difference in required irrigation volumes between traditional and micro-irrigation,  $V_i - V_m$  (units are meters of applied water per growing season), as a function of a) rainfall amount and pattern (here represented by mean event depth,  $\alpha$ , and frequency of events,  $\lambda$ ), and b) crop water requirements (here represented by maximum transpiration rate,  $E_{max}$ , and point of incipient stomatal closure,  $s^*$ ). Dashed lines in a) represent combinations of  $\alpha$  and  $\lambda$  leading to the same total precipitation over the growing season,  $R_{tot}$ , as indicated. All the other parameters are as in Figure 3.1.

Building upon these results, we now compare the water requirements of the two irrigation schemes, for various hydroclimatic conditions and plant features. As discussed in Section 3.3.2, micro-irrigation requires smaller water volumes than traditional irrigation, as less water is lost to deep infiltration. Nevertheless, the extent of water saved by applying micro-irrigation rather than the more traditional scheme (i.e.,  $V_t - V_m$ ) depends on rainfall parameters and plant water requirements, as explored in Figure 3.5 (left and right panels respectively). Regarding rainfall amount and timing, the amount of water saved by choosing micro-irrigation is highest for medium to high  $R_{tot}$ , in particular when such amount is delivered through infrequent but rather deep events. In fact, such rainfall patterns enhance water lost to runoff and deep infiltration in particular in the case of traditional-irrigation, thus also maximizing the difference  $V_t - V_m$  (Eq. (39)). The difference in irrigation water volumes is higher for crops (and environmental conditions) with higher water demands, both in terms of maximum transpiration rate and point of incipient stomatal closure (Figure 3.5b)). However,  $V_t - V_m$  is more sensitive to  $E_{max}$  than to  $s^*$ : this fact implies that any environmental condition that enhances transpiration rate may render micro-irrigation even more advantageous in terms of water requirements.

### **3.4 Discussion and conclusions**

While climatic conditions cannot be controlled, agricultural management may take pro-active steps to adapt soil features and crop species to the local rainfall and climatic regimes, to achieve sustainability and profitability.

When irrigation is constrained by limited water availability, total water needed to avoid plant water stress (i.e., to maximize yield) over the growing season may be the main element to prefer one irrigation scheme to the other. Under such conditions, micro-irrigation (possibly associated to deficit irrigation, as discussed in Chapter 4) is the most convenient irrigation scheme. Furthermore, because of the adopted constant evapotranspiration function above  $s^*$  (Eq. (30)), the same amount of water is transpired for stress avoidance irrigation, regardless of the selected scheme. Hence, being crop productivity related to seasonal transpiration (e.g., Payero et al. 2006, Geerts and Raes 2009), at a first approximation the same crop yield will be achieved. These facts render micro-irrigation always preferable to minimize water requirements, as well as to maximize water use efficiency (water transpired per unit applied water) and water productivity (crop yield per unit applied water). A further potential advantage of micro-irrigation lies in its ability to minimize lost water, which in turn limits nutrient leaching and groundwater pollution. Nevertheless, the limitation of deep percolation might be also a potential drawback when soil salinization is an issue. Under such circumstances, traditional-irrigation may be preferable as it at least partially limits soil salinization due

to increased deep percolation, even though the exact amount of required soil flushing is difficult to determine and the higher supplied water volumes may be counterproductive if water itself is a source of salts.

Despite these advantages in terms of sustainability, such a fine-tuned scheme as micro-irrigation may be difficult to apply in practice (English et al. 2002, Jones 2004), thus making traditional-irrigation (or some mixed scheme) preferable. Moreover, depending on the cost of irrigation water in the region under scrutiny, stress-avoidance micro-irrigation may not be the most profitable choice, as its direct costs of installations are generally around double those for surface irrigation (Brady and Weil 2002, p. 264). Since, as a first approximation, crop yield is not expected to be impacted by the chosen irrigation scheme, the profitability of micro-irrigation over traditional-irrigation entirely depends on the balance between higher installation costs and lower water expenses. In face of the predicted increase in water demands and decrease in readily available water supplies (Jury and Vaux 2007), micro-irrigation may become more profitable in the near future, even in regions where less refined irrigation schemes are currently advantageous under the economic point of view.

## **4 From rainfed agriculture to stress-avoidance irrigation: optimizing crop yield and net profit under intra- and inter-annual stochastic hydrologic variability**

This chapter is based on the manuscript Vico G. and A. Porporato, From rainfed agriculture to stress-avoidance irrigation: optimizing crop yield and net profit under intra- and inter-annual stochastic hydrologic variability, in preparation.

### ***4.1 Introduction***

Population growth and quest for food security and biofuels, among other things, have increased global water demand, while water quality degradation, ecosystem and climatic alterations impose more stringent limitations on water supply, in particular in certain areas of the world (Jury and Vaux 2007). Agriculture represents the most important freshwater user, absorbing around 80% of withdrawn water (FAO 2002), and irrigated agriculture is responsible for 40% of total food production (Feres and Soriano 2007). The role of irrigation, which has become more and more important in the past decades, is projected to further increase in the near future (FAO 2002).

It is becoming increasingly apparent that part of agricultural land is currently being managed unsustainably, by inappropriate tillage and crop rotation practices (resulting in soil compaction, top soil loss and a general decrease in fertility), or supply of water, fertilizers and pesticides (resulting in soil salinization, excessive water withdrawal,

groundwater pollution) (Schoups et al. 2005, Payero et al. 2006, Forkutsa et al. 2009). As such, choices for irrigation strategies need to include considerations relative to its sustainability, profitability and crop yield. Among other possible improvements, changes in irrigation scheduling and water delivery technique may significantly increase the overall efficiency of irrigation and water productivity (i.e., crop yield per unit applied water), both by reducing losses through runoff and deep percolation, and by increasing application uniformity. As for irrigation scheduling one of the main improvements is switching from time-fixed irrigation to demand-based irrigation, either by estimates of crop available water through potential evapotranspiration or soil moisture monitoring (Jones 2004). Also, when water is scarce or expensive, a deficit irrigation (i.e., the application smaller amounts of water than those required to compensate transpiration) can increase water productivity (Jury and Vaux 2007) and can even improve the partitioning of carbohydrate to reproductive structure such as fruit, control excessive growth and mutual shading (Chalmers et al. 1981), and increase the quality of some fruits (particularly grapes; Fereres and Soriano (2007) and references therein).

The choice of 'optimal' irrigation management is complicated by uncertainties in crop yield, fluctuations in crop prices and costs, and rainfall unpredictability. A number of factors contribute to the uncertainty inherent in crop yield as a function of applied water, among which the timing of rainfall relative to growth stages, crop physiological

response to water availability, soil features, irrigation efficiency and amount of water lost to runoff and deep infiltration (English 1981). To assess the profitability of an irrigation practice, crop prices and fixed and variable costs need to be accounted for, along with their variability and its impact on 'optimal' irrigation management. For example, elevated costs of irrigation infrastructure or water supply may currently prevent the expansions of irrigated areas, but irrigation might become economically feasible in face of trend of increasing crop prices or changes in the regulatory and policy incentive scenarios. However, rainfall intermittency, and its random timing and amounts, both at the daily and growing season time scales, by far represents the most important source of uncertainty in soil moisture variability and hence irrigation feasibility and crop productivity. Interannual rainfall variability is particularly relevant in humid regions, where rainfed agriculture may be profitably performed in wetter years, while drier years may require significant water supplies through irrigation; in contrast, agriculture in arid areas is completely dependent on irrigation, hence water requirements exhibit a lower variability (Wisser et al. 2008). The daily and interannual rainfall variability requires a probabilistic approach to obtain a tool for yield predictions (and economic risk quantifications), and water allocation. Also, the forecast change in rainfall timing, with increase in frequency of dry spells and temperatures (and hence potential evapotranspiration), requires a modelistic approach to the problem for long-term water resource management and infrastructure choices.

In Section 4.2, we offer a statistical description of soil moisture at steady state conditions for a generalized irrigation scheme; the same framework may be extended to the case of rainfed agriculture. Processes are resolved at the daily time scale, thus allowing the inclusion of random timing and amount of rainfall, which represent the most important source of uncertainty in soil moisture variability. In Section 4.3, on the basis of frequently observed relationship between seasonal transpiration and crop yield, we obtain average crop yield and show how it is affected by irrigation practices, total precipitation and its average timing; the implications of the irrigation scheme choice are discussed under the economic viewpoint. Finally, to provide an effective tool for long-term irrigation planning, in Section 4.4 we explore the impact of rainfall interannual variability on crop yield, and the economic risks associated to such variability.

## **4.2 Model formulation**

### **4.2.1 Soil water balance**

Under the assumptions of negligible lateral soil moisture fluxes, the water balance averaged over the active soil depth, where most of the roots are located,  $Z_r$ , reads

$$nZ_r \frac{ds(t)}{dt} = R(t) + I(s,t) - ET(s) - LQ(s,t). \quad (40)$$

$n$  is the soil porosity,  $s$  is the plant accessible relative soil moisture,  $R(t)$  and  $I(s,t)$  are the rainfall and irrigation inputs, while  $ET(s)$  and  $LQ(s,t)$  represents the main soil

water losses (evapotranspiration and the combined effects of deep infiltration and runoff losses respectively).

Rainfall  $R(t)$  is modeled as instantaneous events occurring according to a marked Poisson process of rate (mean frequency of rainfall events)  $\lambda$ , and with exponentially distributed depths with mean  $\alpha$  (Rodriguez-Iturbe et al. 1999, Rodriguez-Iturbe and Porporato 2004).  $R(t)$  may be purged of canopy interception, which may reduce both the frequency of effective rainfall and its depth (Rodriguez-Iturbe et al. 1999, Daly et al. 2008). For the sake of simplicity, in the following, we neglect canopy interception. Mean rainfall depth will be normalized as  $1/\gamma = \alpha/nZ_r$ .

We assume a ‘generalized traditional irrigation’ scheme, consisting in concentrated applications of water when soil moisture reaches a given ‘intervention’ level  $\tilde{s}$ . At each treatment, a fixed amount of water is applied thus bringing soil moisture back to a prescribed level  $\hat{s}$ . Such irrigation scheme is more general than the traditional irrigation discussed in Chapter 3, since it represents through a common framework ambient conditions (i.e., the so-called rainfed agriculture), traditional irrigation (i.e., a concentrated application of water to bring soil moisture back to  $\hat{s}$  whenever  $\tilde{s}$  is reached) and micro-irrigation (i.e., a continuous supply of water which maintains soil moisture at  $\tilde{s}$ ). The case of rainfed agriculture is retrieved when the intervention point  $\tilde{s}$  tends to 0, i.e. no irrigation is ever performed regardless of soil water status. The micro-irrigation scheme is retrieved when  $\hat{s} \rightarrow \tilde{s}$ . Furthermore,

through a proper definition of  $\tilde{s}$  and  $\hat{s}$  with respect to vegetation and soil parameters such as incipient stomatal closure  $s^*$  and soil field capacity (above which soil deep percolation becomes relevant), this generalized scheme allows to assess the water requirements for both deficit and stress avoidance irrigation, as well as soil flushing in case of soil salinization problems.

Daily evapotranspiration per unit ground area  $ET(s)$  is assumed to vary in time only through soil moisture, thus neglecting the effect of the day-to-day variability in transpiration rate, caused by either plant growth or variable environmental conditions (e.g., air temperature and humidity, solar irradiance). While the latter has a secondary effect when compared to the impact of rainfall-induced soil moisture variability, the former may be relevant, in particular when annual crops are considered. Nevertheless, to keep the analytical tractability, the dependence of transpiration rate on soil moisture,  $ET(s)$ , will be assumed constant in time, and interpreted as an average over the growing season. While for the general results reported below the specific form of  $ET(s)$  is not relevant, in the following quantitative applications a piecewise linear function with constant losses under well watered conditions will be assumed (Rodriguez-Iturbe et al. 1999):

$$\rho(s) = \begin{cases} \eta \frac{s}{s^*} & \text{if } 0 \leq s < s^* \\ \eta & \text{if } s^* \leq s < s_1. \end{cases} \quad (41)$$

$\eta = E_{\max} / (nZ_r)$  is the normalized loss rate under well watered conditions (averaged over the growing season), and  $s^*$  is the point of incipient stomatal closure, below which experimental evidence (e.g., Morison and Gifford 1984, Kalapos et al. 1996) suggest a linear decrease in plant transpiration down to basically zero at wilting point (here  $s = 0$  for simplicity). Both  $E_{\max}$  and  $s^*$  depend on plant and soil features.

Finally, deep infiltration and runoff losses  $LQ(s, t)$  are treated here in a simplified manner, by assuming they take place instantaneously (at the daily time scale) whenever soil moisture reaches a threshold  $s_1$ , typically around or slightly above soil field capacity (Milly 2001, Porporato et al. 2004). Because of this simplified treatment of  $LQ(s, t)$ , the soil moisture process is bound at  $s_1$ .

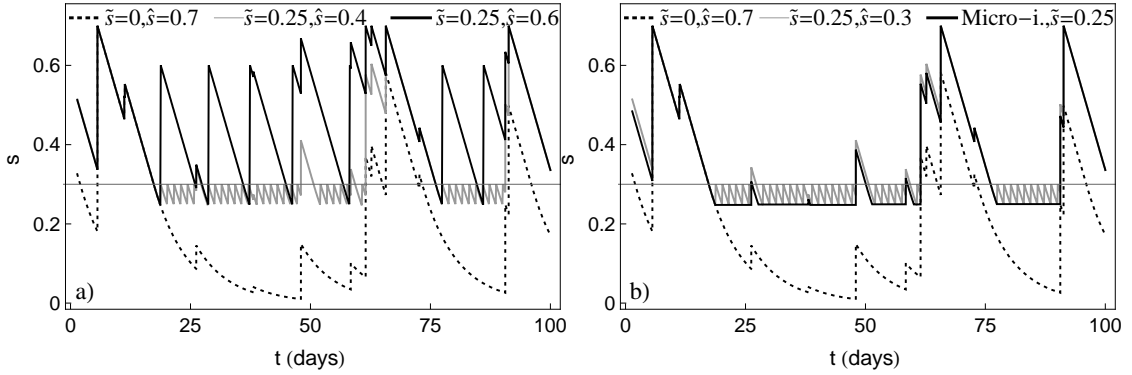


**Figure 4.1:** Example of soil moisture time series for two choices of the parameters  $\tilde{s}$  and  $\hat{s}$ ; soil moisture temporal evolution for rainfed agriculture is reported for reference (dotted line), as well as  $s^* = 0.3$  (thin horizontal lines). Soil is sandy loam with  $n=0.43$ ,  $Z_r = 25$  cm (Rodriguez-Iturbe and Porporato 2004);  $s_1 = 0.7$ . Average precipitation depth is  $\alpha = 15$  mm and rainfall frequency  $\lambda = 0.15$  day<sup>-1</sup>. Evapotranspiration rate is  $E_{\max} = 0.45$  cm day<sup>-1</sup>.

A few examples of soil moisture time series for different choices of the irrigation parameters  $\tilde{s}$  and  $\hat{s}$  are presented in Figure 4.1. As expected, under ambient conditions (dotted lines), soil moisture levels oscillates both above and below  $s^*$ , depending on rainfall occurrence. An irrigation treatment limits such variability to soil moisture levels above  $\tilde{s}$ . The choice of  $\hat{s}$  strongly impacts the most probable values assumed by soil moisture over the course of time: the nearer  $\hat{s}$  is to  $\tilde{s}$ , the more the process oscillates in a small range of soil moisture levels, with infrequent excursions above  $\hat{s}$  driven by rainfall occurrence (gray lines).

## 4.2.2 Generalized traditional irrigation

The soil water balance described by the nonlinear stochastic differential equation (40) has been extensively analyzed elsewhere, both in absence of irrigation (Rodriguez-Iturbe and Porporato 2004 and references therein) and under simplified irrigation schemes such as micro-irrigation and traditional irrigation (Chapter 3). We now extend the previously obtained results to the case of the generalized traditional irrigation described above, and offer exact solutions of the steady state soil moisture probability density function (pdf). Its evolution for  $\tilde{s} \leq s \leq s_1$  is described by the master or Chapman-Kolmogorov equation

$$\frac{\partial}{\partial t} p(s, t) = \frac{\partial}{\partial s} [\rho(s)p(s, t)] - \lambda p(s, t) + \lambda \int_{\tilde{s}}^s p(u, t) f(s-u, u) du, \quad (42)$$

where  $f(y, s) = \gamma e^{-\gamma y} + \delta(y - s_1 + s) e^{-\gamma(s_1 - s)}$  is the pdf of the soil moisture jumps due to the difference between the instantaneous rainfall and the runoff and percolation events (Porporato et al. 2004, Rodriguez-Iturbe and Porporato 2004). Eq. (42) may be more conveniently written with the formalism of probability currents (Chapter 3; Daly and Porporato 2006a) as

$$\frac{\partial}{\partial t} p(s, t) = -\frac{\partial}{\partial s} J(s, t), \quad (43)$$

where the probability current  $J(s, t)$  is

$$J(s,t) = -\rho(s)p(s,t) + \lambda \int_{\tilde{s}}^s e^{-\gamma(s-u)} p(u,t) du. \quad (44)$$

A general solution of Eq. (42) or Eqs. (43) and (44) presents serious mathematical difficulties; hence we focus here on stochastic steady state conditions, i.e.  $\partial p(s,t)/\partial t = 0$ . Under such assumption, the loss of trajectories at  $\tilde{s}$  and their re-injection at  $\hat{s} \leq s_1$  alter the balance of upcrossings and downcrossings, so that the probability current  $J(s)$  is equal to  $\tilde{J} = -\rho(\tilde{s})p(\tilde{s})$  if  $\tilde{s} \leq s \leq \hat{s}$ , and zero for  $\hat{s} < s \leq s_1$ . Thus, in general

$$J(s) = \theta(\hat{s} - s)\tilde{J} = -\theta(\hat{s} - s)\rho(\tilde{s})p(\tilde{s}), \quad (45)$$

where  $\theta(\cdot)$  is the Heaviside function. Eq. (45) reduces to  $J(s) = 0$  for  $\tilde{s} \rightarrow 0$  (i.e., rainfed agriculture) and to  $J(s) = \tilde{J}$  for  $\hat{s} \rightarrow s_1$  (i.e., traditional irrigation bringing soil moisture to  $s_1$ ), in agreement to the results presented in Chapter 3.

Substituting Eq. (45) into Eq. (44), multiplying by  $e^{\gamma s}$  and differentiating with respect to  $s$ , a first order ordinary linear differential equation is obtained. Its solution is

$$p(s) = \frac{e^{-\int_{\tilde{s}}^s \left(\gamma - \frac{\lambda}{\rho(u)}\right) du}}{\rho(s)} \left\{ C + \tilde{J} \int_{\tilde{s}}^s [\gamma \mathcal{G}(\hat{s} - u) - \delta(\hat{s} - u)] e^{\int_{\tilde{s}}^u \left(\gamma - \frac{\lambda}{\rho(y)}\right) dy} du \right\}, \quad (46)$$

where  $\delta(\cdot)$  is the Dirac delta function and the normalizing constant  $C$  is such that

$$\int_{\tilde{s}}^1 p(u) du = 1. \quad (47)$$

The choice of the lower limit of integration in Eq. (46) is arbitrary and does not alter the final result. However, for simplicity of notation, it is convenient to set such limit at  $\tilde{s}$ , which results in  $\tilde{J} = C$ , as it is easy to show combining Eqs. (45) and (46).

Assuming a piecewise linear loss function for  $ET(s)$  (Eq. (41)) and deficit irrigation ( $\tilde{s} < s^*$ ), with appropriate substitutions and integrations, Eq. (46) becomes

$$p(s) = \begin{cases} \frac{C}{\eta} \frac{s^*}{s} e^{\gamma(s-\tilde{s})} \left(\frac{s}{\tilde{s}}\right)^{\frac{\lambda s^*}{\eta}} \left\{ 1 + e^{\gamma \tilde{s}} \tilde{s}^{\frac{\lambda s^*}{\eta}} [h_1(s) - h_1(\tilde{s})] \right\} & \text{if } \tilde{s} \leq s < s^* \\ \frac{C}{\eta} e^{-\gamma(s-\tilde{s}) + \frac{\lambda}{\eta}(s-s^*)} \left(\frac{s^*}{\tilde{s}}\right)^{\frac{\lambda s^*}{\eta}} \left\{ 1 + e^{\gamma \tilde{s}} \tilde{s}^{\frac{\lambda s^*}{\eta}} [h_1(s^*) - h_1(\tilde{s})] + e^{\gamma(s^*-\tilde{s})} e^{-\left(\gamma - \frac{\lambda}{\eta}\right)s^*} \left(\frac{\tilde{s}}{s^*}\right)^{\frac{\lambda s^*}{\eta}} [h_2(s) - h_2(s^*)] \right\} & \text{if } s^* \leq s \leq s_1 \end{cases} \quad (48)$$

where

$$h_1(s) = \int^s [\gamma\theta(\hat{s}-u) - \delta(\hat{s}-u)] e^{-\gamma u} u^{\frac{\lambda s^*}{\eta}} du, \quad (49)$$

$$h_2(s) = \int^s [\gamma\theta(\hat{s}-u) - \delta(\hat{s}-u)] e^{\left(\gamma - \frac{\lambda}{\eta}\right)u} du.$$

In case of stress-avoidance or over-irrigation (i.e.,  $\tilde{s} \geq s^*$ ), Eq. (48) simplifies as

$$p(s) = \frac{C}{\eta} e^{-\left(\gamma - \frac{\lambda}{\eta}\right)(s-\tilde{s})} \left\{ 1 + e^{-\left(\gamma - \frac{\lambda}{\eta}\right)\tilde{s}} [h_2(s) - h_2(\tilde{s})] \right\}. \quad (50)$$

The integrals listed in Eq. (49) are analytically solvable, but for generic parameters they result in rather cumbersome expressions which will not be reported here. Conversely, whenever  $\tilde{s} < s^*$ , a numerical integration of Eq. (47) is needed to obtain the normalizing

constant  $C$ . While, in principle, the above formulation is able to describe the case of micro-irrigation as well, a cleaner formulation including the atom of probability  $p_0$  in  $\tilde{s}$ , can be obtained as described in Chapter 3 also for a generic  $\tilde{s}$ .

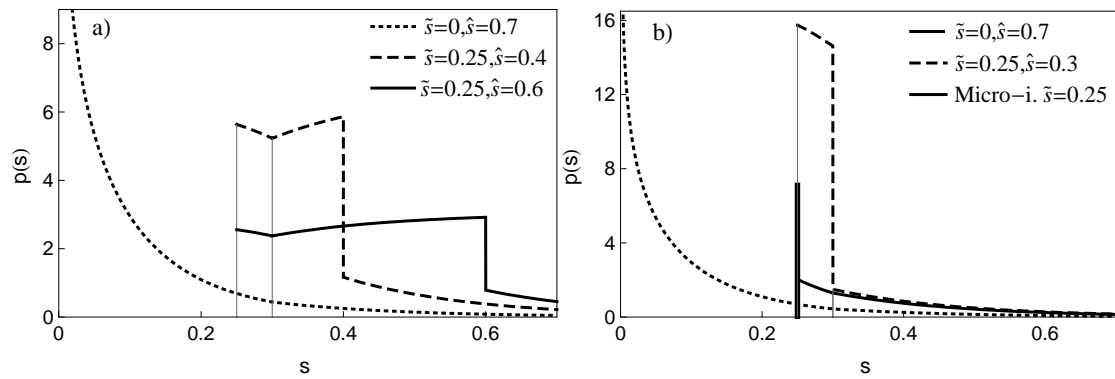


**Figure 4.2:** Example of steady state probability density functions of soil moisture relative to different choices of the parameters  $\tilde{s}$  and  $\hat{s}$ , as indicated. As a term of comparison, the soil moisture pdf for rainfed agriculture is represented (dotted lines), as well as the case of micro-irrigation (solid line in b)). Note that the vertical axes scale differ in a) and b); also, in b) the atom of probability in  $\hat{s}=0.25$  (thick vertical line) is not to scale. All the other parameters are as in Figure 4.1.

Examples of soil moisture pdfs are reported in Figure 4.2 for different choices of the parameters  $\tilde{s}$  and  $\hat{s}$ . In the most general case, the pdf of  $s$  exhibits different behaviors over the three ranges of soil moisture limited by  $\tilde{s}$ ,  $s^*$  and  $\hat{s}$ . Clearly, some of these ranges may not exist with particular choices of irrigation parameters. Above  $\hat{s}$  the pdf has the same shape it would be obtained for a rainfed agriculture, as the

distribution of probability in that range of soil moisture is not directly impacted by irrigation applications.

The frequency and duration of the excursions of the soil moisture process below a generic threshold  $s = \xi$  have been obtained before (Porporato et al. 2001), and may be used to infer the frequency of irrigation, which equals the frequency of downcrossing of threshold  $\xi = \tilde{s}$ , i.e.,

$$v_{\tilde{s}} = \rho(\tilde{s})p(\tilde{s}), \quad (51)$$

while the mean duration of each treatment is virtually zero. This is the case also for  $\hat{s} \rightarrow \tilde{s}$ , i.e. when micro-irrigation is obtained as a special case of the generalized traditional irrigation scheme described above: under such circumstances, in absence of rain, the virtually instantaneous irrigation is performed for several consecutive days in a row to balance evapotranspiration losses, thus resulting in periods of irrigation of non-zero duration (in agreement with Eq. (22)). Each irrigation treatment supplies a volume (per unit area)  $nZ_r(\hat{s} - \tilde{s})$ , hence the total volume for unit area required for irrigation purposes over a growing season of duration  $T_{seas}$  will be

$$V = nZ_r(\hat{s} - \tilde{s})v_{\tilde{s}}T_{seas} = nZ_r(\hat{s} - \tilde{s})\rho(\tilde{s})p(\tilde{s})T_{seas}. \quad (52)$$

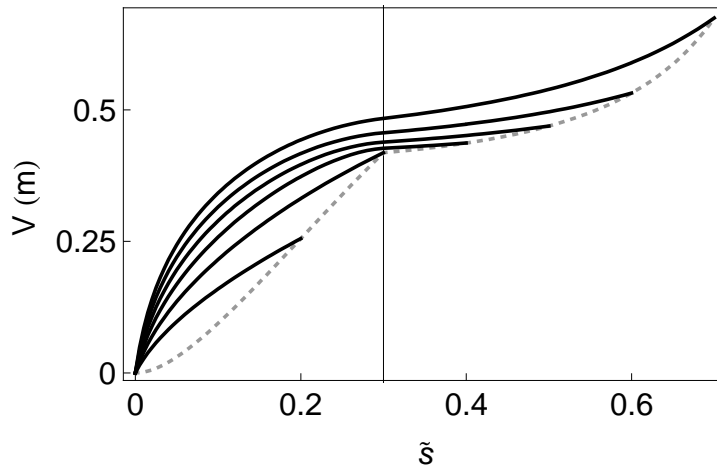


**Figure 4.3:** Irrigation volumes as a function of intervention point  $\tilde{s}$ , for different choices of irrigation parameter  $\hat{s}$  (from top to bottom,  $\hat{s}$  increases from 0.2 to 0.7). As reference the case of micro-irrigation is plotted as well (dotted line). The thin vertical line discriminate deficit irrigation (on the left) and over-irrigation (on the right). All the other parameters are as in Figure 4.1.

Figure 4.3 represents irrigation volumes for different choices of irrigation parameters, when rainfall statistics are kept constant. Clearly, the analysis is limited to the combination of parameters for which  $\tilde{s} \leq \hat{s}$ , where the equality corresponds to the case of micro-irrigation (dotted gray line in Figure 4.3). As expected, the higher  $\tilde{s}$ , the higher the volumes of water required over the growing season. The dependence of irrigation volumes on  $\tilde{s}$  becomes less marked as  $\hat{s}$  increases.

### **4.3 Average crop yield**

When soil moisture over the root zone decreases, plants respond with a number of adjustments (e.g., stomatal closure, reduction in CO<sub>2</sub> assimilation and respiration, changes in resource allocation; Hsiao (1973)), to limit transpiration rate and offset possible permanent damages. The reduction of transpiration rate is accompanied by a decrease in CO<sub>2</sub> assimilation rate, and possibly a depletion of crop yield. Given the fluctuating nature of soil moisture and its dependence on rainfall occurrence, plant water stress and hence productivity are clearly impacted not only by total precipitation, but also by precipitation timing (Appendix C; Ridolfi et al. 2000). In the following paragraphs, a simplified model linking average crop yield to the long term soil water balance is described and used to explore the impact of irrigation parameters on crop yield and economic profit.

#### **4.3.1 Crop water productivity functions**

Several classes of empirical relationships have been proposed to describe crop yield as a function of available rainfall and supplied water, or plant transpiration. Since the relevance of yield reduction due to water stress may depend on both the phenological stage in which the water deficit occurs, and on the extent of the deficit itself, such 'productivity functions' often include crop varying sensitivity to water shortage by combining the effects of water deficit on crop yield in specific growth stage

(for a comparison of selected crop water functions see Igbadun et al. (2007) and references therein). Nevertheless, while clearly the inclusion of plant stress sensitivity in the various growing stages would be more realistic and physiologically sound, the productivity functions for the single phenological stage have a shape similar to the relationship relative to the entire growing season. For the sake of simplicity, we aim at describing the ‘macroscopic’ effects of plant activity on crop yield and hence we assume here that crop yield is related to total seasonal transpiration (the latter has been shown to be well correlated with crop yield; Payero et al. (2006)). On the basis of empirical data relative to a variety of crops (Geerts and Raes 2009 and references therein), we assume a logarithmic function relating total seasonal transpiration to crop yield, i.e.,

$$Y(ET_{seas}; \alpha, \lambda) = \begin{cases} 0 & \text{if } ET_{seas} < ET_0 \\ \kappa \ln\left(\frac{ET_{seas}}{ET_0}\right) & \text{if } ET_{seas} \geq ET_0 \end{cases} \quad (53)$$

where  $ET_0$  represents the minimum total transpiration necessary to support the crop, while  $\kappa$  includes plant features such as maximum yield and plant water use efficiency over the entire growing season. Such a relationship is flexible enough to describe the most often observed features of productivity functions (i.e., the existence of a minimum transpiration to avoid total yield loss, the nearly linear dependence of yield on transpiration at intermediate  $ET_{seas}$ , the decrease in slope of the yield- $ET_{seas}$  relationship towards high  $ET_{seas}$  corresponding to well watered conditions; Geerts and Raes (2009)), while limiting the number of parameters. Both parameters in Eq. (53) are obtained

through regression of experimental data; in the following quantitative analysis, we will use wheat data as presented by Musick et al. (1994) (leading to  $ET_0 = 224$  mm ,  $\kappa = 4791$  kg ha<sup>-1</sup>;  $r^2=0.69$ ). Alternatively, Eq. (53) may be substituted by a piecewise linear function (see, e.g., Musick et al. 1994, Zhang and Oweis 1999 for wheat) or a quadratic relationship (see, e.g., Kang et al. 2002, Sun et al. 2006 for wheat).

This simplified approach of Eq. (53) is supported by several experimental results assessing the impact of irrigation withdrawal during different plant growth stages. Few examples are reported in Figure 4.4, where *Triticum aestivum* and *Zea mays* yields for different irrigation treatments are plotted against measured total transpiration. While accounting for the vegetative stage over which irrigation was reduced (here each symbol represents a different irrigation treatments) may help explaining some of the observed scatter, data are reasonably well described by the model in Eq. (53). Figure 4.4 also shows that the productivity function does not depend only on selected crop, but also on crop cultivar, soil features and climatic conditions.

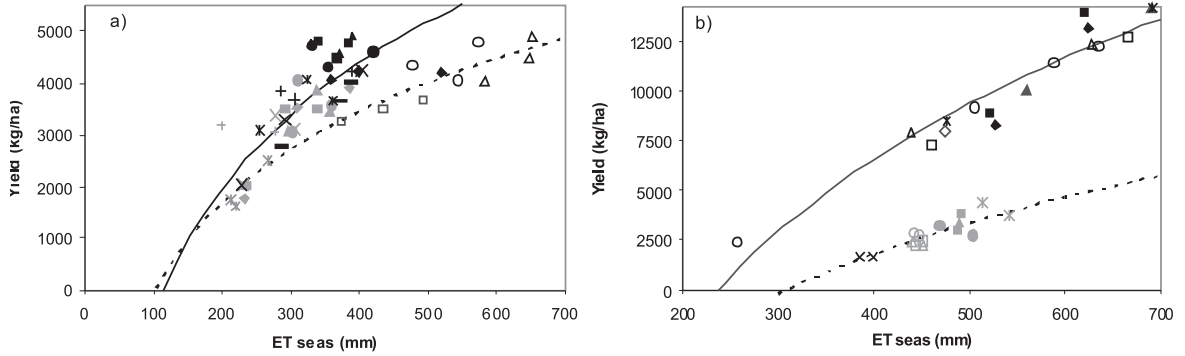


**Figure 4.4:** Observed crop yields as a function of total seasonal transpiration and fitted model for a) *Triticum aestivum* (open symbols and dotted line: Karam et al. (2009),  $r^2=0.70$ ; other symbols and solid line: Kang et al. (2002),  $r^2=0.66$ ) and b) *Zea mays* (dark symbols and line: Payero et al. (2006),  $r^2=0.91$ ; gray symbols and dotted line: Igbadun et al. (2007),  $r^2=0.72$ ). Different symbols refer to different irrigation treatments, consisting in a) maintenance of lower, intermediate or high soil water content, and b) irrigation withdrawal over different growth period (see sources of data for more details on irrigation treatments).

Under the assumption of stochastic steady state conditions, a first approximation of total seasonal transpiration is given by  $\langle ET \rangle T_{seas}$ , where  $\langle ET \rangle$  is mean daily transpiration rate, as obtained through the long term averages of the components of the soil water balance at the daily time scale (Eq. (40)). The nature of the hypothesized loss function (Eq. (41)) is such that  $\langle ET \rangle$  linearly depends on average soil moisture  $\langle s \rangle$  if the latter is smaller than  $s^*$ , while  $\langle ET \rangle = E_{max}$  whenever  $\langle s \rangle \geq s^*$ . Hence, crop yield is

$$\text{upper bounded by } \kappa \ln \left( \frac{E_{max} T_{seas}}{ET_0} \right).$$

### 4.3.2 Economic analysis

Under the assumptions discussed above (stochastic steady state conditions, piecewise linear loss function and logarithmic dependence of yield on total crop transpiration), soil moisture should be kept at or above the point of incipient stomatal closure  $s^*$  to maximize crop yield (i.e., a stress-avoidance irrigation should be performed). Nevertheless, yield maximization may not be the primary objective when water for irrigation purposes represents a significant cost, and enhancing water productivity may be more profitable. In such a case, an economic analysis, including the crop price and the fixed and variable costs, should be performed (English et al. 2002). For the sake of simplicity, we assume that the only variable cost is related to the amount of water employed for irrigation, all the other costs being fixed. Thus, net income per unit cultivated area may be expressed as (English 1990)

$$Net\ Income = c_c Y(ET_{seas}) - [c_F + c_w V], \quad (54)$$

where  $c_c$  is the crop sale price per unit crop,  $c_F$  are the fixed costs (irrigation equipment, field machinery and operations),  $c_w$  is the cost per unit volume water employed for irrigation. Assuming as guidelines the economic data for wheat grown in north-western Iran reported in Sepaskah et al. (2006) and setting  $c_F = 100$  arbitrary units  $ha^{-1}$ ,  $c_w = 35$  arbitrary units  $m^{-1} ha^{-1}$  and  $c_c = 0.05$  arbitrary units  $kg^{-1}$ . Clearly,  $c_w$  in general depends on location (and possibly amount of rainfall during the year or the

previous one), while  $c_c$  is determined by offer and demand, and depends on crop quality and year. For example, normalizing the data reported in English (1990) for wheat in the Columbia Basin leads to  $c_w = 1.6$  arbitrary units  $m^{-1} ha^{-1}$  and  $c_c = 0.02$  arbitrary units  $kg^{-1}$ .

In what follows, we explore which irrigation scheme and parameters may yield to the maximum net income, and the sensitivity of the latter to costs associated to irrigation water and rainfall pattern. In fact, while rainfall amount and timing, crop water requirements and economic parameters are generally fixed, it may be practical to alter the irrigation parameters for the sake of profit maximization. To this purpose, Figure 4.5 depicts the net income as a function of the irrigation parameter  $\tilde{s}$ , for micro-irrigation and for two generalized traditional irrigation scenarios ( $\hat{s}=0.4$  and  $\hat{s}=0.6$ ), for a linear dependence of water costs on applied water volumes but different costs of unit volume (Figure 4.5 a) black and gray lines).

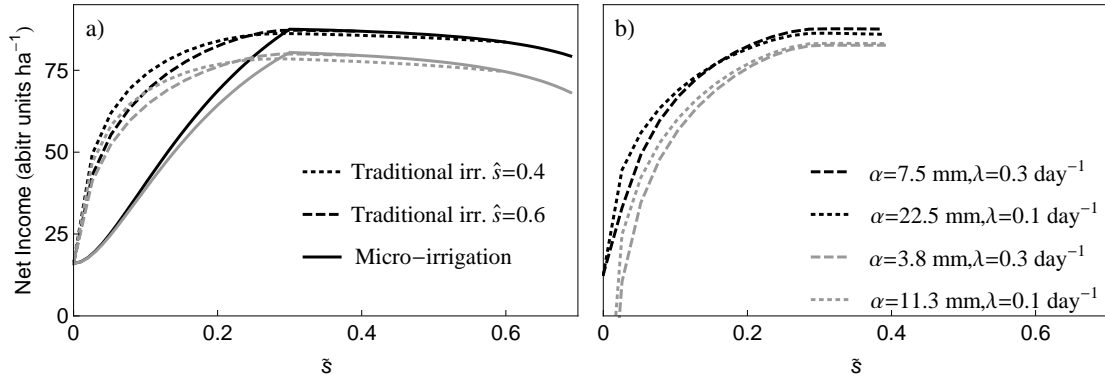


**Figure 4.5:** Net income as a function ‘intervention’ soil moisture  $\tilde{s}$  for a) different irrigation schemes (micro-irrigation: solid lines; traditional irrigation with  $\hat{s}=0.4$  and  $\hat{s}=0.6$ : dashed and dotted lines respectively) and water costs (gray lines refer to income for higher water costs), and b) different rainfall amounts ( $R_{tot} = 337$  mm and 168 mm for black and gray lines respectively) and timing ( $\lambda = 0.3$  and  $0.1$  day<sup>-1</sup> for dashed and dotted lines respectively).  $c_c = 0.05$  arbitrary units kg<sup>-1</sup>, while  $c_w = 35$  arbitrary units m<sup>-1</sup> ha<sup>-1</sup> (except for gray lines in a) where  $c_w = 53$  arbitrary units m<sup>-1</sup> ha<sup>-1</sup>). In a) total rainfall parameters are  $\alpha = 15$  mm and  $\lambda = 0.15$  day<sup>-1</sup>; in b) only the case of traditional irrigation with  $\hat{s} = 0.4$  is depicted. The growing season is supposed to last 150 days. All the other parameters are as in Figure 4.1.

As expected, the maximum income corresponds to the case of stress-avoidance micro-irrigation (i.e.,  $\tilde{s} = s^*$ ), regardless of water price. In fact, such irrigation scheme minimizes the amount of water lost to deep infiltration, while guaranteeing that plants do not experience water stress levels that may limit their productivity (Chapter Traditional and micro-irrigation with stochastic soil moisture<sup>3</sup>). These results support the use of micro-irrigation not only for a more sustainable employment of water but also for profit maximization. Note that in the above analysis we assumed that irrigation costs (both fixed and water related) are the same for traditional and micro-irrigation: higher

costs related to micro-irrigation installation (Brady and Weil 2002) or to the need of a continuous supply of water might render the traditional irrigation more profitable. Similar results to those presented in Figure 4.5a) would be obtained assuming a quadratic dependence of variable costs on irrigated volumes, with the exception of a more pronounced decrease in net income at higher  $\tilde{s}$  (and  $\hat{s}$ ; not shown), where supplied irrigation volumes are higher (see Figure 4.3).

The expected steep decrease in crop yield (and hence in net income) for micro-irrigation when soil moisture drops slightly below  $s^*$  (Figure 4.5a), solid lines) clearly shows that a successful irrigation depends on accurate soil moisture or plant stress sensing, to avoid counter-productive damages. As discussed in Jones (2004), it is problematic to precisely track soil moisture, and soil water actually available to crops may be not uniformly distributed in the field. Hence, it might be expected that, in reality, soil moisture fluctuates around the predicted value. If this is the case, a stress avoidance micro-irrigation with  $\tilde{s} = s^*$  might be risky, as a small reduction of the actual field  $\tilde{s}$  may result in a significant decrease in crop yield and thus net income. In contrast, traditional irrigation presents a less abrupt decrease in net profits when  $\tilde{s}$  drops below  $s^*$ , in particular if the parameter  $\hat{s}$  is set to higher values: however, in the latter case, expected net income is lower than the one for the  $\tilde{s} = s^*$  micro-irrigation, in particular at higher water costs. All these elements considered, a traditional irrigation with intermediate  $\hat{s}$  (e.g.,  $\hat{s}=0.4$ ) might be the most suitable choice for a number of

practical applications, particularly when water costs are relatively low if compared to fixed costs.

In Figure 4.5b) the impact of average rainfall amount and timing on net income is investigated; for the sake of simplicity, we focus on a traditional irrigation scenario with variable  $\tilde{s}$  and  $\hat{s}=0.4$ , for four different combinations of rainfall amounts and patterns. As expected, the higher the total rainfall over the growing season, the higher the net income, thanks to lower required irrigation volumes (Figure 4.5b), dark lines); such differences would be more significant for higher water costs (not shown). More interesting is the role of rainfall timing: for a deficit irrigation (i.e.,  $\tilde{s}$  below  $s^*$ ), the more frequent but less intense the rainfall events are, the higher the net income is thanks to smaller rainfall amounts lost to deep infiltration and runoff, and hence smaller water requirements to maintain similar plant stress levels over the growing season. In contrast, for  $\tilde{s}$  nearing  $s^*$ , intense but infrequent rainfall events may result in equal or even slightly higher profits than frequent but small events, because they force the soil moisture process to spend time above  $s^*$  (and possibly even above  $\hat{s}$ ), thus enhancing crop yield, without significantly increasing water losses. The  $\tilde{s}$  threshold at which the infrequent but large events are more productive depends on total precipitation over the growing season.

## **4.4 Interannual variability of crop yield**

In the previous sections, rainfall statistics were assumed constant, and depending only on location climate. Analyses of historical records of rainfall suggest strong interannual variability in daily rainfall statistics, which in turn has been shown to explain at least part of interannual variability in observed natural ecosystem primary production and crop yields (Appendix C; Robertson 1974, Lauenroth and Sala 1992, Knapp and Smith 2001). Nevertheless, variable rainfall and the associated economic risks has been seldom included in irrigation optimization models (English 1981, Sepaskhah and Akbari 2005, Oweis and Hachum 2009), despite its relevance for water management planning regarding both long-term water infrastructure choices and farmer level decisions at the beginning of each growing season (choice of crops, total area to be put into production and water allocation per unit area). In what follows, we investigate the impact of interannual rainfall variability on expected crop yields (and hence net income) and irrigation water requirements in a probabilistic framework.

### **4.4.1 Interannual variability of rainfall amount and timing**

Interannual fluctuations in rainfall depth and frequency can be realistically assumed to be independent, i.e.  $g(\alpha, \lambda) = g_\alpha(\alpha)g_\lambda(\lambda)$ . Analyses of daily rainfall records showed that a good model for such interannual variability is a two-parameter gamma distribution (Appendix C; D'Odorico et al. 2000), i.e.,

$$g_x(x) = \frac{b_x^{a_x}}{\Gamma(a_x)} x^{a_x-1} e^{-b_x x}, \quad (55)$$

where  $x$  stands for either  $\alpha$  or  $\lambda$ ,  $a_x$  and  $b_x$  are the shape and scale parameters of the distribution respectively, and  $\Gamma(\cdot)$  is the gamma function (Abramowitz and Stegun 1965).

#### **4.4.2 Impact of rainfall interannual variability on crop yield and choice of irrigation scheme**

In principle, the derived distribution technique (Kottegoda and Rosso 1998) allows to obtain the pdf of the derived variable  $Y$  accounting for rainfall interannual variability,  $p(Y)$ . However, the complexity of the dependence of  $Y(ET_{seas}; \alpha, \lambda)$  on  $\alpha$  and  $\lambda$  hampers any attempt to proceed analytically. Hence we explored the effects of climate and irrigation scheme on  $p(Y)$  through a Monte Carlo approach.

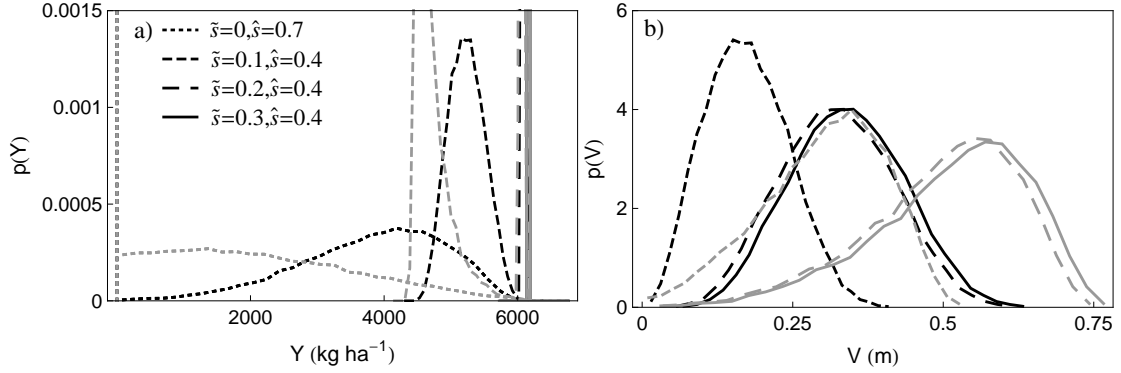


**Figure 4.6:** Probability density functions of a) average crop yield and b) irrigation volume for different values of  $\tilde{s}$ , once rainfall interannual variability is included. Rainfall parameters are those of Mahattan, eastern Kansas ( $a_\alpha = 21.8$ ,  $b_\alpha = 1.90 \text{ mm}^{-1}$ ,  $a_\lambda = 27.4$ ,  $b_\lambda = 91.9 \text{ day}$ ; black lines) and SGS LTER, northern Colorado ( $a_\alpha = 15.3$ ,  $b_\alpha = 2.56 \text{ mm}^{-1}$ ,  $a_\lambda = 6.35$ ,  $b_\lambda = 20.3 \text{ day}$ ; gray lines) (Appendix C). All the other parameters are as in Figure 4.1. In a) the average crop yield pdfs for rainfed agriculture are plotted for reference (dotted lines).

The model described above allows assessing the impact of frequency and amount of applied water, through a sensitivity analysis on the parameters  $\tilde{s}$  and  $\hat{s}$ . Regardless of rainfall amount and its interannual variability, the smaller the extent of the deficit irrigation (i.e., the higher  $\tilde{s}$ ), the higher and less variable the crop yield is (Figure 4.6a)). In fact, the intrinsic variability of rainfall amount and timing is compensated by the requested irrigation volumes, which become more and more variable (and clearly higher for lower intervention points  $\tilde{s}$ ; Figure 4.6a)). Hence, deficit irrigation decreases crop yield, while increasing its interannual variability (and the associated economic

risk). In contrast, a low-deficit irrigation requires higher amounts of water, that may change significantly from year to year, thus making water allocation more difficult. With the assumed piecewise linear loss function, stress avoidance irrigation ( $\tilde{s} = s^*$ ) or over-irrigation for salinization control ( $\tilde{s} > s^*$ ) are limit cases, exhibiting no variability in yield (which is distributed according to a Dirac delta distribution,  $\delta(Y - \kappa \ln(E_{\max} T_{seas} / ET_0))$ ), and an extreme variability in required irrigation water volumes. The impact of  $\hat{s}$  is less significant (not shown). Massive irrigation applications (i.e., high  $\hat{s}$ ) result in a slightly lower yield variability, with most of the changes observed at lower yield values, and causes a shift of the distribution of irrigation volumes towards higher values. Such a shift becomes more significant at higher  $\tilde{s}$ . From a practical standpoint, applying higher amount of waters at every irrigation treatment results in slightly more consistent (and higher) yields. The main drawback is that significant amounts of water are required to sustain these small enhancements in productivity and the increase in water cost may not be offset by the slightly higher and less variable productivity.

Figure 4.6 also allows assessing the impact of different rainfall patterns and level of interannual variability, since the crop yield and irrigation volume pdfs are plotted for two locations differing in rainfall statistics: Manhattan, in eastern Kansas, and Short Grass Steppe (SGS) Long-Term Ecological Research (LTER), in north-western Colorado (Appendix C). Both locations exhibit an average mean frequency event rate,  $\bar{\lambda}$ , around

0.3 d<sup>-1</sup>, but SGS presents a higher variability of  $\lambda$  (the standard deviation of  $\lambda$  at SGS is twice the one observed at Manhattan). The two locations significantly differ in mean storm depth,  $\bar{\alpha}$  ( $\bar{\alpha}$  at Manhattan is twice that of SGS, with a slightly higher degree of variability in  $\alpha$ ). The difference in  $\bar{\alpha}$  is responsible for the observed difference in average total precipitation (higher average rainfall amounts in Manhattan, KS). Such difference in total rainfall is clearly reflected on the pdfs of crop yield (note the atom of probability at zero yield predicted for SGS for rainfed agriculture; Figure 4.6a), dotted gray line, which is not present at Manhattan, KS). Moreover, higher volumes of water for irrigation are required for the same irrigation parameters.

#### **4.5 Discussion and conclusions**

We explored the impact of irrigation parameters on crop yield and net income, by linking a simplified model of soil moisture balance at steady state to average crop yield and economic profit, both for a single growing season and including rainfall interannual variability. Choice of irrigation parameters such as intervention point (i.e., the level of soil moisture that triggers a water application) and applied water volume at each treatment have significant impact on the resulting crop yield and net income associated to agriculture. While, as expected, stress avoidance micro-irrigation is the most convenient irrigation scheme for yield and profit maximization, other irrigation

strategies may be more suited for practical applications. In fact, such a fine-tuned irrigation may be difficult to apply (English et al. 2002, Jones 2004) and it might be expected that in reality soil moisture fluctuates around the predicted values. Our modeling results show that such fluctuations may be responsible for a significant reduction in net income, thus making traditional irrigation with intermediate amount of water applied at each treatment preferable in practice.

The inclusion of rainfall interannual variability provides a useful tool for long term water management and strategic irrigation choices, as it provides not only the expected values of crop yield, net income and required irrigation volumes, but also their probability distributions. As such, it allows determining the degree of risk associated to rainfall interannual variability in terms of probability of obtaining a certain minimum net income. Also, since such risk can be virtually erased by setting aside higher volumes of water for irrigation purposes, our results may offer guidance for irrigation planning to farmers with different levels of risk aversion (English 1981). When water is a limited resource, a farmer that is averse to risk will probably select less-than-optimal irrigation schemes, involving slightly abundant water applications to offset risks associated to uncertainties in crop physiological response to soil moisture and in soil water status assessments; also, at the beginning of the growing season, the farmer will allocate higher water volumes per unit cultivated area to limit the impact of rainfall interannual variability. Higher water use and higher water allocation per unit area will limit the land

put into production by the risk aversion farmer, thus limiting the maximum achievable profit. In contrast, the acceptance of higher risks may allow the farmer to put in production larger areas over which the limited water supply is to be distributed, thus maximizing the highest possible net income, but also its interannual variability.

## **5 Probabilistic description of topographic slope and aspect**

This chapter is based on the article Vico G. and A. Porporato (2009), Probabilistic description of topographic slope and aspect, *Journal of Geophysical Research*, Earth Surface Section, 114, F01011.

### **5.1 Introduction**

A wealth of research activity has been devoted to the scaling properties of river networks (e.g., Rodriguez-Iturbe and Rinaldo 1997, Rinaldo et al. 1998), the spatial scaling of topography (e.g., Dodds and Rothman 2000, Gagnon et al. 2006) and the space-time dynamics of topographic evolution, both in the context of surface growth processes (Sornette and Zhang 1993, Barabasi and Stanley 1995, Dodds and Rothman 2000, Sornette 2003) and of physically based erosion-deposition models (Willgoose et al. 1991, Tucker et al. 2001). On the other hand, the probabilistic description of local slope and aspect has received far less attention, despite their relevance to a number of ecological, hydrological, meteorological, and geomorphological processes.

Local aspect and slope directly determine the amount and timing of solar radiation, while nonlocal topographic features may be relevant in rugged landscapes through shadowing effects and changes in diffuse radiation (Pope and Lloyd 1975, Dubayah et al. 1990, Oliphant et al. 2003). These differences in solar radiation input in

turn may result in differences in temperature regimes, vapor pressure, and evapotranspiration (Barry 1992, Munro and Huang 1997, Essery 2001), which are crucial for species distribution and biodiversity both above-ground (e.g., Florinsky and Kuryakova 1996, Franklin 1998, Kumar and Skidmore 2000, van der Tol et al. 2007) and below-ground (e.g., Mahler et al. 1979, Moore et al. 1993, Florinsky et al. 2004). Furthermore, surface slope impacts CO<sub>2</sub> assimilation in plants by changing sunlit and shaded leaf area index (Wang et al. 2002).

Topography-driven differences in solar radiation input may be further enhanced by patterns in cloudiness induced by orography (e.g., Munro and Huang 1997, Turner et al. 1997, Hook and Burke 2000), while precipitation tends to be more abundant on wind-facing slopes (e.g., Barry 1992, Munro and Huang 1997, Essery and Pomeroy 2004). Topographically induced micro-climate also influences snow detention, melting and redistribution, as well as glacier location, predominant direction and evolution (Evans 2006). Slope and aspect may also impact soil properties and depth, and in turn soil water content (e.g., Hanna et al. 1982, Ridolfi et al. 2003), as well as erosion (Moore et al. 1993, Cerdà 1997, Pachepsky et al. 2001) and preferential development of soil crusting and sealing (Casanova et al. 2000). Finally, local slope and convexity, and distance from ridges are relevant factors for the occurrence of avalanches and landslides (Ancy et al. 2003, Maggioni and Gruber 2003).

While very little attention has been devoted to the probabilistic description of aspect, previous works analyzed the statistical distributions of slopes in a variety of landscapes. Slope distributions have been shown to be consistently unimodal, with multimodal frequency curves only in very heterogeneous landscapes (Speight 1971, Montgomery 2001, Wolinsky and Pratson 2005). Slope mean and standard deviation appear to vary independently (Speight 1971), while a systematic change from positively to negatively skewed distributions with increasing mean slope has been documented in a variety of landscapes, and linked to the dominant hillslope process (creep/wash at lower slopes, slope failure at higher slopes; (Wolinsky and Pratson 2005)). For smaller regions in north-western USA, Montgomery (2001) observed that slopes are exponentially-distributed when depositional processes predominate, while they are (approximately) Gaussian-distributed when active rock uplift is dominant.

Despite these sparse observations, a general statistical theory linking large-scale topographic features to the occurrence of slope and aspect is still lacking. Such a theory will provide a compact representation of major topographic features based on few parameters easily linkable to measurable properties of the landscape (anisotropy, elevation trends, drainage density, etc.), as well as to the climatic and geomorphologic processes that produced them. A simple and parsimonious statistical description of local topographic features would be useful in a variety of ecohydrological and climatological models which work at larger scales and necessitate a coarse-scale description of the local

links among topography, water and energy balances, and soil and plant biogeochemical processes. We hope that this research is a first contribution in this direction.

In this work, we explore the impact of large-scale topographic features, such as regional trends and anisotropy, on the probability density functions (pdf's) of slope and aspect. To this purpose, we assume smooth (i.e., differentiable) elevation fields and adopt relatively simple joint pdf's of elevation derivatives that are however flexible and realistic enough to reproduce the features of most landscapes. For these general classes of models, we obtain the pdf's of slope and aspect using derived distribution theory. We also briefly discuss possible stochastic models that reproduce such behaviors. Our theoretical results are compared to four case studies in the continental USA with different geomorphology, bedrock, tectonic history and climate (Figure 5.1). Finally, as an example of application, we employ the proposed statistical description of slope and aspect to explore the impact of topographic features on solar radiation mean and standard deviation. In this Chapter we limit our analysis to general models which provide simple pdf's to be used for large-scale descriptions of topography with few parameters. Future analyses will refine these statistical models to include the effects of fluvial and glacial erosion and deposition, as well as vegetation controls on erosion. We also plan to consider a wider variety of case studies to link the statistical parameters defining these pdf's to observable quantities of the landscape and to their geomorphologic and hydroclimatic drivers.

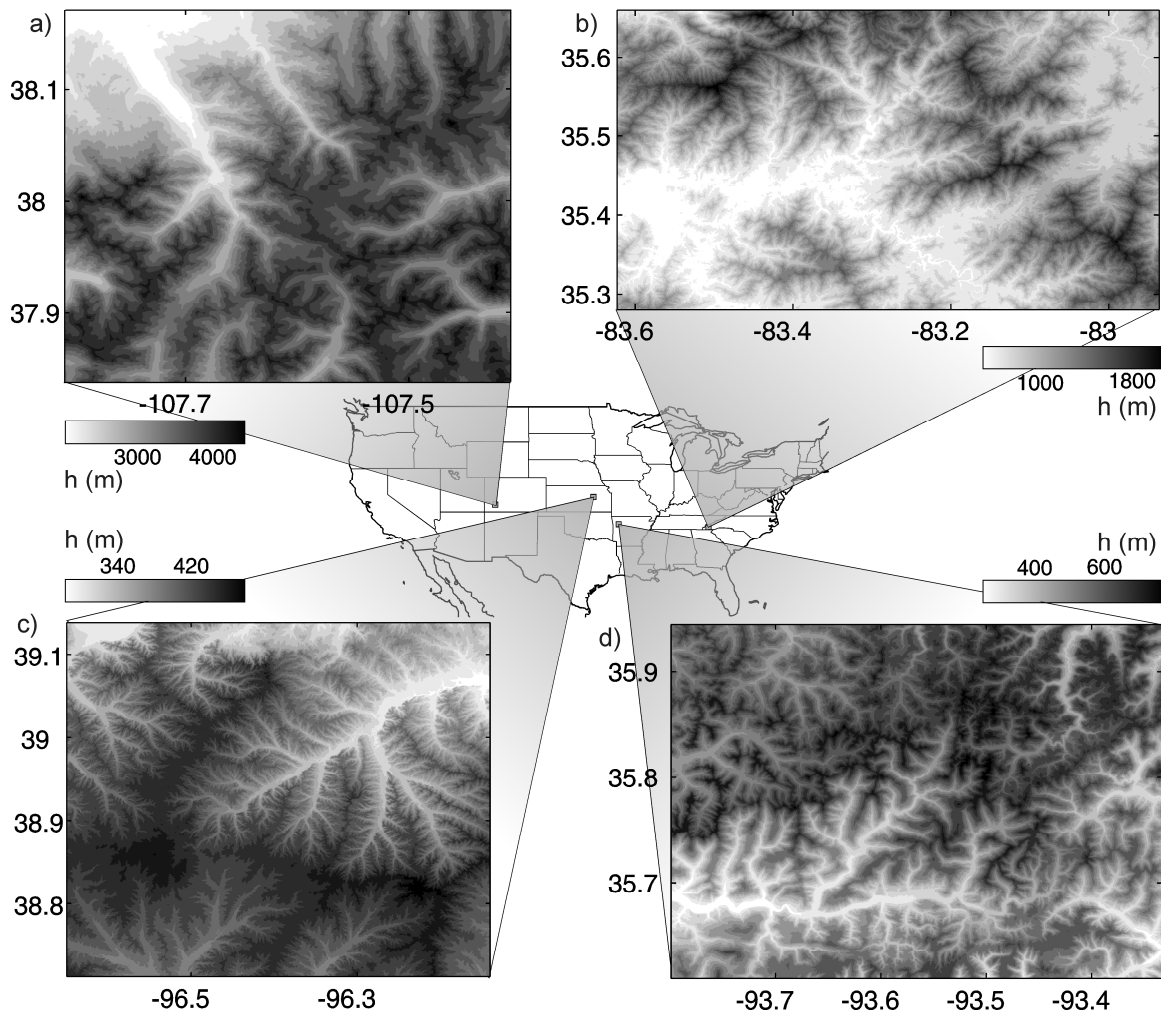


**Figure 5.1:** Case studies: i) south-western Colorado Rocky Mountains, ii) Smoky Mountains at the North Carolina-Tennessee border, iii) Flint Hills in north-eastern Kansas, and iv) Ozark Mountains in north-western Arkansas. Covered areas range from 1500 to 3100 km<sup>2</sup>, with boundaries independent of river network structure, and elevation differences between 564 to 2250 m. DEM data source is the USGS National Elevation Dataset (NED), with nominal horizontal resolution of 1 arc-second (approximately 30 meters along the Equator); elevations are resolved to the meter.

**Table 5.1:** Summary of parameters and results relative to the four case studies. As detailed in the text, parameters  $b_x$  and  $b_y$  in Eqs. (58) and (59) are equal to  $\mu_{\partial_x h}$  and  $\mu_{\partial_y h}$  respectively. The relative entropy is estimated from the observed aspect field using 64 partitions.

	Rocky Mts (Colorado)	Smoky Mts (North Carolina)	Flint Hills (Kansas)	Ozark Mts (Arkansas)
$\mu_{\partial_x h}$ (‰)	17.2	3.2	-0.61	0.50
$\mu_{\partial_y h}$ (‰)	-25	8.5	-1.94	5.2
$\sigma_{\partial_x h}$ (m m <sup>-1</sup> )	0.35	0.29	0.059	0.17
$\frac{\sigma_{\partial_x h}}{\sigma_{\partial_y h}}$	0.84	0.85	0.86	0.89
$\rho_{\partial_x h, \partial_y h}$	-0.008	-0.062	-0.082	-0.047
$\eta$	5.75	-	3.86	7.20
$D[p_\alpha(\alpha) \parallel (2\pi)^{-1}]$ (nats)	0.0108	0.0077	0.0053	0.031

## 5.2 Theory

### 5.2.1 Definitions and preliminaries

For each point of the topographic landscape  $\{x,y\}$  the rate of change of the elevation in directions  $x$  and  $y$  can be used to identify the magnitude and direction of the steepest gradient of the topographic elevation field,  $h(x,y)$ . The local slope  $S$  is defined as the magnitude of the gradient

$$S = \sqrt{(\partial_x h)^2 + (\partial_y h)^2}, \quad (56)$$

while the aspect  $\alpha$  is its direction

$$\alpha = \tan^{-1} \left( \frac{\partial_y h}{\partial_x h} \right). \quad (57)$$

Note that, if the  $x$  and  $y$  axes correspond to reference parallel and meridian, the aspect  $\alpha$  is measured counter-clockwise from west; the slope,  $S$ , is defined as magnitude of the gradient (elevation change per horizontal unit length), but can be easily transformed in degrees with respect to the horizontal plane ( $\beta = \tan^{-1} S$ ).

We assume that the actual topographic field  $h(x,y)$  may be represented probabilistically as a single realization of a two-dimensional random field. Large-scale landscape structures tend to make the topographic elevation field inhomogeneous in space. We assume for simplicity that such a field may be realistically represented by the sum of a homogeneous random field of zero mean,  $z(x,y)$ , and an independent deterministic linear trend, i.e.,

$$h(x, y) = z(x, y) + b_0 + b_x x + b_y y. \quad (58)$$

A linear trend is generally adequate for the description of weak trends and can be interpreted as a local linear approximation of more complex inhomogeneities. The parameters  $b_0$ ,  $b_x$  and  $b_y$  can be estimated by the least-square method. Among the four case studies (as expected) trends are more relevant in the south-western Rocky Mountains and the Smoky Mountains, small in the Ozark Mountain region, and almost negligible in the Flint Hills (Table 5.1).

In general, the full joint pdf of  $z(x,y)$ ,  $p[z(x_1, y_1), \dots, z(x_n, y_n)]$ , at an arbitrary large number  $n$  of locations  $\{x_i, y_i\}$  is needed to completely describe a spatial random field. However, our focus on local slope and aspect only requires the knowledge of the local properties of elevation fields (i.e., elevation at a point and its immediate neighbors) in terms of the first derivatives  $\partial_x h$  and  $\partial_y h$ . These will be regarded as homogeneous in space. Because of the linearity of the trend (Eq. (58))

$$\begin{aligned}\partial_x h &= \partial_x z + b_x \\ \partial_y h &= \partial_y z + b_y'\end{aligned}\tag{59}$$

and the mean and variance of the marginal distribution of  $\partial_x h$  are related to those of  $\partial_x z$  as  $\mu_{\partial_x h} = \mu_{\partial_x z} + b_x$  and  $\sigma_{\partial_x h}^2 = \sigma_{\partial_x z}^2$  (and similarly in direction  $y$ ). Also, the correlation coefficient between  $\partial_x h$  and  $\partial_y h$  is the same as that of  $\partial_x z$  and  $\partial_y z$ , i.e.  $\rho_{\partial_x h, \partial_y h} = \rho_{\partial_x z, \partial_y z}$ . Finally, because of the spatial homogeneity of  $z(x,y)$ , the means of its partial derivatives are zero, therefore  $\mu_{\partial_x h} = b_x$  and  $\mu_{\partial_y h} = b_y$ . Accordingly, the joint distribution of  $\partial_x h$  and  $\partial_y h$ ,  $p(\partial_x h, \partial_y h)$ , has the same shape of the joint distribution of  $p(\partial_x z, \partial_y z)$ , but shifted by  $b_x$  and  $b_y$  in directions  $x$  and  $y$  respectively.

A consequence of the homogeneity of the elevation field  $z(x,y)$  is that its correlation function only depends on the relative distance between points ( $l_x$  and  $l_y$ ), i.e.  $R_z(l_x, l_y) = \sigma_z^2 \rho_z(l_x, l_y)$  (Vanmarcke 1983). If the elevation field is differentiable in the mean square sense (i.e., if the covariance function has an approximately parabolic shape

around zero lag; Vanmarcke (1983)), the two-dimensional covariance function  $R_z(l_x, l_y)$ , is related to the autocovariance function of the random field of the partial derivative along  $x$ ,  $R_{\partial_x z}(l_x, l_y)$ , as (Vanmarcke 1983)

$$R_{\partial_x z}(l_x, l_y) = -\frac{\partial^2 R_z(l_x, l_y)}{\partial x^2}, \quad (60)$$

and similarly for  $y$ , while the crosscovariance function,  $R_{\partial_x z, \partial_y z}(l_x, l_y) = \sigma_{\partial_x z} \sigma_{\partial_y z} \rho_{\partial_x z, \partial_y z}(l_x, l_y)$ , is related to the covariance function of the homogeneous random field,  $R_z(l_x, l_y)$ , as (Vanmarcke 1983)

$$R_{\partial_x z, \partial_y z}(l_x, l_y) = -\frac{\partial^2 R_z(l_x, l_y)}{\partial x \partial y}. \quad (61)$$

When evaluated at zero lag (i.e.,  $l_x = l_y = 0$ ), Eqs. (60) and (61) provide the variance of the partial derivative in direction  $x$ ,  $\sigma_{\partial_x z}^2$  (a similar expression leads to  $\sigma_{\partial_y z}^2$ ), and the correlation coefficient between the partial derivatives,  $\rho_{\partial_x z, \partial_y z}$ . By definition, the field of elevations  $z(x, y)$  is isotropic if the correlation function has spherical symmetry, i.e. if  $R_z(l_x, l_y)$  is invariant to any rotation of the axes. In this case,  $\partial^2 R_z / \partial x^2 = \partial^2 R_z / \partial y^2$ , while the mixed second derivative is equal to 0. Hence, the isotropy of the elevation field translates in the following conditions relative to the partial derivative fields:  $\sigma_{\partial_x z} = \sigma_{\partial_y z}$  and  $\rho_{\partial_x z, \partial_y z} = 0$ . As discussed below, a homogeneous and isotropic elevation field will

result in a uniform distribution of aspect, regardless of the joint distributions of the partial derivatives of elevation.

The pdf's of slope and aspect can be obtained by representing the gradient vector in polar coordinates  $\{r, \theta\}$ . Defining slope and aspect as magnitude and direction of the gradient respectively (as in Eqs. (56) and (57)), the modulus  $r$  is equivalent to the slope  $S$ , and the direction  $\theta$  to the aspect  $\alpha$ . Given the joint distribution of the first partial derivatives in Cartesian coordinates,  $p(\partial_x h, \partial_y h)$ , a single one-to-one transformation of variables

$$\begin{aligned}\partial_x h &= S \cos \alpha \\ \partial_y h &= S \sin \alpha\end{aligned}\tag{62}$$

leads to the joint distribution of slope and aspect,  $p_{S,\alpha}(S, \alpha)$ , by means of the derived distribution technique (e.g., Kottegoda and Rosso 1998)

$$p_{S,\alpha}(S, \alpha) = |J| p(\partial_x h = S \cos \alpha, \partial_y h = S \sin \alpha),\tag{63}$$

where  $J=S$  is the Jacobian of the transformation represented by Eq. (62). The marginal distributions of  $p_{S,\alpha}(S, \alpha)$  are the desired pdf's of slope and aspect.  $p(S)$  and  $p(\alpha)$  can be obtained at least by numerical integration, regardless of the distribution of partial derivatives.

## 5.2.2 Slope

Some general characteristics of the distribution of slope can be discussed independently of the choice of the models of elevation derivatives. For example, the obtained slope distribution always has heavier tails than the joint distribution of the partial derivatives. Specifically, if the tails of the marginal pdf's of the derivatives decay as  $\sim |\partial_x h|^{-k}$ , then  $p_S \sim S^{-k+1}$ . This is a consequence of the transformation of variables in Eq. (62), the Jacobian of which is  $J=S$ .

Similar considerations can be used to explain the behavior of slope distributions at very low values. This is interesting, because, as discussed in the introduction, observed slope distributions have different behaviors depending on the dominant hillslope process (see, e.g., Burbank 1992, Montgomery 2001). Thus, considering again a decay like  $\sim |\partial_x h|^{-k}$ , now for  $\partial_x h \rightarrow 0$ , it follows that a finite non-zero value for  $p_S(S)$  is possible only if  $k=1$ , while the  $p_S(S)$  is zero at the origin if  $k<1$  and infinite for  $k>1$ . The exponential distribution of slopes, sometimes observed in low-relief or depositional environments (Montgomery 2001), is thus obtained for the special case of  $p(\partial_x h) \sim |\partial_x h|^{-1} \exp(-|\partial_x h|)$ . A uniform distribution of derivatives (i.e.,  $k=0$ ) gives rise to a linear increase of slope distribution with  $S$ .

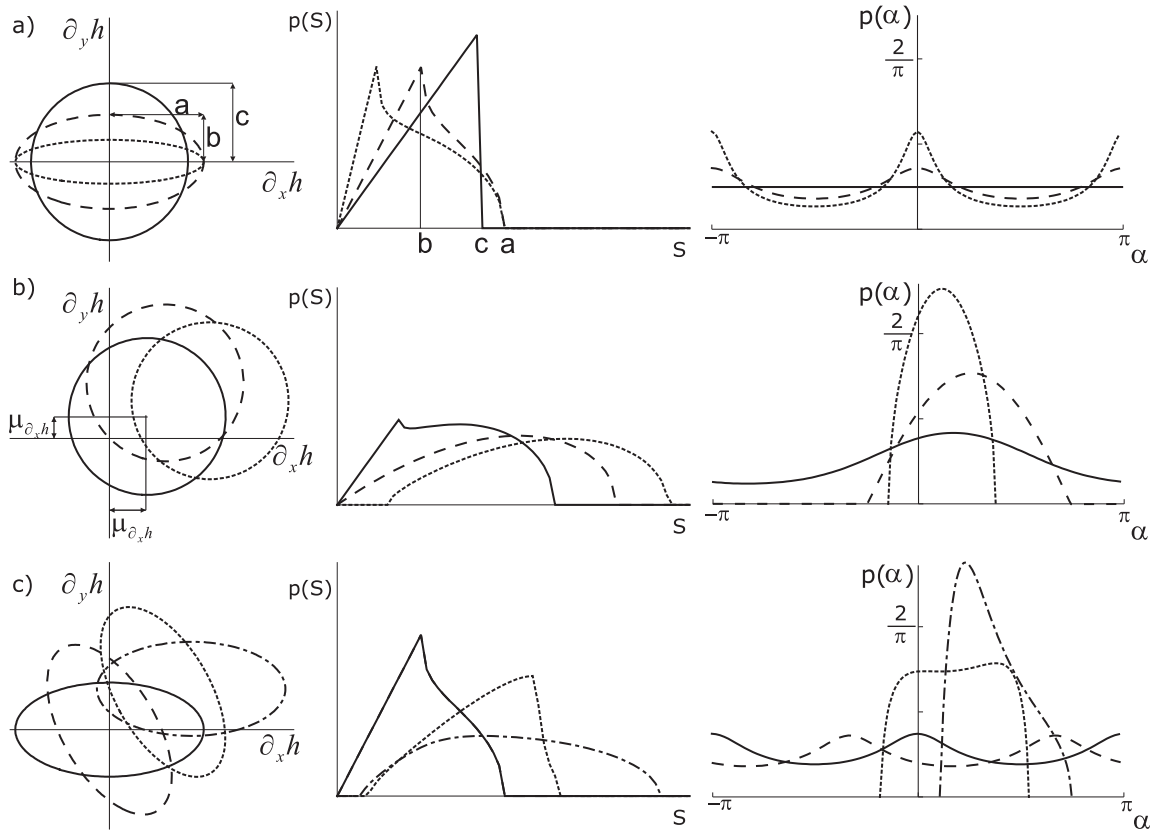


**Figure 5.2:** Impact of trends and degrees of anisotropy on slope and aspect distribution in the simple case of uniformly-distributed partial derivatives on an elliptical domain. From left to right columns contain the contour plots of the joint pdf  $p(\partial_x h, \partial_y h)$ , and the corresponding  $p_S(S)$  and  $p_\alpha(\alpha)$ . Rows from top to bottom explore the effects of anisotropy only (a), trend only (b), and their combination (c). In panel (a)  $a$  and  $b$  are the major and minor semi-axes of the elliptic domain of the partial derivative distributions, while  $c$  represents the radius of the domain in the isotropic case. In panel (b),  $\mu_{\partial_x h}$  and  $\mu_{\partial_y h}$  represents the means of  $\partial_x h$  and  $\partial_y h$  respectively, which correspond to the trend.

The effect of trends and anisotropy on the distribution of slope can be analyzed with reference to the simple case of uniformly distributed partial derivatives on an elliptical region in the space of the partial derivatives and having zero probability

elsewhere (Figure 5.2, left column). The anisotropy is due to both the ellipse eccentricity,  $\varepsilon = \sqrt{1 - b^2/a^2}$ , where  $a$  and  $b$  are the two semiaxes, and the rotation of its axes with respect to the reference system. The position of the ellipse center represents the trend components. For an isotropic elevation field ( $\varepsilon = 0$ , i.e.,  $a=b=c$ ) and no trend (i.e., the center of the circle is at the origin of the axes), the distribution of slope increases linearly with  $S$  (as discussed above), and the mode is  $S=c$  for the isotropic case (Figure 5.2a, solid lines), and  $S=b$  for an anisotropic elevation field (e.g., Figure 5.2b, dashed lines). In the latter case, the mode is followed by a curvilinear decrease in the pdf (Figure 5.2a, dashed and dotted lines). When the trend is small but non-zero, the distribution domain still contains the origin of the axes and there remains a linear increase of slope probability (Figure 5.2b, solid line). When the trend is further increased and the distribution domain no longer contains the origin, the initial linear part of the distribution disappears (Figure 5.2b, dashed and dotted lines). The latter however is a somewhat extreme case, which is quite unrealistic when one considers large regions. In all cases, slopes range between  $\max\left[0, a - \sqrt{\mu_{\partial_x h}^2 + \mu_{\partial_y h}^2}\right]$  and  $a + \sqrt{\mu_{\partial_x h}^2 + \mu_{\partial_y h}^2}$ . A similar pattern is observed for eccentric distributions ( $\varepsilon > 0$ ) as well (Figure 5.2c). The effect of a rotation is irrelevant when there is no trend (Figure 5.2c, solid and dashed lines), since the way the probability is distributed around the origin does not change.

### 5.2.3 Aspect

In a perfectly homogeneous and isotropic field, hillslopes do not have a preferential orientation, hence the distribution of aspect is uniform, i.e.,  $p_\alpha(\alpha) = (2\pi)^{-1}$ , regardless of the specific features of the joint distribution  $p(\partial_x h, \partial_y h)$ . Conversely, trends and anisotropy play an important role. This can be conveniently analyzed using again the simplified cases in Figure 5.2.

With no trend (Figure 5.2a), the anisotropy determines one preferential direction and thus two maxima (modes) of  $p_\alpha(\alpha)$ , which are  $\pi$  apart and more pronounced the more anisotropic the distribution is. Such modes are equally probable as long as the distribution of derivatives is symmetric with respect to the preferential direction (e.g., mode coinciding with mean; Figure 5.2a).

When the trend is non-negligible but the distribution is isotropic, the aspect distribution is unimodal, with the mode in the same direction of the trend (Figure 5.2b). The stronger the trend is the more pronounced the mode is. With both trend and anisotropy, the two opposite modes generated by the anisotropy compete with the single mode due to the trend, with the result that the two modes become unequal in probability and move closer to each other (Figure 5.2c).

Finally we note that a useful measure of the degree of non-uniformity of the aspect distributions (and thus of the impact of anisotropy and trend on aspect) can be obtained

using the relative entropy between the actual aspect distribution and the corresponding uniform case (Cover and Thomas 1991), i.e.,

$$D[p_\alpha(\alpha) \parallel (2\pi)^{-1}] = \int_{-\pi}^{\pi} p_\alpha(\alpha) \log|2\pi p_\alpha(\alpha)| d\alpha. \quad (64)$$

The relative entropy is always non-negative, and zero if and only if  $\alpha$  is uniformly distributed. This measure will be analyzed for the four case studies, through a numerical approximation of the integral in Eq. (64).

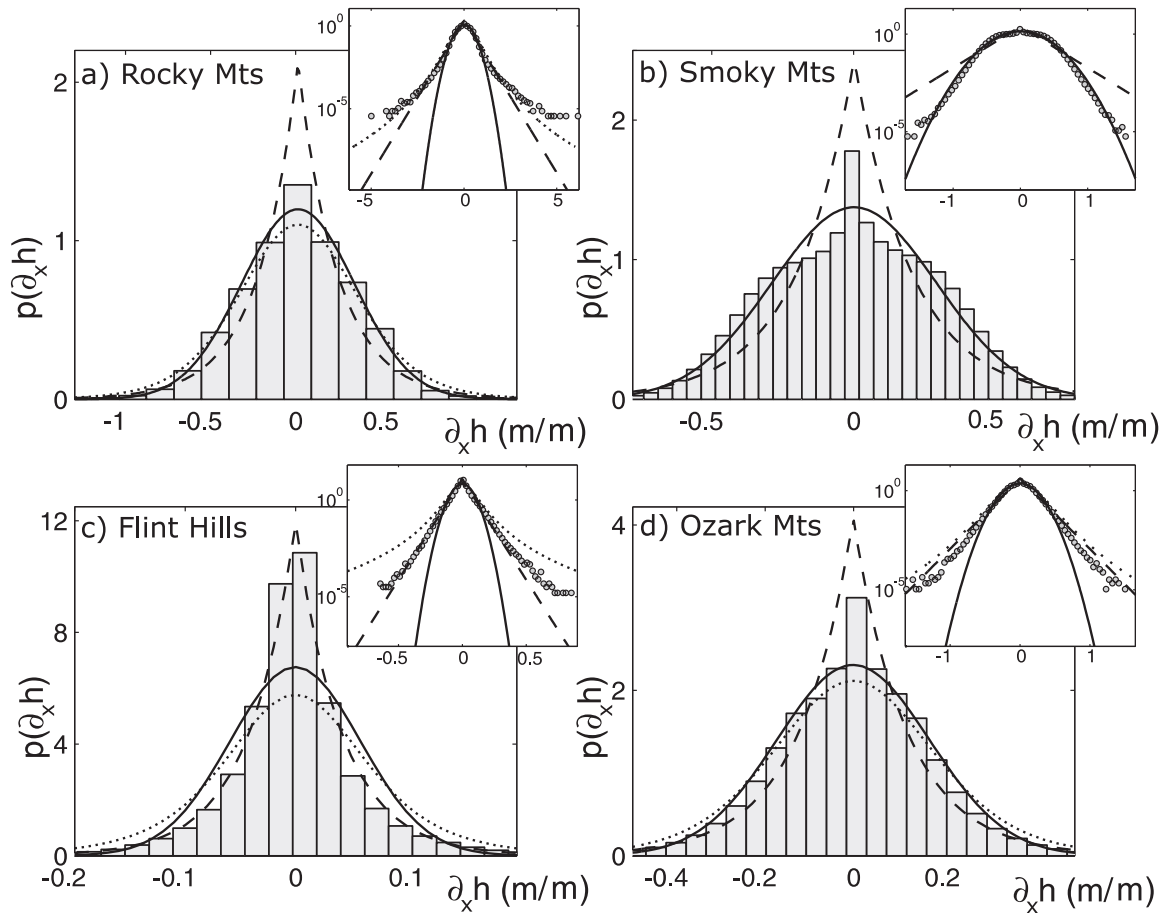


**Figure 5.3:** Comparison between observed derivatives in orthogonal directions and assumed marginal distributions for the four case studies (Figure 5.1) both in linear scale (main plots) and semi-logarithmic scales (insets, to enhance tail behavior). The different lines represent the theoretical pdf's under different assumptions on the distribution of the first partial derivatives: Gaussian joint pdf (solid lines), Laplace joint pdf (dashed) and Pearson type VII joint pdf (dotted). Pdf parameters have been estimated directly from the fields of partial derivatives and are listed in Table 5.1; given the nature of the observed partial derivatives in the Smoky Mountain area, no attempt has been made to fit the Pearson type VII marginal distributions in this case. Derivative values are obtained assuming a nominal resolution of 30 m, despite the differences in site latitudes.

### 5.3 Models of derivatives of elevation

As it appears from the definitions (Eqs. (56) and (57)), the probabilistic structure of slope and aspect directly depends on the joint distribution of the partial derivatives of the elevation field,  $p(\partial_x h, \partial_y h)$ . We begin by using observations of marginal pdf's to guide our choice of the joint pdf. Figure 5.3 reports the histograms of the calculated finite differences of the elevation field in the  $x$  direction (similar results are obtained in the  $y$  direction) for all the four case studies. The histograms are strongly unimodal, with the values clustered around the component of the trend (equivalent to the mean of the derivatives thanks to the assumed linearity of the trend). In contrast, as apparent in the semi-logarithmic plots (Figure 5.3, insets), the tail behavior shows a greater variability, ranging from Gaussian to power-law tails. Regarding the estimate of  $\sigma_{\partial_x z}$ ,  $\sigma_{\partial_y z}$  and  $\rho_{\partial_x z, \partial_y z}$  the direct determination by means of a centered-difference approximation of  $\partial_x h$  and  $\partial_y h$  is the most practical and reliable. In principle, the same parameters could be estimated by evaluating the derivatives of the correlation function at zero lag (Eqs. (60) and (61)). This method, however, is less reliable, because the resulting estimates strongly depend on the model chosen for the correlation function around zero lag (Vanmarcke 1983, p.113).

We adopt three different hypotheses on the joint distribution of the first partial derivatives: i) a bivariate Gaussian distribution, ii) a bivariate double exponential

(Laplace) distribution, and iii) a bivariate Pearson type VII distribution. They are potentially adequate to describe the observed data since they all are unskewed, unimodal and sufficiently diverse to cover different behaviors of the tails of the distributions. We keep intentionally simple the models of partial derivative distributions because we aim at exploring the impact of large-scale topographic features on slope and aspect distributions. Furthermore, we seek a compact statistical description of topographic features, based on few parameters. Some details, such as the marked peak at low values of the derivatives in the observed histograms, might be of geomorphological interest. Nevertheless, the inclusion of such details would considerably complicate the analyses and will thus be postponed to future contributions.

The adopted bivariate Gaussian distribution has the well-known expression

$$p_G(\partial_x h, \partial_y h) = \frac{1}{2\pi \sigma_{\partial_x h} \sigma_{\partial_y h} \sqrt{1 - \rho_{\partial_x h, \partial_y h}^2}} \exp \left[ -\frac{1}{2(1 - \rho_{\partial_x h, \partial_y h}^2)} \left( \frac{\partial_x h^{*2}}{\sigma_{\partial_x h}^2} - 2\rho_{\partial_x h, \partial_y h} \frac{\partial_x h^* \partial_y h^*}{\sigma_{\partial_x h} \sigma_{\partial_y h}} + \frac{\partial_y h^{*2}}{\sigma_{\partial_y h}^2} \right) \right], \quad (65)$$

where  $\partial_x h^* = \partial_x h - \mu_{\partial_x h}$  and  $\partial_y h^* = \partial_y h - \mu_{\partial_y h}$ , and  $\mu_{\partial_x h}$  and  $\mu_{\partial_y h}$  are the means of  $\partial_x h$  and  $\partial_y h$  respectively,  $\sigma_{\partial_x h}$  and  $\sigma_{\partial_y h}$  their standard deviations, and  $\rho_{\partial_x h, \partial_y h}$  their correlation coefficient. This model may be theoretically justified by the fact that the elevation gradients of some nonlinear growth models, frequently generating fractal surfaces (e.g., the Kardar-Parisi-Zhang equation), have Gaussian distributions without necessarily having Gaussian elevation fields (e.g., Barabasi and Stanley 1995, Halpin-Healy and Zhang 1995, Krug 1997).

The univariate Laplace distribution has been already employed in the literature to describe the distribution of first partial derivatives (assumed to be independent and with no trend; (Essery 2001, Essery and Pomeroy 2004)). Here we extend this model by using a non-central bivariate Laplace (double exponential) distribution to take into account possible trends and correlation between the derivatives. Specifically, we adopt the following expression for the bivariate Laplace distribution (McGraw and Wagner 1968)

$$p_L(\partial_x h, \partial_y h) = \frac{1}{\pi \sigma_{\partial_x h, \partial_y h}^2 \sqrt{1 - \rho_{\partial_x h, \partial_y h}^2}} K_0 \left( \sqrt{\frac{2\partial_x h^{*2} - 4\rho_{\partial_x h, \partial_y h} \partial_x h^* \partial_y h^* + 2\partial_y h^{*2}}{\sigma_{\partial_x h, \partial_y h}^2 (1 - \rho_{\partial_x h, \partial_y h}^2)}} \right), \quad (66)$$

where  $K_0(\cdot)$  is the zeroth order modified Bessel function of the second kind (Abramowitz and Stegun 1965). Differently from Eq. (65), there is a single parameter accounting for the standard deviation of the orthogonal derivatives, i.e.,  $\sigma_{\partial_x h, \partial_y h}$ , which we assumed to be well represented by the arithmetic mean of the two standard deviations  $\sigma_{\partial_x h}$  and  $\sigma_{\partial_y h}$ . Such assumption is mainly motivated by the observed relative small difference between the standard deviation of the orthogonal derivatives in all case studies (Table 5.1). It should be noted that in the isotropic case, along the radial direction the two distributions described above belong to the exponential power distribution (EPD) family,  $p(\partial_x h) \sim \exp(-|\partial_x h|^k)$  (Shi et al. 2005).

Finally, the bivariate Pearson type VII distribution used as a third model corresponds to (McGraw and Wagner 1968)

$$p_P(\partial_x h, \partial_y h) = \frac{\eta - 1}{\pi m \sqrt{1 - \rho_{\partial_x h, \partial_y h}^2}} \left\{ 1 + \frac{\partial_x h^{*2} - 2\rho_{\partial_x h, \partial_y h} \partial_x h^* \partial_y h^* + \partial_y h^{*2}}{m(1 - \rho_{\partial_x h, \partial_y h}^2)} \right\}^{-\eta}, \quad (67)$$

where  $\eta$  controls the relative importance of the tails, while  $m$  is a normalization parameter. The Pearson type VII distribution is rather flexible and includes the  $t$ -Student and Cauchy distributions as special cases. For  $|\partial_x h|$  and  $|\partial_y h| \gg 1$ , it decays algebraically with exponent  $-2\eta$ . Drawing on the formulation of the bivariate  $t$ -Student as a special case, we link the normalizing parameter  $m$  to  $\eta$  and to the overall measure of the standard deviations as  $m = 2(\eta - 1)\sigma_{\partial_x h, \partial_y h}^2$ . In turn, in what follows  $\eta$  is determined from averaged kurtosis of the orthogonal first partial derivatives using the method of moments, thus focusing on the fitting of the observed extreme values.

In Figure 5.3 the fitted marginal pdf's of  $\partial_x h$  are compared with the histograms of the calculated finite difference of the elevation field (similar results are obtained in the  $y$  direction). The proposed distributions are adequate to capture the overall distribution of partial derivatives (any goodness-of-the-fit test of these bivariate distributions is beyond the scope of the current research). The Flint Hills are very well described by the Laplace distribution, even at low values of  $\partial_x h$ . This is due to the terraced topography typical of the area, with vast uplands and frequent flat-floored valleys (likely responsible for the

histogram peak at low partial derivative values), connected by steep valley walls. On the contrary, in the other case studies, the model that best describes the extreme values of the partial derivative does not capture equally well the mode of the distribution. In these case studies, at least two mechanisms seem to coexist: one shaping the pdf of derivatives around the origin and likely associated to depositional areas in lowlands, and another one responsible for the body and tail behavior of the distributions possibly related to the balance between rock uplift and erosion. The existence of the first mechanism becomes evident when observing the derivative histograms relative to areas below and above the median elevation (not shown). With the exception of the Flint Hills, the pdf's of derivatives below the median elevation present a more pronounced peak at low derivatives values, indicating a high probability of almost flat depositional areas. The second process, shaping the body and tails of the pdf's, seems to produce pdf's that go from Gaussian distributions for the Smoky Mountains, to Laplace and stretched exponential distributions for the Flint Hills and Ozark Mountains (eroded in sedimentary rocks), up to heavy-tailed distributions for the Rocky Mountains. Detailed geomorphological analyses including several test cases from different regions should be carried out to link the above statistical descriptors to the relevant observable landscape properties, but this is outside our scope here.

## 5.4 Distributions of slope

For all the three models adopted for first partial derivatives of elevation, analytical pdf's of slope are obtainable only under the hypotheses of negligible trend (i.e.,  $\mu_{\partial_x h} = \mu_{\partial_y h} = 0$ ) and uncorrelated first partial derivatives (i.e.,  $\rho_{\partial_x z, \partial_y z} = 0$ ). Assuming Gaussian-distributed first partial derivatives (Eq. (65)), the pdf of  $S$  can be shown to be

$$p_G(S) = \frac{S}{\sigma_{\partial_x h} \sigma_{\partial_y h}} I_0 \left( S^2 \frac{|\sigma_{\partial_x h}^2 - \sigma_{\partial_y h}^2|}{4\sigma_{\partial_x h}^2 \sigma_{\partial_y h}^2} \right) \exp \left( -S^2 \frac{\sigma_{\partial_x h}^2 + \sigma_{\partial_y h}^2}{4\sigma_{\partial_x h}^2 \sigma_{\partial_y h}^2} \right), \quad (68)$$

where  $I_0(\cdot)$  is the zeroth order modified Bessel function of the first kind (Abramowitz and Stegun 1965). If the random field of the first partial derivatives may be considered isotropic (i.e.,  $\sigma_{\partial_x h} = \sigma_{\partial_y h}$  in addition to the zero correlation hypothesis), the above pdf simplifies as

$$p_G(S; \sigma_{\partial_x h} = \sigma_{\partial_y h}) = \frac{S}{\sigma_{\partial_x h, \partial_y h}^2} \exp \left( -\frac{S^2}{2\sigma_{\partial_x h, \partial_y h}^2} \right), \quad (69)$$

which is a power-exponential distribution (stationary distribution of the Rayleigh process, e.g., Gardiner (1990) p. 135; see also Longuet-Higgins (1957) for a similar result), with characteristic scale  $\sqrt{2}\sigma_{\partial_x h, \partial_y h}$  and exponent 2 (Sornette 2003).

Considering a bivariate Laplace distribution for the partial derivatives (Eq. (66)), the pdf of  $S$  reads

$$p_L(S) = \frac{2S}{\sigma_{\partial_x h, \partial_y h}^2} K_0 \left( S \frac{\sqrt{2}}{\sigma_{\partial_x h, \partial_y h}} \right) \quad (70)$$

where, as in Eq. (66),  $K_0(\cdot)$  is the zeroth order modified Bessel function of the second kind (Abramowitz and Stegun 1965); for  $S \gg 1$ ,  $p_L(S) \sim \sqrt{S} e^{-S}$ .

For the Pearson type VII distribution (Eq. (67)), the following expression for the pdf of  $S$  holds

$$p_P(S) = 2(\eta - 1)m^{\eta-1} \frac{S}{(m + S^2)^\eta}; \quad (71)$$

in the limit  $S \rightarrow \infty$ , the pdf of  $S$  decreases as  $S^{1-2\eta}$ .

All the obtained pdf's of slope are unimodal (Figure 5.4), in agreement with the observations from a variety of landscapes (Speight 1971, Wolinsky and Pratson 2005 and references therein). The obtained pdf's are positively skewed (in the case of Eq. (71),  $\eta > 5/2$  for the skewness to be finite); hence, according to the interpretation of Wolinsky and Pratson (2005), they are particularly suitable for areas where creep and wash sediment transport mechanisms dominate. Furthermore, given the features of the chosen models,  $p(S)$  goes to zero at the origin.

As observed in Section 5.2.2, the tails of the slope distribution are heavier than the tails of the original partial derivative distributions. To quantify the impact of the distribution parameters on the weight of the tails, we analyzed how they affect the kurtosis of slope distribution. For example, Gaussian partial derivatives lead to slope

distributions with kurtosis ranging from 3.25 to 4.17, with the minimum kurtosis obtained for isotropic elevation fields (Eq. (69)) and the maximum when the ratio of the standard deviations is 3 (i.e., for strongly anisotropic fields).

When trends in  $h(x, y)$  and  $\rho_{\partial_x h, \partial_y h}$  are non-negligible, the distribution of slope can only be obtained numerically. A sensitivity analysis showed that, using observed values of the trends (Table 5.1), the differences between the theoretical distributions obtained with and without trend and correlation are negligible. Nevertheless, it is interesting to evaluate the impact of non-weak trends on  $p(S)$ : as expected, the inclusion of a strong trend results in a shift of the mode towards higher values. Such a mode becomes less pronounced for Gaussian or Pearson type VII joint distributions, while Laplace-distributed derivatives the pdf becomes more peaked around the mode. The intensity of such changes depends on the relevance of the trend, regardless of its direction.

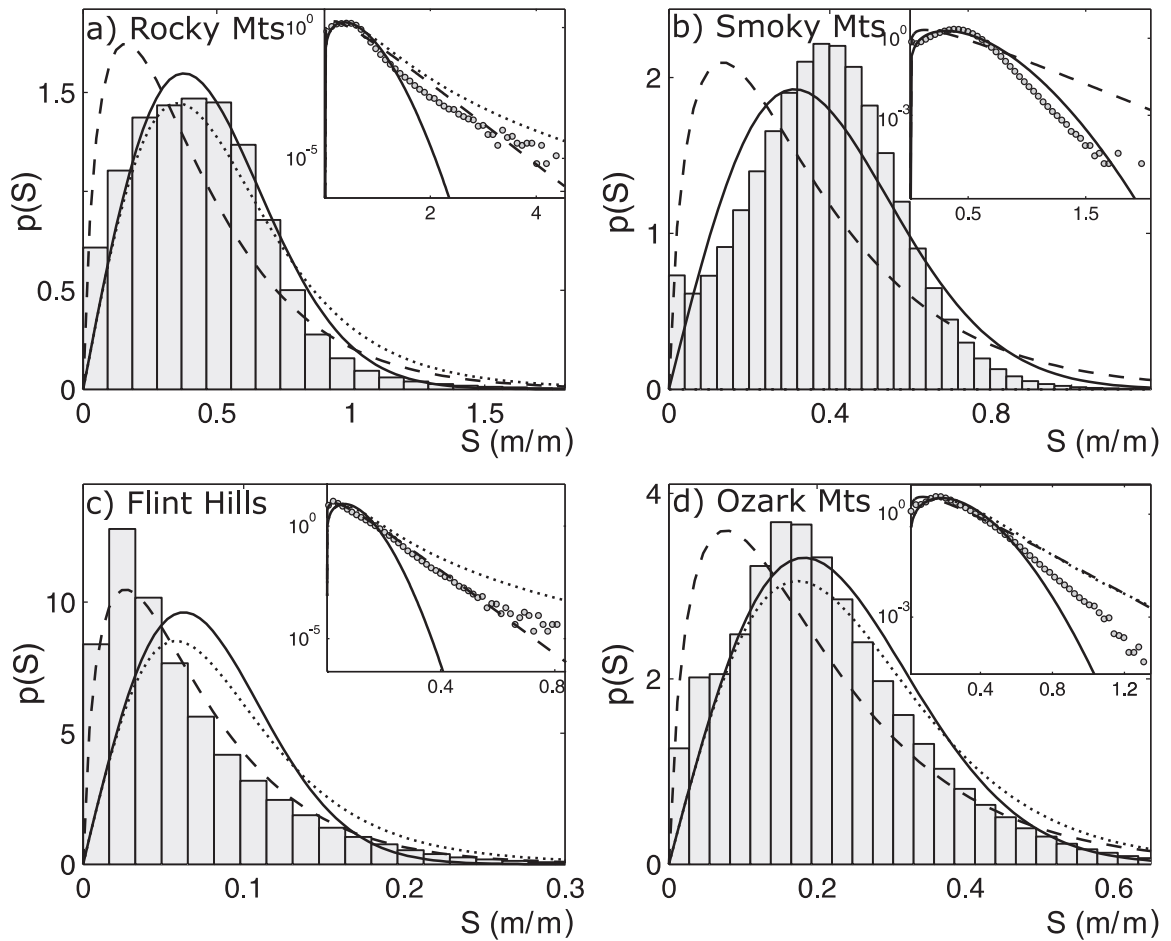


**Figure 5.4:** Comparison with data of derived slope pdf's including trend and correlation between first derivatives. Lines and plots are as in Figure 5.3.

In Figure 5.4 the slope distributions observed in the four case studies are compared to the theoretical pdf's obtained by numerical integration, accounting for trend and correlation. All distributions have positive skewness, with increasing values from Rocky Mountains to Smoky Mountains and Ozark Mountains, in agreement with the documented relationship between mean slope and skewness of its distribution (Wolinsky and Pratson 2005). In the Flint Hills, the dominance of terraced topography

results in a higher skewness. The steep valleys and relatively rare flat areas in the Colorado Rocky Mountains result in a heavy-tailed slope distribution, thus making  $p(S)$  obtained using the Pearson type VII for the partial derivatives the most suitable distribution for describing the data (Figure 5.4a). For the Smoky Mountains the  $p(S)$  obtained assuming Gaussian-distributed partial derivatives works well, apart from some underestimation of the mode (Figure 5.4b). In this case study, observed slope histogram exhibits a second mode at very low  $S$ , possibly associated with flat-floored valleys, which, however, is not captured by the current parametrization. For the Flint Hills, the slope distribution obtained from Laplace-distributed partial derivatives is best suited to describe the observations, in spite of its slight underestimate at high slopes (Figure 5.4c). Finally, the slopes observed in the Ozark Mountains have intermediate tails, in between those obtained by assuming Gaussian and Laplace-distributed partial derivatives (Figure 5.4d).

## **5.5 Distributions of aspect**

For all the partial derivative models considered, the analytical determination of  $p_\alpha(\alpha)$  from  $p_{S,\alpha}(S, \alpha)$  is only feasible when the trend is neglected. Under this assumption, for Gaussian distributed derivatives, integrating the polar formulation of Eq. (65) over  $S$ , yields

$$p_{\alpha}(\alpha) = \frac{\sigma_{\partial_x h} \sigma_{\partial_y h} \sqrt{1 - \rho_{\partial_x h, \partial_y h}^2}}{2\pi} \left[ \sigma_{\partial_y h}^2 \cos^2 \alpha - 2\rho_{\partial_x h, \partial_y h} \sigma_{\partial_y h} \sigma_{\partial_x h} \cos \alpha \sin \alpha + \sigma_{\partial_x h}^2 \sin^2 \alpha \right]^{-1} \quad (72)$$

where  $\alpha \in [-\pi; +\pi]$ . Under the further assumption of partial derivatives having the same standard deviation, the above pdf simplifies to

$$p_{\alpha}(\alpha; \sigma_{\partial_x h} = \sigma_{\partial_y h}) = \frac{\sqrt{1 - \rho_{\partial_x h, \partial_y h}^2}}{2\pi} \left[ 1 - 2\rho_{\partial_x h, \partial_y h} \cos \alpha \sin \alpha \right]^{-1}, \quad (73)$$

which, as expected, further simplifies into a uniform distribution for an isotropic field (i.e.,  $\rho_{\partial_x h, \partial_y h} = 0$  in addition to  $\sigma_{\partial_x h} = \sigma_{\partial_y h}$ ). Since  $p_{\alpha}(\alpha)$  does not depend on the specific features of the partial derivatives distribution when the trend is neglected (Section 5.2.3), Eq. (73) is obtained also under the assumption of Laplace- or Pearson-distributed partial derivatives.

When the trend is non-negligible, a numerical integration of  $p_{S, \alpha}(S, \alpha)$  is needed to determine  $p_{\alpha}(\alpha)$ . The obtained pdf is generally bimodal, with peaks occurring approximately in the direction of the estimated trends. However it is no longer independent of the assumption on the partial derivatives, with a stronger impact of the trend for distributions with more pronounced mode.

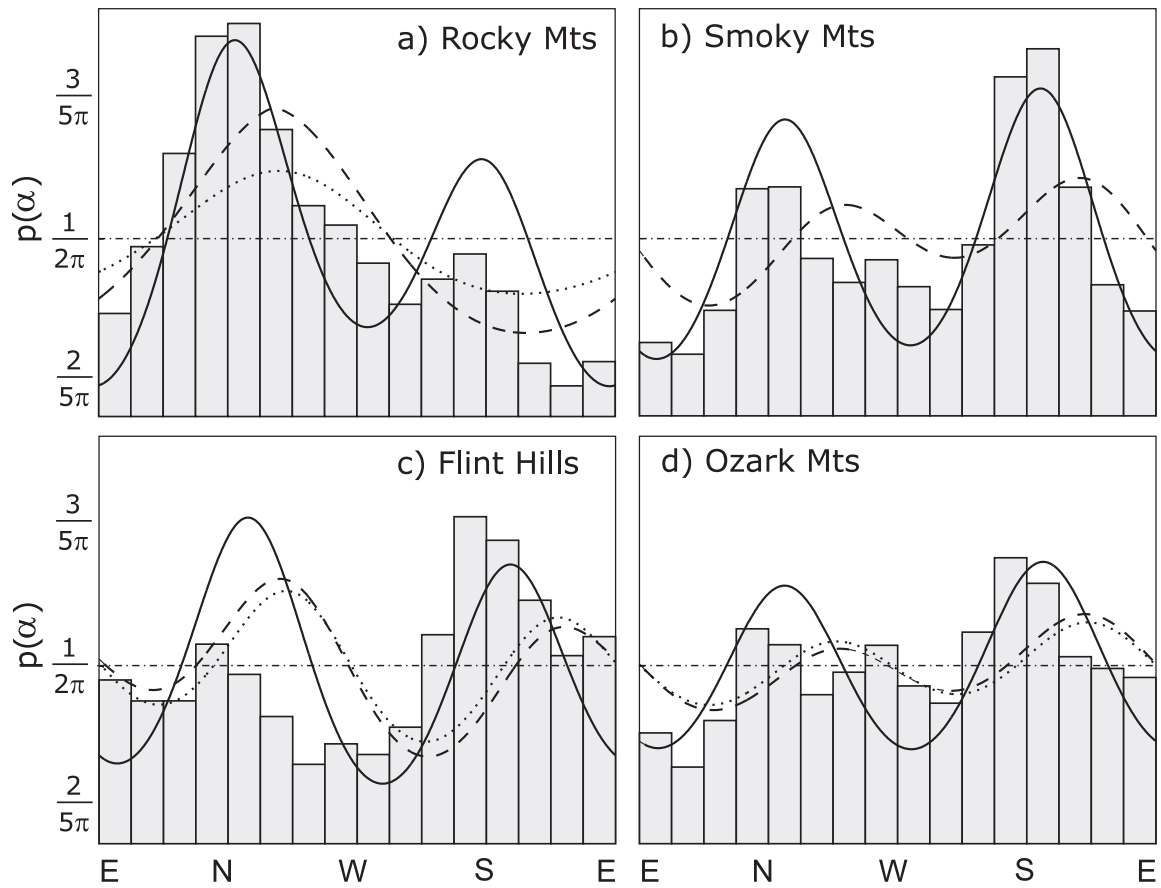


**Figure 5.5:** Comparison with data of derived aspect pdf's including trend and correlation between first derivatives. Lines as in Figure 5.4.

In Figure 5.5 the obtained theoretical pdf's are compared to the observations. In the Flint Hills and Ozark Mountains the aspect distribution is rather uniform, as a consequence of their small trends and frequent valley dissections and tributaries (Oviatt 1998). This is particularly evident in the Ozark Mountains, where short valleys are separated by relatively low ridges and the river network is quite complex (Figure 5.1, bottom right). Conversely, the existence of preferential aspects is apparent in south-

western Colorado and in the Smoky Mountains, where trends are more marked (Table 5.1) and valleys are longer and more preferentially oriented (Figure 5.1, upper row). Note, however, that in all case studies, observed distributions of aspects are quite close to uniform, as also apparent from the computed relative entropy values (Table 5.1). When compared to the observed aspect fields, the theoretical pdf obtained assuming Gaussian partial derivatives best describes the observed aspects. This occurs also in those case studies where the assumption of Gaussian partial derivatives did not perform well. In fact, Laplace and Pearson derivative distributions do not account for the anisotropy of the partial derivative fields, while  $p_\alpha(\alpha)$  is strongly affected by it (Figure 5.2a). This fact explains at least partially the relatively poor fitting of the pdf's of aspect obtained assuming Laplace- and Pearson-distributed partial derivatives. The theoretical pdf's perform reasonably well in the case of Ozark Mountains and Smoky Mountains. In contrast, in the Flint Hills and Rocky Mountains, the theoretical  $p_\alpha(\alpha)$  captures the most frequent aspects, but does not accurately describe their frequency of occurrence. The discrepancies between theoretical pdf's and observed histograms in all case studies is likely associated to nonlocal properties, such as those related to the presence of a river network, not explicitly considered here.

## 5.6 Statistics of solar radiation over the landscape

As an application of the previous results, we explore the impact of topographic features on the instantaneous and daily direct solar radiation, which in turn impacts many ecological and hydrological processes. Most of the variance of the incoming solar radiation is due to variations in direct solar radiation induced by terrain orientation (i.e., slope and aspect; (e.g., Dubayah et al. 1990, Oliphant et al. 2003)). For the sake of simplicity, topographic shadowing, which may be relevant at very low solar elevation (Oliphant et al. 2003, Essery and Marks 2007), is neglected.

The mean and variance of instantaneous solar radiation over the landscape are related to the distribution of slope and aspect, respectively, as

$$\bar{I}(t) = \int_0^{\infty} \int_{-\pi}^{\pi} I_S(t; \tan^{-1} S, \alpha) p_{S,\alpha}(S, \alpha) d\alpha dS, \quad (74)$$

$$\sigma_I^2(t) = \int_0^{\infty} \int_{-\pi}^{\pi} [I_S(t; \tan^{-1} S, \alpha) - \bar{I}(t)]^2 p_{S,\alpha}(S, \alpha) d\alpha dS, \quad (75)$$

where  $I_S(t; \tan^{-1} S, \alpha)$  is the instantaneous direct solar radiation over a sloping surface.

It can be estimated through the illumination angle (i.e., the angle between the solar beam and the normal to the sloping surface),  $i$ , as (Sellers 1965)

$$I_S(t; \tan^{-1} S, \alpha) = I_{hor}(t) \cos i, \quad (76)$$

where  $I_{hor}(t)$  is the direct solar radiation reaching a horizontal surface, a function of the day of the year (DOY), local apparent time ( $t$ ), and total atmospheric transmissivity (here

for simplicity assumed constant), while the illumination angle  $i$  is a function of solar zenith and azimuth, topographic slope and aspect, and local apparent time (Sellers 1965). Eq. (76) must be set to zero when either solar zenith is  $> \pi/2$  or  $\cos i < 0$  (Dingman 1994).

Among the parameters discussed above, the mean instantaneous radiation and its standard deviation over the landscape are mainly affected by the partial derivative standard deviations, while the model chosen to represent partial derivatives, the weak trends and low anisotropy play a secondary role. For this reason, in what follows we assume isotropic field with no trend and Gaussian-distributed derivatives, and focus on the impact of partial derivative standard deviation. Nevertheless, estimated  $\bar{I}(t)$  and  $\sigma_i(t)$  become slightly more sensitive to the model choice when standard deviations of the derivatives are increased above the observed values (not shown). The more pronounced the mode in the derivative model (e.g., Laplace model), the higher  $\bar{I}(t)$  and the lower  $\sigma_i(t)$ ; the differences among the models are more evident under higher solar zeniths.

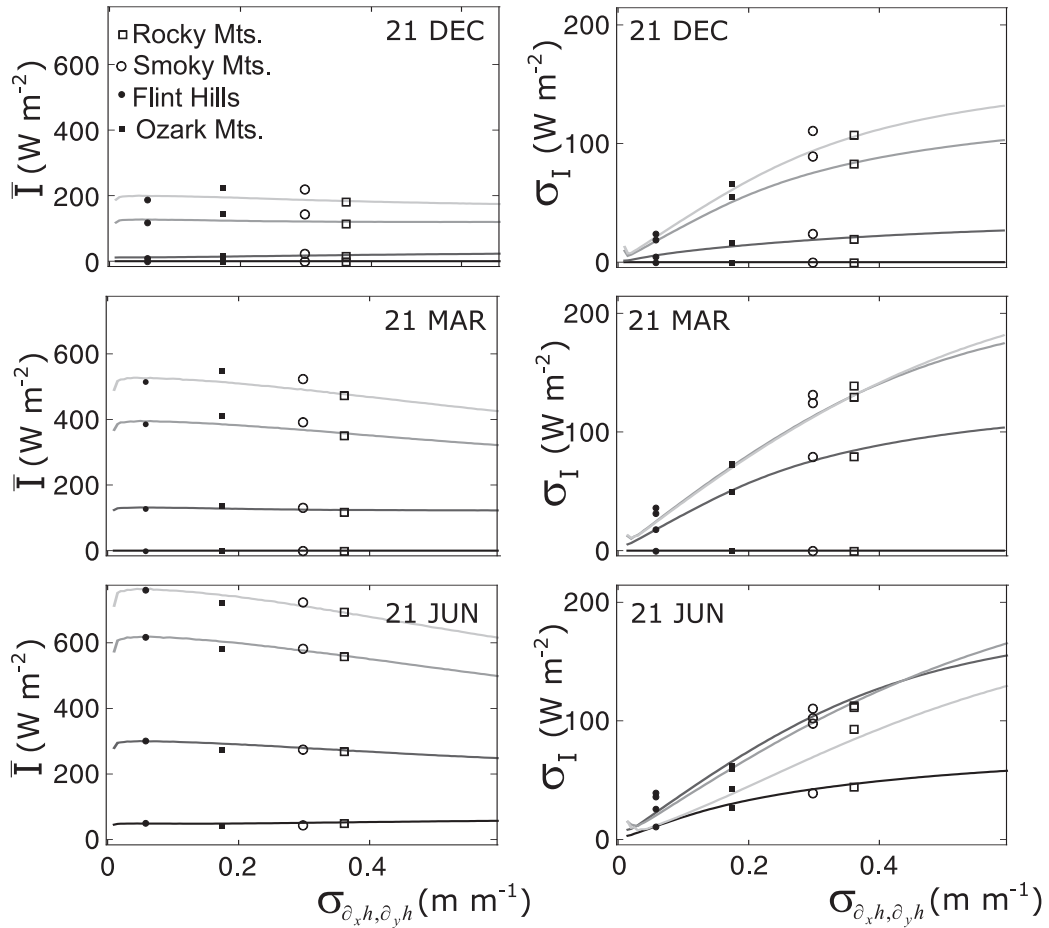


**Figure 5.6:** Mean (left column) and standard deviation (right column) of instantaneous direct solar radiation as a function of the partial-derivative standard deviation,  $\sigma_{\partial_x h, \partial_y h}$  for three days. Modeled quantities (lines) refer to an isotropic landscape with no trend and Gaussian-distributed partial derivatives. Symbols represent direct solar radiation mean and standard deviation, estimated by applying Eq. (76) to each pixel for the four case studies. All lines refer to 38° of latitude N, while the latitude of case studies varies from 35.3 to 39.1° (Figure 5.1). In each plot lines from dark grey to light grey refer to 6 am, 8 am, 10 am, 12 noon local apparent time.

In more detail, in the case of isotropic field of elevation with no trend and Gaussian derivatives, mean direct solar radiation over the landscape is perfectly symmetric with respect to noon, as well as to the spring and fall equinox. Figure 5.6

shows mean and standard deviation of radiation as a function of the standard deviation of the partial derivatives ( $\sigma_{\partial_x h, \partial_y h}$ ) for four times in the morning on the two solstices and the spring equinox at 38° latitude N.  $\bar{I}(t)$  decreases with increasing  $\sigma_{\partial_x h, \partial_y h}$ , while this tendency is reduced moving from noon to earlier in the day and from summer to winter (Figure 5.6, left column). This behavior can be explained by considering that a topography with higher standard deviation will have more frequent steeper areas, which may be very well illuminated when the sun is low on the horizon, thus increasing the overall mean radiation early in the morning. In Figure 5.6, our modeling results (lines) are compared to mean direct solar irradiance estimated by applying Eq. (76) to each DEM pixel and then averaging the results over the whole areas (symbols). The agreement between modeled results and direct estimate of solar irradiance from the DEM is rather good especially for the mean values (Figure 5.6, left column).

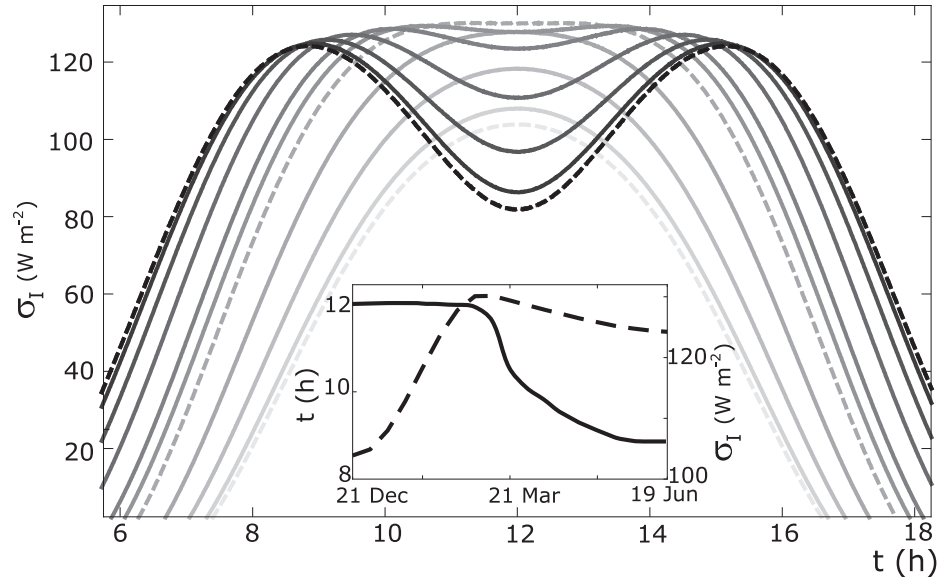


**Figure 5.7:** Daily evolution of solar-irradiance standard deviation: lines (every 20 days) correspond to different days, from the winter solstice (dashed light grey line) through the spring equinox (dashed dark grey line) to the summer solstice (dashed black line). In the inset, maximum daily irradiance standard deviation (dashed line) and time at which such maximum is reached (solid line) as a function of DOY. As in Figure 5.6, the landscape, located at 38°N, is assumed to be isotropic with no trend and Gaussian distributed partial derivatives. The partial derivative standard deviation is set to 0.35 m m<sup>-1</sup>.

The standard deviation of solar radiation increases with increasing  $\sigma_{\partial_x h, \partial_y h}$  (Figure 5.6, right column), reflecting the greater variability of the landscape hillslopes. The magnitude of such an increase depends on both the day of the year and the time of the day: in winter it monotonically increases during the morning, while during the spring it has a maximum before noon. To further investigate this dependence, in Figure 5.7, the daily evolution of the standard deviation of radiation,  $\sigma_I(t)$ , is studied for a given  $\sigma_{\partial_x h, \partial_y h}$  for several days as a function of the local apparent time. Beginning with

the winter solstice (Figure 5.7, light grey dashed line)  $\sigma_I(t)$  increases with solar radiation till the spring equinox (grey dashed line), when it reaches its absolute maximum (Figure 5.7 inset, grey line). In these months the daily maximum of  $\sigma_I(t)$  is achieved at midday (Figure 5.7 inset, solid line), when radiation is also at its maximum. After the spring equinox, as the season proceeds,  $\sigma_I(t)$  starts to decrease, despite the obvious increase in mean solar radiation (Figure 5.6, left column). Furthermore,  $\sigma_I(t)$  now reaches its daily maximum earlier in the morning (and later in the afternoon; Figure 5.7 inset, continuous line). Such a behavior is explained by the fact that the maximum disparity in solar illumination across the topography is achieved at intermediate solar elevations, i.e. around midday in winter and earlier in the days during the springs (see also Essery and Marks 2007). When our model results are compared to the directly calculated solar radiation standard deviations (Figure 5.6, right column), it is apparent that they slightly underestimate the standard deviation, in particular for Smoky Mountains and Flint Hills. Part of such discrepancies may be associated to the simplifying assumptions on the partial derivatives (isotropic field with no trend, and Gaussian-distributed partial derivatives). Moreover, the theoretical curves in Figure 5.6 refer to a single latitude, while, of course, the DEMs of the four case studies cover different latitudes (as clear in Figure 5.1). Nevertheless, further analyses showed that the differences in latitude among case studies are responsible for changes in instantaneous

direct solar radiation mean and variance far smaller than those induced by topography, hour and day of the year.

## **5.7 Conclusions**

We explored the impact of large-scale topographic features (namely, trends and anisotropy) on the probabilistic distribution of slope and aspect. We found that, regardless of the distribution of elevation partial derivatives, the pdf's of topographic slope always exhibit heavier tails than the corresponding marginal distributions of partial derivatives. Moreover, the frequency of occurrence of very low values of slope (i.e., near flat areas) is determined by the behavior of the partial derivative distribution around its mode. Typically observed correlation between derivatives and large-scales trends were found to play a secondary role on the slope distributions. Conversely, aspect distributions are strongly impacted by anisotropy and regional trends, even if weak. Regardless of the specific form of the distributions of the elevation derivatives, an isotropic field with no trend results in a uniform distribution of aspects. The analysis of the simplified case of uniformly distributed derivatives over an elliptical domain allowed us to clearly identify the impact on aspect of the anisotropy, which is responsible for two equally probable modes in opposite directions, and of the trend which gives rise to a single mode. We considered four case studies differing in climate and geomorphology, and compared the observed histograms of partial derivatives, slope and aspect with the theoretical description. We found distributions of partial

derivatives mostly differing in their tail behavior, ranging from Gaussian derivatives for Smoky Mountains to more spiked and heavier-tailed distributions (e.g., Laplace and Pearson type VII) in the Rocky Mountains, Flint Hills and Ozark Mountains. The slope and aspect pdf's were obtained analytically for simplified cases (such as negligible regional trend). Observed slope histograms were reasonably well described by the obtained theoretical pdf's, with the exception of very low slope values, the frequency of which is underestimated by the model. The proposed description of aspect, when the anisotropy is accounted for (i.e., assuming Gaussian-distributed derivatives), was able to capture the position of the aspect modes in all the case studies, but was not adequate to describe other observed details, probably because aspect distribution is driven by nonlocal features (e.g., river network) not accounted for in our parameterizations. Finally, we applied our results to evaluate mean and standard deviation of direct solar radiation over the landscape, showing the key role of elevation derivatives (in particular their variance) and its non-monotonic behavior during the year. The good agreement between calculated and modeled solar radiation showed that the proposed statistical description of slope and aspect may provide a useful and parsimonious tool for ecohydrological and geomorphological applications.

Further analyses on a wider variety of test cases are needed to relate the different geomorphological processes (e.g., tectonic uplift, erosion and deposition, river network incision) as well as their relationships with local geology, climate, and vegetation to the

parameters of our statistical descriptions. Future analyses focusing on the effects of glacial erosion and fluvial deposition will be useful to better capture the observed distribution of partial derivatives at low values, while explicit inclusion of the river network effects will likely improve the statistical description of aspect distributions.

## **6 Towards a spatially-implicit minimalistic model of ecosystem dynamics**

In the first part of this dissertation, the role of water availability on plant dynamics has been described at different level of detail, from sub-daily (Chapter 2) to seasonal and longer time scales (Chapters 3 and 4, and Appendix C). In Chapter 5 a probabilistic description of local topographic features has been presented. In this chapter, these elements are linked together to develop a theoretical framework to analyze the impact of topography on vegetation and nutrient dynamics. To this purpose, the main features of a minimalist model to be interpreted at the year time scale are outlined. The aim is to develop a parsimonious model, able to describe the most relevant interactions among soil moisture, vegetation and nutrient dynamics, including the role of topography through a spatially implicit, probabilistic approach.

### ***6.1 Ecosystem dynamics and the role of topography***

At any point in space, soil moisture, vegetation and nutrient dynamics are inherently coupled (e.g., Jones 1992, Lambers et al. 1998). The main external forcings to ecosystem dynamics are represented by the largely unpredictable rainfall timing and amount, and by solar radiation.

Rainfall timing and amount, in turn, are major drivers of soil water balance, which affects both vegetation and nutrient cycling. At the sub-daily time scale, soil water availability controls vegetation activity, by affecting the leaf water status through the Soil-Plant-Atmosphere continuum (Chapter 2; Daly et al. 2004a). The cumulative effects of vegetation dynamics are apparent at longer time scales, ranging from differences in soil moisture evolution during a single dry-down (Chapter 2) to differences in seasonal crop yield (Chapter 3) and plant primary productivity between subsequent growing seasons (Appendix C; Chapter 4). Also, soil moisture alters rates of nutrient cycling and plant uptake (e.g., Porporato et al. 2003).

Solar radiation is the strongest external driver of canopy and soil energy balance, which in turn affects vegetation assimilation and transpiration rates, as well as soil nutrient cycling. As also described in Chapter 5, available solar radiation depends on local aspect and slope, which directly determine the amount and timing of solar radiation. Nonlocal topographic features may be relevant in rugged landscapes through shadowing effects and changes in diffuse radiation (e.g., Pope and Lloyd 1975, Dubayah et al. 1990, Oliphant et al. 2003). Topographically induced changes in radiation impact vegetation by altering the partition of leaf area in sunlit and shaded leaves (e.g., Wang et al. 2002), as well as instantaneous assimilation rate, vapor pressure, and evapotranspiration (e.g., Barry 1992, Munro and Huang 1997, Essery 2001). The latter

changes, integrated over the growing season, may enhance differences in soil moisture evolutions at the daily time scale and overall seasonal plant primary productivity.

Besides impacting vegetation through solar radiation, topography plays further roles on ecosystem dynamics from sub-daily to geologic times. For example, at sub-daily time scale, solar radiation locally impacts soil temperature. Also, large scale topographic features are partly responsible for the creation of micro-climates and uneven rainfall distribution. Precipitation tends to be more abundant on wind-facing slopes (Barry 1992, Munro and Huang 1997, Essery and Pomeroy 2004), and topography-driven differences in solar radiation input may be further enhanced by patterns in cloudiness induced by orography (Munro and Huang 1997, Turner et al. 1997, Hook and Burke 2000). Topographically induced micro-climate also influences other longer-term aspects of the hydrological cycle, such as snow detention, melting and redistribution, as well as glacier location, predominant direction and evolution (Evans 2006). Integrated over the growing season, such differences may alter the rates of nutrient cycling in the soil, as well as local soil water availability and length of the growing season, thus indirectly impacting vegetation dynamics in a number of ways. At even longer time scales, energy balance is crucial for species distribution and biodiversity both aboveground (Florinsky and Kuryakova 1996, Franklin 1998, Kumar and Skidmore 2000, van der Tol et al. 2007, Bennie et al. 2008) and below ground (e.g., Mahler et al. 1979, Moore et al. 1993, Florinsky et al. 2004). In turn, at geomorphic time scales, vegetation plays a role in

landscape processes, by impacting soil strength to runoff erosion and land-sliding, and channel initiation and hence drainage density (Prosser and Soufi 1998, Istanbuluoglu and Bras 2005).

Finally, landscape processes also control soil features, resulting in spatial patterns of soil depths and texture (Hanna et al. 1982, 1983). In turn, soil physical characteristics play a role in soil moisture dynamics, soil erosion, preferential development of soil crusting (Cerdà 1997, Casanova et al. 2000), root growth and plant water uptake, as well as organic matter accumulation and nutrient availability (Parton et al. 1987). Topographically driven patterns in vegetation, soil moisture and soil temperature directly control the dynamics of soil carbon and nutrient accumulation and redistribution. Depending on plant composition and topographic position, residues of different qualities are produced and mineralized by decomposers, which are highly sensitive to both soil water content and temperature (Brady and Weil 2002, Porporato et al. 2003). As a result, topographically-induced heterogeneities in nutrient cycling and heterotrophic respiration emerge (Pacific et al. 2008).

When spatial connectivity is taken into account, the picture is further complicated. At the landscape level and at the daily time scale the most important spatial interactions for soil-vegetation dynamics are lateral fluxes of water and water-mediated transport of nutrients. Both transport processes are driven by slope, heterogeneities in soil features and soil moisture distribution, and timing of rainfall

events. For example, precipitation may reconnect areas of hillslope otherwise hydrologically unconnected (Grayson et al. 1997, Stieglitz et al. 2003), giving rise to a high degree of spatial organization under wet conditions (Western et al. 1999). Nutrients are transported by water in dissolved form, but also redistributed in the form of plant litter by gravity and wind, and adsorbed to sediments (Rosenbloom et al. 2001, Atkin et al. 2008).

The above described spatial interactions have been modeled either explicitly by using distributed models, or implicitly (e.g., Peters-Lidard et al. 1998, Western et al. 1999). Examples of spatially explicit models including both hydrology and vegetation components are those proposed by Wigmosta et al. (1994), Band et al. (1993) and, recently, Ivanov et al. (2008). In contrast, only a few attempts have been made to describe explicitly spatial heterogeneities of soil carbon and nutrient dynamics at the landscape scale (Rosenbloom et al. 2001). Among spatially implicit models, some forms of terrain indices are often employed, which may be either local (e.g., slope, aspect and curvature) or nonlocal (e.g., specific upslope area, terrain convergence and distance from ridge or river network). The use of local terrain indices may be sufficient when the phenomenon under study is not strongly impacted by spatial interactions with neighboring areas. This is the case of solar radiation estimates (when neglecting nonlocal shadowing effects; Bennie et al. (2008), Chapter 5), or soil moisture distribution when

hydrologic connectivity may be considered less relevant than topographic features (e.g., during dryer periods; see Grayson et al. (1997) and Stieglitz et al. (2003)).

As a first step on the development of a comprehensive theoretical framework to describe ecosystem processes in complex terrain, here a minimalistic, coupled hydrologic-biogeochemical model is presented and future research objectives are outlined.

## **6.2 *Minimalistic model coupling water, nitrogen and vegetation dynamics***

A minimalistic ecosystem model is proposed to describe the coupling of soil moisture, vegetation and nutrient dynamics at a point, at the year time scale. We assume that nitrogen is the most relevant limiting nutrient, as is generally the case in terrestrial ecosystems (Vitousek and Howarth 1991, Brady and Weil 2002). The model is based on mass balances of soil moisture ( $s$ ), carbon and nitrogen in the vegetation compartment ( $C_p$  and  $N_p$ ) and soil organic and inorganic nitrogen ( $N_o$  and  $N_l$ ). Mass balances are then interpreted at steady state conditions. All the variables (except soil moisture) are expressed as carbon or nitrogen mass per unit ground area.

### 6.2.1 Soil water balance

To account for temporal variability of rainfall, we start from the daily soil moisture balance (as detailed in Chapter 3), and compute the long term average soil moisture  $\langle s \rangle$ . Assuming a linear dependence of transpiration on soil moisture and building upon the theoretical results obtained by Porporato et al. (2004), we develop a simplified explicit equation linking average soil moisture to transpiration rate and rainfall features,

$$\langle s \rangle \approx \frac{\beta}{\eta + \beta}, \quad (77)$$

where  $\beta$  depends on rainfall features and  $\eta$  is the normalized transpiration loss. The parameter  $\beta$  is chosen in such a way that the above formulation well describes the results obtained by Porporato et al. (2004). To this purpose, the simplest assumption is

$$\beta = \frac{P}{nZ_r} \text{ (i.e., long term soil moisture average will be a function of total precipitation$$

only, regardless of its average timing). Nevertheless, Appendix C and Chapter 4 clearly show that even at the growing season time scale water input timing may be as relevant to vegetation activity (and hence net growth) as total rainfall amount. Hence, more complex formulations, including the dependence on rainfall mean inter-arrival time and event depth, will also be investigated. We link the normalized transpiration loss  $\eta$

(Chapter 3) to vegetation biomass by using vegetation carbon content, as  $\eta = \frac{ET}{nZ_r} C_P$ ,

where the parameter  $ET$  is the transpiration rate per unit plant carbon mass. In general,  $ET$  depends on leaf nutrient content (which affects water use efficiency; e.g., Wright et al. (2004)), as well as environmental conditions, such as air temperature and humidity, and solar radiation.

### 6.2.2 Vegetation dynamics

Vegetation dynamics may be represented either through a single variable, by considering different species or plant functional types, or by describing vegetation stoichiometry in addition to dry matter dynamics. While more complex models accounting for stoichiometry are preferable for a more physically based coupling of vegetation and nutrient dynamics, more detailed models including allocation and allometric relationships are beyond the scope of the minimalistic model described here. As such, vegetation dynamics is described by two mass balance equations,

$$\begin{aligned} \frac{dC_p}{dt} &= G - LIT \\ \frac{dN_p}{dt} &= UP - LIT_N, \end{aligned} \tag{78}$$

where  $C_p$  and  $N_p$  are carbon and nitrogen masses per unit ground area respectively,  $G$  is plant carbon gross productivity,  $UP$  is nutrient uptake from the soil,  $LIT$  and  $LIT_N$  are plant senescence terms accounting for carbon and nitrogen losses through leaf shedding. In this model, plant C-to-N ratio is assumed to be flexible and determined by the balance of carbon assimilation ( $G$ ) and nutrient uptake ( $UP$ ).

There is strong evidence that CO<sub>2</sub> assimilation and plant growth are related to transpiration, both at the daily (Chapter 2) and the seasonal time scale (see e.g., the relationship between crop yield and total transpiration rate in Figure 4.4). These allow us to introduce a water use efficiency (*WUE*) linking *G* and total transpiration  $ET C_p$ , i.e.

$$G = WUE ET C_p. \quad (79)$$

Furthermore, instantaneous assimilation rate and stomatal conductance are enhanced by leaf nitrogen concentration (Field and Mooney 1986, Schulze et al. 1994, Wright et al. 2004). Hence, plant water use efficiency is assumed to be a function of plant nitrogen concentration, here approximated by the inverse plant C-to-N ratio,  $N_p/C_p$ .

Plant losses of carbon and nitrogen through litterfall clearly depend on the corresponding biomass. Nevertheless, such dependence may depend on vegetation features, such as the allometric structure or the timing of leaf shedding. Also, the plant partially controls nitrogen loss through litterfall, through nitrogen resorption to other plant tissues before leaf shedding (Aerts and Chapin 2000). The effect of a maintenance respiration term, linearly dependent on  $N_p$  (Reich et al. 2006), will also be tested.

### 6.2.3 Soil nutrient dynamics

Two pools of soil nitrogen are considered, representing soil organic and inorganic nitrogen ( $N_o$  and  $N_i$  respectively; see e.g. Manzoni and Porporato, (2007)).

Organic nitrogen mass evolution depends on the balance between plant litter input ( $LIT_N$ ) and nitrogen mineralization ( $MIN$ , a linear function of  $N_o$  at the yearly time scale),

$$\frac{dN_o}{dt} = LIT_N - MIN. \quad (80)$$

Inorganic soil nitrogen is driven by mineralization, wet and dry deposition ( $DEP$ ), plant nitrogen uptake ( $UP$ ) and leaching ( $L$ ), i.e.,

$$\frac{dN_I}{dt} = MIN + DEP - UP - L \quad (81)$$

As a first approximation, plant nitrogen uptake is supposed to be completely driven by transpiration rate, i.e.,  $UP = \frac{N_I}{nZ_r \langle s \rangle} ET C_p$ , where the normalization by  $nZ_r \langle s \rangle$  converts

nitrogen mass per unit ground area to a concentration in liquid phase. Leaching losses mainly depend on water deep infiltration rates, hence it may be assumed that

$L = \frac{N_I}{nZ_r \langle s \rangle} \langle LQ \rangle$ . Since the simplified water balance (Eq. (5)) does not explicitly

distinguish deep infiltration from runoff, such an approximation may overestimate leaching losses, in particular when  $\langle s \rangle$  is relatively high.

### **6.3 Upscaling to the landscape**

The spatial upscaling of soil plant dynamics at the landscape scale is challenging as it requires taking into account topographic heterogeneities. However, it is an essential step to extract useful results at landscape scale from plot-scale experiments and modeling results. In what follows, a possible way to include the main impacts of topography on the above described ecosystem dynamics is outlined. To this purpose, a spatially implicit approach is employed. Such approach may be more suitable than a spatially explicit model when seeking a parsimonious description of the links among topography, water and energy balances, and soil and plant biochemistry.

Neglecting hydrologic connectivity, the previously outlined minimalistic model will be modified to include topographic effects, with *ad hoc* dependences of some crucial parameters on landscape location. As described in Section 6.1, topography influences ecosystem dynamics both directly (e.g., spatial variability in soil features) and indirectly, through the mediation of the solar radiation and surface energy balance.

At the sub-daily time scale, solar radiation influences CO<sub>2</sub> assimilation and transpiration rates (Eq. (89); Farquhar et al. 1980, Jones 1992). It is expected that such dependences also persist at longer time scales, with increasing total production with total intercepted solar radiation (e.g., Monteith 1977): hence, the above formulated model will need to include the impact of solar radiation on both plant growth and total seasonal transpiration. More specifically, given the assumed dependence of plant

growth  $G$  on transpiration, as a first approximation the transpiration per unit carbon biomass,  $ET$ , will be scaled with total solar radiation over the growing season. The proposed formulation is somehow a crude approximation, as at the year time scale vegetation response to available solar radiation may be complicated by plant adaptation strategies and by altered species composition at longer time scales.

Solar irradiance variability across the landscape also controls the surface energy balance at the point. Hence, topographic location impacts average soil and leaf temperature, with higher temperature on south facing slopes where irradiance is maximal. As a consequence, the rate of nutrient cycling and vegetation growth may be affected. Other energy mediated effects of topography (e.g., development of micro-climates and uneven spatial rainfall distribution) will not be considered in this first order analysis.

Landscape position will also affect soil features, namely rooting depth  $Z_r$  and soil porosity  $n$ . It is expected that average rooting depth will be deeper in valley bottoms, and shallower along steep slopes.

Clearly, thanks to the inherent coupling of soil moisture, vegetation and nutrient dynamics, such dependences on topography will have repercussion on soil water and nutrient content. Also, the joint distribution of topographic slope and aspect obtained in Chapter 5 can be used to produce probability distributions and spatial averaged of the

ecosystem variables under scrutiny. Spatially averaged variables may be employed with success in large scale global models.

## 7 Conclusions and future developments

The expected growth in population and the related increase in food, fiber and biofuel demands will enhance the pressure on the already limited freshwater resources. Such pressure may be aggravated by the predicted climate change. For a better management of these scarce resources, a deeper understanding of the responses of ecosystems to anthropogenic pressure and hydroclimatic forcing is warranted and is the overarching motivation of this dissertation. The quantitative models presented in the previous chapters are useful tools to address these issues. By explicitly accounting for environmental variability, quantitative models bridge the gap between experiments often conducted under limited ranges of controlled conditions and the real world, where interaction at multiple temporal and spatial scale are crucial.

In the first part of this dissertation, the hydrologic controls on vegetation dynamics were described by means of a modeling framework accounting for processes at hourly-to-interannual time scales. In the second part, a stochastic approach to include the effects of a complex landscape on ecosystem dynamics was introduced.

In Chapter 2 the effects of water availability on leaf biochemistry were modeled at the hourly time scale. This leaf level model synthesizes the wealth of experimental results available in the literature in a common framework, and allows assessing which the crucial limiting factors for plant activity are. Also, the model provides a more physiological basis to the semi-empirical relationships between soil moisture and daily

plant assimilation and transpiration that are often used in ecohydrological applications and coupled climate-ecosystem models. Moreover, the strong relationships between soil moisture availability and plant water status and activity at daily time scale suggest the need to include hydroclimatic forcing even when aiming at seasonal-time scale descriptions of ecosystem dynamics. Given the inherent unpredictability of this forcing, a stochastic approach is needed.

In Chapter 3 and 4, stochastic soil water balance models were applied to agricultural settings, and analytical dependences of irrigation requirements on soil, crop and climatic characteristics were derived. Such relationships are useful tools for water management and strategic irrigation choices, as they quantify both water requirements and overall profitability. Fine-tuned irrigation schemes such as stress-avoidance micro-irrigation theoretically maximize water productivity, water requirements, and net income. Nevertheless, technical difficulties in precisely tracking soil and plant water status, and soil salinization issues, may render the application of less water conservative irrigation schemes more suitable. For example, demand-driven traditional irrigation that only partially replenishes soil water content is shown to be a reasonable compromise among applicability, water conservation and profitability. The obtained results are further extended by including rainfall interannual variability, which allows retrieving the probability distributions of crop yields, net income and required irrigation volumes. The latter may be used to assess the economic risks inherent in the chosen irrigation

strategy. Also, as discussed in Appendix C, the interactions of daily and interannual hydroclimatic fluctuations exacerbate the occurrence of prolonged droughts and intense storms. A full account of these interactions across temporal scales is necessary for ecosystem productivity predictions under future climate scenarios.

The presented results clarify the relationship between vegetation dynamics and hydrologic forcing at the plot scale. However, these results do not account for the effect of landscape position, which directly influences plants through solar radiation and indirectly through complex feedbacks among soil nutrient, micro-climatic conditions, soil features and vegetation.

As a first step towards an ecosystem model also accounting for spatial heterogeneity, a simple probabilistic description of the main local topographic features (slope and aspect) was presented in Chapter 5. Such probabilistic description allows singling out the role of large-scale landscape structures on the distribution of slope and aspect, and comparing the salient landscape features in relation to their geomorphology. This framework was applied to evaluate solar radiation statistics in different landscapes as a function of landscape roughness. Given the relevant role played by solar radiation on soil moisture, nutrient and vegetation dynamics in a complex terrain, this application is instrumental to extend plot-scale models to the landscape scale.

This work lays a foundation for future research projects considering not only the impact of solar radiation but also the dynamics of the whole ecosystem. As an

alternative to computationally expensive spatially explicit models, a spatially implicit stochastic approach may be chosen. More specifically, to fully link landscape features and ecosystem dynamics, a minimalistic biogeochemical model was outlined in Chapter 6. The parameters controlling the dynamics of the main ecosystem variables at a point will be changed as a function of topographic features, leading to an explicit dependence on landscape position. The developed modeling framework will be used to produce spatial averages of the main ecosystem variables, as well as to single out the most relevant processes at the landscape level. Future research efforts will also investigate the effect of hydrological connectivity, which is not included yet in the minimalistic model.

## Appendix A. CO<sub>2</sub> assimilation model

The assimilation models we use follow with some modifications the parameterizations by Berry and Farquhar (1978) and Farquhar et al. (1980) and their subsequent evolutions (e.g., Collatz et al. 1991, Collatz et al. 1992, Chen et al. 1994, von Caemmerer 2000). The CO<sub>2</sub> assimilation rate is described as the minimum of two potential capacities (Eq. (1)): Rubisco activity ( $A_C$ ), and photosynthetic electron transport, driven by available solar radiation ( $A_J$ ). The finite rate of export or utilization of photosynthesis products may result in a further limitation to photosynthesis (Harley and Sharkey 1991): while some models take into account this third limitation by means of dependences on the maximum activity of Rubisco,  $V_{c,max}$  (Collatz et al. 1991, Foley et al. 1996), it is not considered here (as, e.g., in Farquhar et al. 1980, Leuning 1995, von Caemmerer 2000).

To introduce a gradual, more realistic transition from one limitation to the other, the minimum law in Eq. (1) is often substituted by the lower root of the following quadratic relation (Collatz et al. 1991, Collatz et al. 1992, Foley et al. 1996)

$$\kappa_A A_{gross}^2 - (A_C + A_J) A_{gross} + A_C A_J = 0, \quad (82)$$

where  $\kappa_A$  is the curvature factor.

### CO<sub>2</sub> limitation

Following Farquhar et al. (1980) and von Caemmerer (2000), the Rubisco limited rate of photosynthesis is given by

$$A_c = V_{c,\max} \frac{c - \Gamma^*}{c + K_c \left( 1 + \frac{o}{K_o} \right)}, \quad (83)$$

where  $c$  and  $o$  are the CO<sub>2</sub> and O<sub>2</sub> concentrations at the site of photosynthesis (the mesophyll cell in C<sub>3</sub> species, thus the symbols  $c$  and  $o$  in Eq. (83) will have subscript  $m$ ; the bundle sheath in C<sub>4</sub> species, thus  $c$  and  $o$  in Eq. (83) will have subscript  $bs$ ),  $V_{c,\max}$  is the maximum catalytic activity of Rubisco at current leaf temperature and water status,  $\Gamma^*$  is the equilibrium CO<sub>2</sub> compensation point for gross photosynthesis,  $K_c$  and  $K_o$  are the coefficients for CO<sub>2</sub> and O<sub>2</sub> of the Michelis-Menten kinetics, accounting for the competitive inhibition by O<sub>2</sub>. Some experimental results show a dependence of  $V_{c,\max}$  on leaf water potential, as discussed in the text (see also Figure 2.1a). Moreover, it is well known that the maximum carboxylation rate under well-watered conditions ( $V_{c,\max,ww}$ ), and the parameters of the Michelis-Menten kinetics ( $K_c$  and  $K_o$ ) depend on leaf temperature,  $T_L$ ; we adopt the formulation of Leuning (1995) to express such dependences.

In C<sub>3</sub> leaves, photosynthesis takes place in the mesophyll cell, and the CO<sub>2</sub> concentration there,  $c_m$ , is to be determined through the mesophyll conductance (see text for details). In C<sub>4</sub> leaves, bundle sheath cells are functionally similar to mesophyll cells in

C<sub>3</sub> plants; the CO<sub>2</sub> concentration there,  $c_{bs}$ , represents the equilibrium between the influx,  $V_p$ , driven by the C<sub>4</sub>-cycle, and the sinks, represented by CO<sub>2</sub> assimilation,  $A$ , bundle sheath leakage,  $L_{bs}$ , and mitochondrial respiration,  $R_m$ , i.e.  $V_p = A + L_{bs} + R_m$ . The C<sub>4</sub>-cycle is assumed to be controlled solely by PEP carboxylation rate (Berry and Farquhar 1978), and modelled with a Michelis-Menten type dependence upon CO<sub>2</sub> concentration in the mesophyll and an upper-bound PEP regeneration rate,  $V_{Pr}$  (Chen et al. 1994, von Caemmerer 2000), i.e.

$$V_p = \min\left(\frac{c_m V_{p,\max}}{c_m + K_p}, V_{Pr}\right). \quad (84)$$

As discussed in the text, experimental results show that  $V_{p,\max}$  may be reduced by plant water stress, along with PEP carboxylation rate, hence we assume that  $V_{p,\max}(\psi_L) = V_{p,\max,ww} \eta_p(\psi_L)$ , where  $V_{p,\max,ww}$  stands for  $V_{p,\max}$  rate under well-watered conditions (Figure 2.1b). The diffusion flux of CO<sub>2</sub> between the bundle sheath and the mesophyll,  $L_{bs}$ , is driven by the difference in CO<sub>2</sub> concentration and the conductance between them, i.e.  $L_{bs} = g_{bs} (c_{bs} - c_m)$  (Chen et al. 1994, von Caemmerer 2000). As in C<sub>3</sub> leaves, the CO<sub>2</sub> concentration in the mesophyll cell,  $c_m$ , is a function of mesophyll and stomatal conductances.

For the sake of simplicity, the oxygen concentration at the photosynthetic site ( $o_m$  and  $o_{bs}$  for C<sub>3</sub> and C<sub>4</sub> functional types respectively) is kept constant.

### Light limitation

Despite a high potential rate of RuBp (ribulose-1,5-biphosphate) carboxylation/oxygenation by Rubisco, photosynthesis can be limited by RuBp regeneration rate. The latter is driven by available energy in the form of ATP and NAPDH, supplied by the electron transport rate,  $J$ . Following Leuning (1995), the rate of RuBP-limited CO<sub>2</sub> assimilation is described by

$$A_j = \frac{J}{4} \frac{c - \Gamma^*}{c + 2\Gamma^*}, \quad (85)$$

where  $c$  is the CO<sub>2</sub> concentration at the photosynthetic site ( $c_m$  for C<sub>3</sub> plants,  $c_{bs}$  for C<sub>4</sub> species). The dependence of the electron transport rate  $J$  on absorbed photosynthetically active radiation (PAR) is given by the lower root of the equation (Farquhar and Wong 1984)

$$\kappa_\phi J^2 - (J_\phi + J_{\max})J + J_\phi J_{\max} = 0, \quad (86)$$

where  $\kappa_\phi$  is the curvature factor. Eq. (86) represents the continuous equivalent of the minimum between the limitation to the electron transport rate exerted by adsorbed PAR,  $J_\phi$ , and its maximum potential rate,  $J_{\max}$ , which is assumed to depend only on leaf temperature (as in Leuning 1995). The PAR-dependent electron transport rate,  $J_\phi$ , is here determined after Genty et al. (1989) as

$$J_\phi = \frac{1}{2} \phi_{PSII} \phi_{sw}, \quad (87)$$

where  $\phi_{sw}$  is the PAR absorbed by the leaf, and  $\phi_{PSII}$  is the quantum yield of electron flow through the photosystem II (PSII), which is assumed to be reduced with decreasing leaf water potential (Figure 2.2). Theoretical considerations and experimental measurements (Sharkey et al. 1988, Krall and Edwards 1992, Loreto et al. 1994) show that Eq. (87) correctly estimates the electron transport rate necessary to support the photosynthetic process under relatively low light intensities, while overestimating it under high light intensity. Such possible overestimate is avoided here by using Eq. (86), which limits the calculated electron transport rate,  $J$ , to its maximum potential value,  $J_{\max}$ .

Drawing on the similarities between the C<sub>3</sub>-cycle in C<sub>4</sub> plants and the photosynthesis in C<sub>3</sub> plants, the same model is adopted for C<sub>4</sub> functional type as well. In fact, if the dependence of PEP regeneration on solar radiation is neglected, light availability does not impact the CO<sub>2</sub> concentration mechanism, while it plays a role in the C<sub>3</sub>-cycle. Eq. (85) retains the main features of the formulation proposed by Chen et al. (1994), since it includes the dependence on CO<sub>2</sub> availability, and a saturating dependence on adsorbed photo-irradiance, which is upper-bounded by the potential rate of electron transport (Eq. (86) and (87)). This represents an improvement with respect to the models used by Collatz et al. (1992) and Foley et al. (1996), and has the advantage of allowing the inclusion of the impact of plant water status on light-limited assimilation rate.

## Appendix B. Soil water balance and transpiration flux in the plant

According to the cohesion theory, water moves through the SPAC along a path of decreasing water potential, from the soil (at  $\psi_s$ ), up to the leaves (at  $\psi_L$ ), and to the surrounding atmosphere (at  $\psi_a$ ). The water flux inside the plant,  $E$ , is assumed to be proportional to the water potential gradient through the soil-root-plant system,

$$E = g_{srp} (\psi_s - \psi_L), \quad (88)$$

where soil-root-plant conductance,  $g_{srp}$ , is the series of the soil-root and plant conductance ( $g_{sr}$  and  $g_p$ ). The first one is here described through a simple cylindrical model (Katul et al. 2003), including soil hydraulic conductivity,  $K_s(s)$ , active soil depth,  $Z_r$ , and root area index,  $R_{AI}$ , as

$$g_{sr} = \frac{K_s(s) \sqrt{R_{AI}}}{\pi g \rho_w Z_r}. \quad (89)$$

The hydraulic conductivity is reduced with soil moisture  $s(t)$  as  $K_s(s) = K_{sat} s(t)^{2b+3}$ , where  $b$  is the exponent of the retention curve,  $\psi_s = \bar{\psi}_s s^{-b}$ , linking  $s(t)$  to the soil water potential,  $\psi_s(t)$  (e.g., Laio et al. 2001, Rodriguez-Iturbe and Porporato 2004). To account for root response to declining soil moisture availability (Larcher 1995), root area index is corrected with a simple multiplicative term that attenuates the reduction in  $g_{sr}$  due to the reduced hydraulic conductivity during the dry-

down, as  $R_{AI} = R_{AI,ww} s^{-\omega}$ , where  $R_{AI,ww}$  is the root area index under well watered conditions, and  $\omega$  is a parameter greater than one accounting for root response (Daly et al. 2004a). The reduction of  $g_p$  with declining leaf water potential may be described by the following vulnerability curve (Lambers et al. 1998, Sperry et al. 2002)

$$g_p = g_{p,\max} \exp \left[ - \left( \frac{-\psi_L}{d_c} \right)^{b_c} \right], \quad (90)$$

where  $g_{p,\max}$  is the xylem conductance when no cavitation occurs, while the parameters  $b_c$  and  $d_c$  account for the resistance to cavitation of the plant xylem.  $C_4$  plants from arid and semi-arid ecosystems have lower hydraulic conductivity and less vulnerable vessels (i.e., a safer xylem) than most of  $C_3$  species. On the contrary,  $C_4$  plants adapted to resource-rich areas have parameters similar to those of  $C_3$  plants, but a greater leaf area index,  $L_{AI}$ , which results in a more advantageous water use efficiency (Kocacinar and Sage 2003). Neglecting possible capacitances inside the plant, the transpiration rate at the leaf is equal to the flux in Eq. (88). The lower and upper boundary conditions to the SPAC are set by soil water potential and atmospheric humidity respectively.

The temporal evolution of the soil water potential,  $\psi_s$ , is determined by the soil water balance. In the absence of rain (i.e., during a dry-down), the evolution of the vertically-averaged relative soil moisture,  $s(t)$ , may be expressed by the water balance over the root depth  $Z_r$  (e.g., Laio et al. 2001)

$$nZ_r \frac{ds(t)}{dt} = -E - L, \quad (91)$$

where  $n$  is the soil porosity,  $E$  is the plant transpiration (Eq. (88)), and  $L$  accounts for other losses, such as evaporation from soil and deep infiltration. For simplicity,  $L$  is assumed to follow the behaviour of the hydraulic conductivity  $K_s(s)$ , plus a constant,  $E_v$ , accounting for soil direct evaporation. In some experiments (like those in Figure 2.7), both losses are completely prevented (i.e.,  $L=0$ ).

The upper boundary condition can be set by using the big-leaf scheme and linking the transpiration  $E$  to the specific humidity difference between the stomatal air and the atmospheric bulk air through the leaf conductance,

$$E = g_{sba}(q_L - q_a), \quad (92)$$

where  $g_{sba}$  is the series of stomatal, leaf boundary layer and atmospheric conductance for water vapour per unit ground area ( $g_s$ ,  $g_b$  and  $g_a$  respectively, which relate to the corresponding conductances to  $\text{CO}_2$  as specified in

Table 2.1). Assuming equilibrium between the leaf water potential and the potential of water vapour in the stomatal cavities, one can write

$$q_L \cong \frac{0.622}{P_a} e_{sat}(T_L) \exp\left[\frac{V_w \psi_L}{RT_L}\right], \quad (93)$$

where  $e_{sat}(T_L) \cong a_{sat} \exp[b_{sat}(T_L - 273)(c_{sat} + T_L - 273)^{-1}]$  is the saturated water vapour pressure at leaf temperature  $T_L$  (with  $a_{sat}=613.75$  Pa,  $b_{sat}=17.502$ ,  $c_{sat}=240.97$  K; e.g., Jones, 1992, p. 110),  $R$  is the gas constant,  $V_w$  is the water partial molal volume and  $\rho_a$  is the air density. Leaf temperature  $T_L$  may be obtained from the leaf energy balance, i.e.  $H = c_p \rho_a g_a (T_L - T_a)$ . The sensible heat flux is given by  $H = \phi_{net}(t) - \lambda_w \rho_w E$ , where  $\phi_{net}(t)$  is the net flux of radiation per unit leaf area. In natural environments net solar radiation would be a function of latitude, day of the year, time of the day and atmospheric transmissivity. However, under artificial conditions, incident radiation is generally kept constant during the whole light period, and net radiation may be easily estimated from growing conditions, once the absorption coefficient is known (for our simulation we assumed an absorption coefficient of 0.85; Jones (1992)).

## **Appendix C. Hydroclimatic fluctuations and interannual ecosystem productivity**

This appendix is based on the paper Porporato A., G. Vico and P. A. Fay (2006), Superstatistics of Hydro-Climatic Fluctuations and Interannual Ecosystem Productivity, *Geophysical Research Letters*, vol. 33, L15402, 4<sup>th</sup> August 2006.

Hydro-climatic processes fluctuate on a wide range of time scales. Such fluctuations are often unpredictable from the standpoint of living systems, and adapting to them presents one of the grand challenges for the survival of individuals and for the stability and function of communities and ecosystems. A critical question is how fluctuations in hydro-climatic variables at different time scales change the frequency and intensity of extreme events, and how those changes affect ecosystems. There is a growing consensus that an increase in frequency and intensity of extreme hydro-climatic events will represent one of the most potent features of global climate change, with major possible social and biotic impacts (Easterling et al. 2000, Allen and Ingram 2002, Weltzin et al. 2003). Recent field experiments (Knapp and Smith 2001, Knapp et al. 2002, Gutschick and BassiriRad 2003) and modeling analysis (Porporato et al. 2004) have shown that extreme hydro-climatic events are capable of generating intense impacts on organisms in water-limited ecosystems.

Understanding the adaptations and responses of organisms and ecosystems to hydro-climatic variability and extremes requires understanding the probabilistic

structure of the critical hydro-climatic drivers. 'Superstatistics' can be applied to explain the qualitative variation in the distribution and extremes of external forcing varying at multiple hierarchical scales (Beck 2001, Beck and Cohen 2003), describing the superposition of 'local', or short time-scale fluctuations, that combine to produce a higher-order overall distribution. The latter may be qualitatively different from the 'local' one, with dramatic repercussions on the statistics of extreme events. In mathematical terms, imagine that the intermittent, non-linear dynamics of a representative state variable,  $z$  (rainfall depth or interarrival time between storms in our case) at short time scales is described by the probability density function (pdf),  $p(z;\rho)$ , where  $\rho$  is a parameter. If  $\rho$  itself is varying so that the external forcing fluctuates at longer time scales,  $z$  is driven to a different/new 'local' equilibrium. When the timescale of variation in  $\rho$  is much larger than the one of  $z$ , the probability distribution function of  $z$  can be obtained as a superposition of temporary equilibria, i.e.,

$$p(z) = \int p(z|\rho) \varphi(\rho) d\rho, \quad (94)$$

where  $p(z|\rho)$  is the conditional probability of  $z$  given  $\rho$ , while  $\varphi(\rho)$  is the distribution of  $\rho$  (Benjamin and Cornell 1970, Beck 2001).

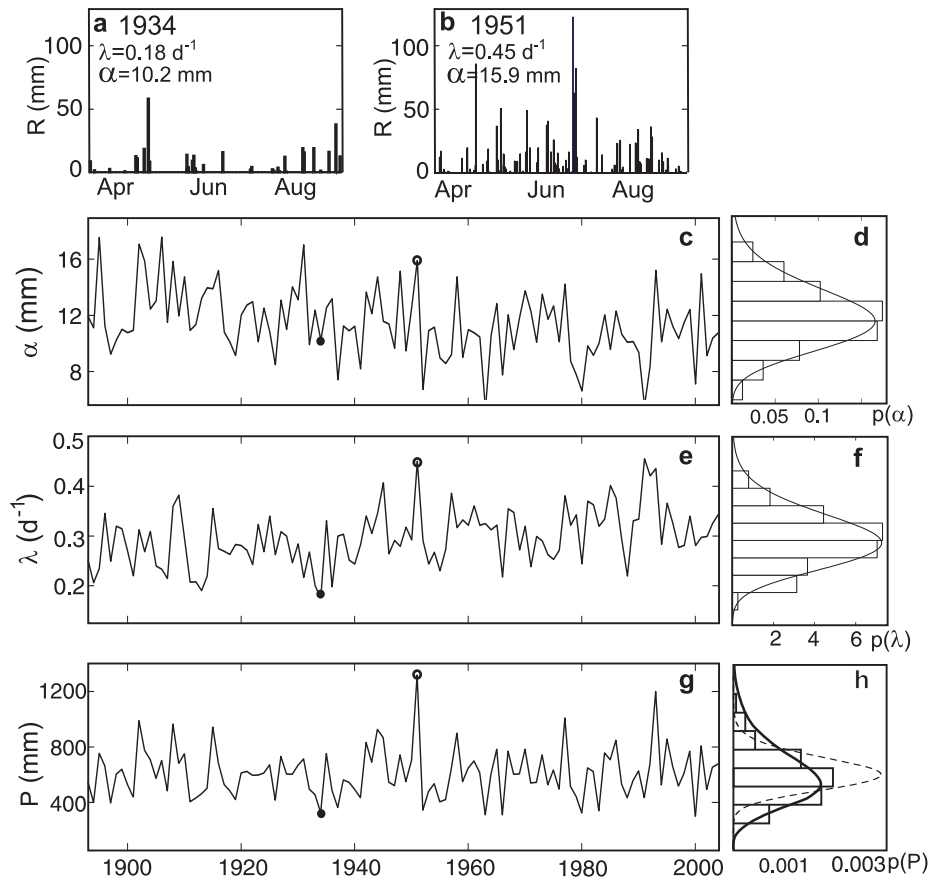


**Figure C.1:** Growing season (April to September) rainfall regime at Manhattan, KS ( $39^{\circ}12' \text{ N}$ ,  $96^{\circ}35' \text{ W}$ ; coop. id. 144972; data available online at [www.ncdc.noaa.gov](http://www.ncdc.noaa.gov)). Daily precipitation during a very dry (a) and a very wet (b) growing season. (c) Time series of mean depth of rainfall events,  $\alpha$  (mean 11.4 mm, standard deviation, s.d., 2.4 mm); (e) mean rate of storm arrival,  $\lambda$  (mean 0.30 1/d, s.d. 0.06 1/d); (g) total rainfall during the growing season,  $P$  (mean 612.4 mm, s.d. 180.3 mm). Frequency distribution and fitted two-parameter gamma distributions of  $\alpha$  (d) and  $\lambda$  (f) (parameters:  $a_{\alpha}=21.8$ ,  $b_{\alpha}=1.90 \text{ 1/mm}$ ;  $a_{\lambda}=27.4$ ,  $b_{\lambda}=91.9 \text{ d}$ ). (h) Frequency distribution of total precipitation,  $P$ , and corresponding theoretical model (solid line); the pdf obtained assuming no interannual variability is also plotted for comparison (dashed line).

Water-limited ecosystems are excellent examples of externally-forced, non-equilibrium systems, and the conceptual framework of superstatistics can be readily

applied to them. In fact, changes in the hydro-climatic regime from growing season to growing season are generally controlled by large-scale circulation patterns that are well known for their interannual and interdecadal variability (Goodin et al. 2003). This is especially true for rainfall, where daily events are a pulsing process with random interarrival times and intensities (e.g., Figure C.1a, b), with distributional statistics exhibiting marked interannual variability (Figure C.1c, e, g). Ecosystems tend to reach equilibrium with the daily forcing within each growing season, while year by year the interannual variability in daily forcing drives ecosystems toward new 'local' equilibria. If the adaptation times of the systems are relatively short, as it is often the case for water-limited ecosystems, their 'global' statistics describing the overall pdf of rainfall result from a superposition of the 'local' equilibria determined by fluctuations in the pdfs of daily rainfall (Eq. (94)).

To proceed quantitatively we use a simple stochastic model of daily rainfall (Laio et al. 2001), that describes the occurrence of rainfall as a compound Poisson process with frequency of events  $\lambda$  (the distribution of times  $\tau$  between precipitation events is thus an exponential with mean  $1/\lambda$ ,  $p_{\tau}(\tau | \lambda) = \lambda \exp(-\lambda \tau)$ ), and exponentially distributed rainfall amounts  $h$  with mean  $\alpha$ ,  $p_h(h | \alpha) = 1/\alpha \exp(-h/\alpha)$ . This model fits the observed daily rainfall data for individual growing seasons quite well. However, when applied to all years combined, the model underestimates rainfall variability, based on the comparison of measured total precipitation with the one modeled including only daily fluctuations

(Figure C.1h). The strong interannual variability in the mean rainfall frequency and event depth ( $\lambda$  and  $\alpha$ , respectively) is even more evident in Figure C.1c, e. Formally, interannual variability could be defined as the changes in the year-by-year statistics that cannot simply be explained as the result of different realizations of the same stochastic process describing intra-annual fluctuations. Interannual fluctuations in rainfall depth and frequency can be assumed to be independent; a good model for such interannual fluctuations (Figure C.1 f) (D'Odorico et al. 2000) is a two-parameter gamma distribution

$$g_x(x) = \frac{b_x^{a_x}}{\Gamma(a_x)} x^{a_x-1} e^{-b_x x}, \quad (95)$$

where  $x$  stands for either  $\alpha$  or  $\lambda$ ,  $b_x$  is the scale parameter, and  $a_x$  is the shape parameter of the distribution.

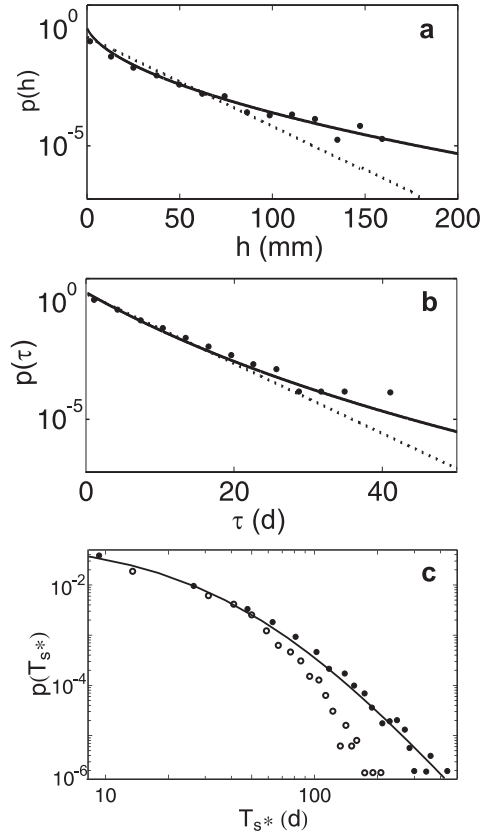


**Figure C.2:** Pdf of rainfall depths (a), and interarrival times (b), obtained as superstatistics of daily and interannual variability (continuous lines); comparison with the exponential pdf corresponding to no interannual variability (dotted lines), and observed frequency distributions at Manhattan, KS (closed symbols). (c) Pdf of the duration of periods of plant water stress at Manhattan, KS: Monte Carlo simulation (closed symbols); fitted Pareto distribution (continuous line); pdf obtained with no interannual variability (open symbols). The parameters of the stochastic soil moisture model (Laio et al. 2001) are: soil type is silty loam ( $n=0.47$ ,  $s_l=0.14$ ,  $s_w=0.16$ ,  $s^*=0.35$ ,  $s_f=0.59$ ,  $K_s=33$  cm/d,  $b=5$ ,  $E_w=0.01$  cm/d) and maximum vegetation transpiration is  $E_{max}=0.45$  cm/d.

The superstatistics of rainfall depth and interval between storms can be obtained analytically by means of Eq. (94), using the exponential distributions for daily

fluctuations conditional on the parameter values, the distribution of which is described by Eq. (95). Accordingly, the pdf of rainfall depth  $h$  can be shown to be

$$p(h) = \frac{2b_h^{(a_h+1)/2}}{\Gamma(a_h)} h^{(a_h-1)/2} K_{1-a_h} \left[ 2\sqrt{b_h h} \right], \quad (96)$$

where  $K_n$  is the Bessel function of order  $n^{\text{th}}$  (Abramowitz and Stegun 1965). The tail of this pdf is similar to that of a stretched exponential distribution (Sornette 2003) and therefore intermediate between a power-law (e.g., scaling behavior) and an exponential one. Interannual variability thus increases the frequency of extreme rainfall event depths with respect to the model including only daily variability. The obtained pdf (Eq. (96)) well describes the observed rainfall patterns, while the exponential distribution proves to be inadequate to statistically characterize extreme storm depths of all the years combined (Figure C.2a). Similarly, the pdf of the intervals between storms,  $\tau$ , including interannual variability, can be obtained as

$$p(\tau) = \frac{a_\tau b_\tau^{a_\tau}}{(\tau + b_\tau)^{a_\tau+1}}, \quad (97)$$

which, interestingly, is a Pareto distribution with scale parameter  $b_\tau/a_\tau$  and shape parameter  $-1/a_\tau$  (Laherrere and Sornette 1998). Data from different sites in the USA show a wide range of values for  $a_\tau$ , always well above 2 (i.e., the distribution is not Lèvy stable (Sornette 2003)). The power-law tail implies more frequent extreme events with significant implications for the return time of drought periods, and thus repercussions for vegetation water stress, river streamflows, and water resource availability.

Correct modeling of the hierarchical variation in rainfall frequency and depth is crucial for improving predictions of important attributes of water limited ecosystems. It has already been shown how interannual variability in rainfall can cause bimodal probability distributions of mean soil moisture (Ridolfi et al. 2000, D'Odorico and Porporato 2004). The distribution of soil moisture affects the distribution of plant water status which in turn directly impacts ecosystem function. In particular, rainfall daily and interannual fluctuations can be related to the duration  $T_{s^*}$  of periods in which soil moisture is below a threshold  $s^*$ , marking the onset of water stress. Figure C.2c shows the probability distribution of  $T_{s^*}$  resulting from Monte Carlo simulations, using the stochastic soil moisture model (Laio et al. 2001) with and without the inclusion of interannual variability. The distribution of  $T_{s^*}$  with interannual variability is well described by a Pareto distribution (solid line in Figure C.2c), the power-law behavior of which implies a higher frequency of long periods of plant water stress, resulting in reduced plant carbon assimilation and net primary productivity (Porporato et al. 2001).

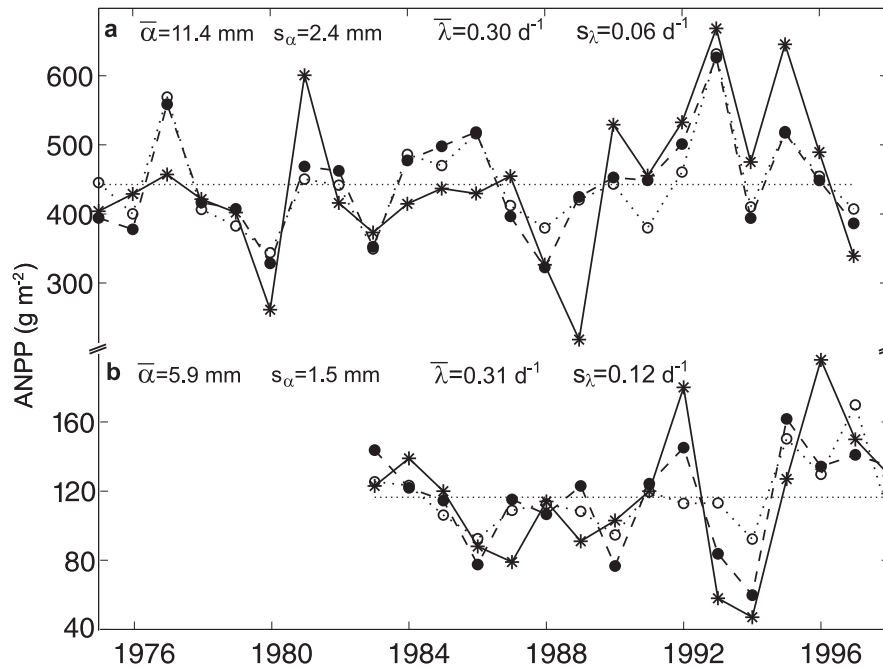


**Figure C.3:** Time series of ANPP (stars) and estimated ANPP at KNZ LTER site, KS (a), and SGS LTER site, CO (b). Estimated ANPP is obtained with a multiple regression model using only the total rainfall over the growing season,  $P$  (open symbols), and including also the mean event depth,  $\alpha$ , and the mean interval between rainfall events,  $1/\lambda$  (close symbols). At KNZ the linear regression using the total precipitation resulted in  $r^2=0.40$  ( $237+0.30P+\xi$ ;  $\sigma_\xi=85$  g/m<sup>2</sup>), while the multiple linear regression improved  $r^2$  up to 0.47 ( $437-6.2\alpha-41\lambda^{-1}+0.32P+\xi$ ;  $\sigma_\xi=84$  g/m<sup>2</sup>). At SGS the linear regression with  $P$  yielded  $r^2=0.27$  ( $40+0.27P+\xi$ ;  $\sigma_\xi=35$  g/m<sup>2</sup>), while the multiple linear regression gave  $r^2=0.53$  ( $173+28\alpha-40\lambda^{-1}-0.29P+\xi$ ;  $\sigma_\xi=31$  g/m<sup>2</sup>). The random deviation from the linear regression,  $\xi$ , is practically Gaussian distributed, with zero mean and standard deviation  $\sigma_\xi$ . At both sites, the growing season is assumed to last from the beginning of April to the end of September. Annual ANPP data collected at KNZ and SGS LTER sites are available online at <http://intranet.lternet.edu/cgi-bin/anpp.pl> (PI: A.K. Knapp and M.D. Smith) (Knapp and Smith 2001). Note that in order to obtain meaningful statistics for KNZ we used rainfall records from Manhattan, KS, located approximately 12 km north of the LTER site. Daily rainfall records for SGS LTER site are available on line at <http://sgs.cnr.colostate.edu>.

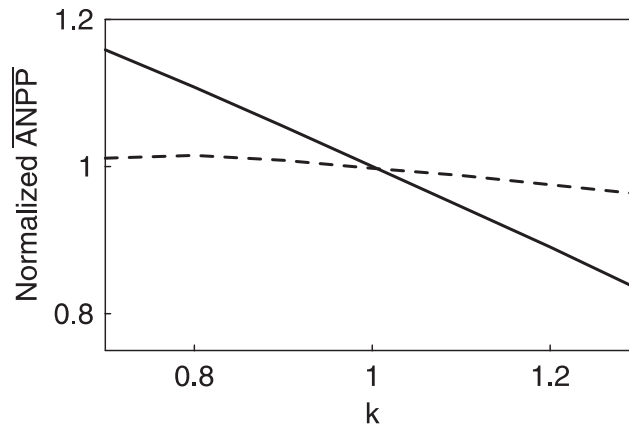


**Figure C.4:** Normalized mean ANPP under different rainfall scenarios corresponding to changes in interannual variability for constant mean rainfall totals, at KNZ (continuous line) and at SGS (dashed line). The hypothetical rainfall scenarios are generated such that the means of  $\alpha$  and  $\lambda$ ,  $\bar{\alpha}$  and  $\bar{\lambda}$ , are modified in opposite ways in order to keep the mean total precipitation constant,  $\bar{P} = \bar{\alpha} \bar{\lambda}$ . Thus values of the parameter  $k = \bar{\alpha}_{projected} / \bar{\alpha}_{current}$  higher than one correspond to increased mean intensity and reduced mean frequency of rainfall events, and vice versa for  $k < 1$ . The ANPP is obtained by means of the multiple regression models of Figure C.3 that employ the annual mean depth of rainfall events  $\alpha$ , the annual mean rainfall frequency  $\lambda$ , and the cumulative precipitation during the growing season  $P$ .

We illustrate these implications by examining two grassland ecosystems with different degree of water limitation, for which long series of aboveground net primary productivity (ANPP) are available: the shortgrass steppe, represented by the Shortgrass Steppe Long-Term Ecological Research (LTER) site (SGS) in northern Colorado, and the tallgrass prairie, represented by the Konza Prairie LTER site (KNZ) in eastern Kansas. ANPP at these sites is significantly correlated with interannual variability in total growing season rainfall ( $r^2=0.40$  and  $r^2=0.27$  for KNZ and SGS resp.; Figure C.3). The inclusion of mean frequency and intensity of rainfall along with total annual rainfall in a

multiple linear regression improves the ANPP prediction, especially for the semi-arid shortgrass steppe site ( $r^2=0.47$  and  $r^2=0.53$  for KNZ and SGS resp.). Climate models predict less frequent precipitation occurrence, but larger rainfall input per event due to more intense convective storms (Easterling et al. 2000). We explored the consequences of such changes via Monte Carlo simulations by predicting ANPP using the multiple regression of Figure C.3 and changing the parameters in the probability distributions of interannual variability (i.e., the two-parameter gamma distribution of Eq. (95)) while keeping the mean total precipitation constant. As shown in Figure C.4, the results predict a low impact of changes in rainfall patterns on ANPP at SGS, as opposed to a marked decrease in mean ANPP at KNZ. The latter finding agrees with results from a 4-year rainfall manipulation experiment (Knapp et al. 2002): however, the results of the regressive model cannot be directly compared to experimental data, due to the short duration of the experiment, which only provides a limited characterization of the link between interannual rainfall variability and ANPP. The diverging results between the two sites can be explained by the difference in total precipitation, which reflects a difference in mean storm depth ( $\bar{\alpha}$  for KNZ is twice that of SGS), rather than a difference in mean rate of storm arrival. As a consequence, at KNZ an increase in mean storm depth would likely result in increasing losses due to runoff and deep drainage combined with longer return intervals with greater soil moisture depletion, resulting in decreased net primary productivity, while at SGS more intense rainfall is likely to be

more effectively used by the vegetation. The fact that the current vegetation at SGS is more adapted to water stress, as opposed to the more mesic KNZ prairie, could further enhance the differences in ecosystem response.

In summary, we have shown that interannual variability of plant productivity is substantially explained by interannual patterns of rainfall total amount, frequency and storm depth. These patterns arise from superstatistics of rainfall at different time scales, which can lead to more likely extreme events in terms of intensity of storms and duration of droughts. Under different rainfall scenarios, our multiple regression model for ANPP as a function of rainfall patterns predicts a decrease of plant productivity, when event depth and interval among storms increase. This is particularly evident in mesic grasslands, where rainfall partitioning and plant water stress tend to be very sensitive to changes in timing and amount of rainfall, and clearly shows that the impact of interannual variability and climate change will be different depending on the type of water limitation of each ecosystem.

## References

- Abramowitz, M., and I. A. Stegun. 1965. Handbook of mathematical functions. Dover, New York.
- Aerts, R., and F. S. Chapin. 2000. The mineral nutrition of wild plants revisited: A re-evaluation of processes and patterns. Pages 1-67 *in* Advances in Ecological Research, Vol 30. Academic Press Inc, San Diego.
- Allen, M. R., and W. J. Ingram. 2002. Constraints on future changes in climate and the hydrologic cycle. *Nature* **419**:224-232.
- Amthor, J. S. 1994. Scaling CO<sub>2</sub>-photosynthesis relationships from the leaf to the canopy. *Photosynthesis Research* **39**:321-350.
- Ancey, C., M. Meunier, and D. Richard. 2003. Inverse problem in avalanche dynamics models. *Water Resources Research* **39**.
- Atkin, O. K., L. J. Atkinson, R. A. Fisher, C. D. Campbell, J. Zaragoza-Castells, J. W. Pitchford, F. I. Woodward, and V. Hurry. 2008. Using temperature-dependent changes in leaf scaling relationships to quantitatively account for thermal acclimation of respiration in a coupled global climate-vegetation model. *Global Change Biology* **14**:2709-2726.
- Band, L. E., P. Patterson, R. Nemani, and S. W. Running. 1993. Forest ecosystem processes at the watershed scale - Incorporating hillslope hydrology. *Agricultural and Forest Meteorology* **63**:93-126.
- Barabasi, A.-L., and H. E. Stanley. 1995. Fractal concepts in surface growth. Cambridge University Press, Cambridge.
- Barry, R. G. 1992. Mountain climatology and past and potential future climatic changes in mountain regions - A review. *Mountain Research and Development* **12**:71-86.
- Beck, C. 2001. Dynamical foundations of nonextensive statistical mechanics. *Physical Review Letters* **87**.
- Beck, C., and E. G. D. Cohen. 2003. Superstatistics. *Physica A-Statistical Mechanics and Its Applications* **322**:267-275.

- Benjamin, J. R., and C. A. Cornell. 1970. Probability, statistics and decision for civil engineers. *in*. McGraw Hill, New York.
- Bennie, J., B. Huntley, A. Wiltshire, M. O. Hill, and R. Baxter. 2008. Slope, aspect and climate: spatially explicit and implicit models of topographic microclimate in chalk grassland. *Ecological Modelling* **216**:47-59.
- Berry, J. A., and G. D. Farquhar. 1978. The CO<sub>2</sub> concentrating function of C<sub>4</sub> photosynthesis: a biochemical model. Pages 119-131 *in* D. Hall, J. Coombs, and T. Goodwin, editors. 4th International Congress on Photosynthesis. Biochemical Society, London.
- Brady, N. C., and R. R. Weil. 2002. The nature and properties of soils, 13th edition. Prentice Hall, Upper Saddle River, New Jersey.
- Bras, R. L., and J. R. Cordova. 1981. Intraseasonal water allocation in deficit irrigation. *Water Resources Research* **17**:866-874.
- Bras, R. L., and D. J. Seo. 1987. Irrigation control in the presence of salinity - Extended linear quadratic approach. *Water Resources Research* **23**:1153-1161.
- Buckley, T. N. 2005. The control of stomata by water balance. *New Phytologist* **168**:275-291.
- Buckley, T. N., K. A. Mott, and G. D. Farquhar. 2003. A hydromechanical and biochemical model of stomatal conductance. *Plant Cell and Environment* **26**:1767-1785.
- Burbank, D. W. 1992. Geomorphology - Characteristic size of relief. *Nature* **359**:483-484.
- Casanova, M., I. Messing, and A. Joel. 2000. Influence of aspect and slope gradient on hydraulic conductivity measured by tension infiltrometer. *Hydrological Processes* **14**:155-164.
- Centritto, M., F. Loreto, and K. Chartzoulakis. 2003. The use of low [CO<sub>2</sub>] to estimate diffusional and non-diffusional limitations of photosynthetic capacity of salt-stressed olive saplings. *Plant Cell and Environment* **26**:585-594.
- Cerdà, A. 1997. Seasonal changes of the infiltration rates in a Mediterranean scrubland on limestone. *Journal of Hydrology* **198**:209-225.

- Chalmers, D. J., P. D. Mitchell, and L. Vanheek. 1981. Control of peach-tree growth and productivity by regulated water-supply, tree density, and summer pruning. *Journal of the American Society for Horticultural Science* **106**:307-312.
- Chaves, M. M. 1991. Effects of water deficits on Carbon assimilation. *Journal of Experimental Botany* **42**:1-16.
- Chen, D.-X., M. B. Coughenour, A. K. Knapp, and C. E. Owensby. 1994. Mathematical simulation of C<sub>4</sub> grass photosynthesis in ambient and elevated CO<sub>2</sub>. *Ecological Modelling* **73**:63-80.
- Collatz, G. J., J. T. Ball, C. Grivet, and J. A. Berry. 1991. Physiological and environmental-regulation of stomatal conductance, photosynthesis and transpiration - A model that includes a laminar boundary-layer. *Agricultural and Forest Meteorology* **54**:107-136.
- Collatz, G. J., J. A. Berry, and J. S. Clark. 1998. Effects of climate and atmospheric CO<sub>2</sub> partial pressure on the global distribution of C-4 grasses: present, past, and future. *Oecologia* **114**:441-454.
- Collatz, G. J., M. Ribas-Carbo, and J. A. Berry. 1992. Coupled photosynthesis-stomatal conductance model for leaves of C<sub>4</sub> plants. *Australian Journal of Plant Physiology* **19**:519-538.
- ContourAnsel, D., G. Ilami, A. Ouarzane, and P. Louguet. 1996. Effect of water stress on pyruvate, P-i dikinase and phosphoenol pyruvate carboxylase activities in the leaves of two cultivars of sorghum (*Sorghum bicolor* L). *Journal of Agronomy and Crop Science-Zeitschrift Fur Acker Und Pflanzenbau* **176**:59-69.
- Cornic, G. 2000. Drought stress inhibits photosynthesis by decreasing stomatal aperture - not by affecting ATP synthesis. *Trends in Plant Science* **5**:187-188.
- Cover, T. M., and J. A. Thomas. 1991. *Elements of information theory*. John Wiley and Sons, New York.
- D'Odorico, P., and A. Porporato. 2004. Preferential states in soil moisture and climate dynamics. *Proceedings of the National Academy of Sciences of the United States of America* **101**:8848-8851.
- D'Odorico, P., L. Ridolfi, A. Porporato, and I. Rodriguez-Iturbe. 2000. Preferential states of seasonal soil moisture: The impact of climate fluctuations. *Water Resources Research* **36**:2209-2219.

- Daly, E., A. C. Oishi, A. Porporato, and G. G. Katul. 2008. A stochastic model for daily subsurface CO<sub>2</sub> concentration and related soil respiration. *Advances in Water Resources* **31**:987-994.
- Daly, E., and A. Porporato. 2006a. Probabilistic dynamics of some jump-diffusion systems. *Physical Review E* **73**.
- Daly, E., and A. Porporato. 2006b. State-dependent fire models and related renewal processes. *Physical Review E* **74**.
- Daly, E., A. Porporato, and I. Rodriguez-Iturbe. 2004a. Coupled dynamics of photosynthesis, transpiration, and soil water balance. Part I: Upscaling from hourly to daily level. *Journal of Hydrometeorology* **5**:546-558.
- Daly, E., A. Porporato, and I. Rodriguez-Iturbe. 2004b. Coupled dynamics of photosynthesis, transpiration, and soil water balance. Part II: Stochastic analysis and ecohydrological significance. *Journal of Hydrometeorology* **5**:559-566.
- Dewar, R. C. 2002. The Ball-Berry-Leuning and Tardieu-Davies stomatal models: synthesis and extension within a spatially aggregated picture of guard cell function. *Plant Cell and Environment* **25**:1383-1398.
- Diaz-Espejo, A., A. S. Walcroft, J. E. Fernandez, B. Hafidi, M. J. Palomo, and I. F. Giron. 2006. Modeling photosynthesis in olive leaves under drought conditions. *Tree Physiology* **26**:1445-1456.
- Dingman, S. L. 1994. *Physical hydrology*. Prentice-Hall, London.
- Dodds, P. S., and D. H. Rothman. 2000. Scaling, universality, and geomorphology. *Annual Review of Earth and Planetary Sciences* **28**:571-610.
- Du, Y. C., Y. Kawamitsu, A. Nose, S. Hiyane, S. Murayama, K. Wasano, and Y. Uchida. 1996. Effects of water stress on carbon exchange rate and activities of photosynthetic enzymes in leaves of sugarcane (*Saccharum* sp). *Australian Journal of Plant Physiology* **23**:719-726.
- Dubayah, R., J. Dozier, and F. W. Davis. 1990. Topographic distribution of clear-sky radiation over the Konza Prairie, Kansas. *Water Resources Research* **26**:679-690.
- Dubois, J. J. B., E. L. Fiscus, F. L. Booker, M. D. Flowers, and C. D. Reid. 2007. Optimizing the statistical estimation of the parameters of the Farquhar-von Caemmerer-Berry model of photosynthesis. *New Phytologist* **176**:402-414.

- Easterling, D. R., G. A. Meehl, C. Parmesan, S. A. Changnon, T. R. Karl, and L. O. Mearns. 2000. Climate extremes: Observations, modeling, and impacts. *Science* **289**:2068-2074.
- Ehleringer, J., and R. W. Pearcy. 1983. Variation in quantum yield for CO<sub>2</sub> uptake among C-3 and C-4 plants. *Plant Physiology* **73**:555-559.
- English, M. 1990. Deficit irrigation 1. Analytical framework. *Journal of Irrigation and Drainage Engineering-Asce* **116**:399-412.
- English, M. J. 1981. The uncertainty of crop models in irrigation optimization. *Transactions of the ASAE* **24**:917-921,928.
- English, M. J., K. H. Solomon, and G. J. Hoffman. 2002. A paradigm shift in irrigation management. *Journal of Irrigation and Drainage Engineering-Asce* **128**:267-277.
- Essery, R. 2001. Spatial statistics of windflow and blowing-snow fluxes over complex topography. *Boundary-Layer Meteorology* **100**:131-147.
- Essery, R., and D. Marks. 2007. Scaling and parametrization of clear-sky solar radiation over complex topography. *Journal of Geophysical Research-Atmospheres* **112**.
- Essery, R., and J. Pomeroy. 2004. Vegetation and topographic control of wind-blown snow distributions in distributed and aggregated simulations for an Arctic tundra basin. *Journal of Hydrometeorology* **5**:735-744.
- Ethier, G. J., and N. J. Livingston. 2004. On the need to incorporate sensitivity to CO<sub>2</sub> transfer conductance into the Farquhar-von Caemmerer-Berry leaf photosynthesis model. *Plant Cell and Environment* **27**:137-153.
- Evans, I. S. 2006. Glacier distribution in the Alps: Statistical modelling of altitude and aspect. *Geografiska Annaler Series a-Physical Geography* **88A**:115-133.
- FAO. 2002. World agriculture: towards 2015/2030. Summary Report Food and Agriculture Organization of the United Nations, Rome.
- Farquhar, G. D., S. von Caemmerer, and J. A. Berry. 1980. A biochemical-model of photosynthetic CO<sub>2</sub> assimilation in leaves of C-3 species. *Planta* **149**:78-90.
- Farquhar, G. D., and S. C. Wong. 1984. An empirical model of stomatal conductance. *Australian Journal of Plant Physiology* **11**:191-209.

- Federer, C. A. 1982. Transpirational supply and demand - Plant, soil, and atmospheric effects evaluated by simulation. *Water Resources Research* **18**:355-362.
- Fereres, E., and M. A. Soriano. 2007. Deficit irrigation for reducing agricultural water use. *Journal of Experimental Botany* **58**:147-159.
- Field, C., and H. A. Mooney. 1986. The photosynthesis - nitrogen relationship in wild plants. *in* T. J. Givnish, editor. *On the economy of plant form and function*. Cambridge University Press, Cambridge.
- Flexas, J., J. Bota, J. Cifre, J. M. Escalona, J. Galmes, J. Gulias, E. K. Lefi, S. F. Martinez-Canellas, M. T. Moreno, M. Ribas-Carbo, D. Riera, B. Sampol, and H. Medrano. 2004a. Understanding down-regulation of photosynthesis under water stress: future prospects and searching for physiological tools for irrigation management. *Annals of Applied Biology* **144**:273-283.
- Flexas, J., J. Bota, J. Galmes, H. Medrano, and M. Ribas-Carbo. 2006a. Keeping a positive carbon balance under adverse conditions: responses of photosynthesis and respiration to water stress. *Physiologia Plantarum* **127**:343-352.
- Flexas, J., J. Bota, F. Loreto, G. Cornic, and T. D. Sharkey. 2004b. Diffusive and metabolic limitations to photosynthesis under drought and salinity in C-3 plants. *Plant Biology* **6**:269-279.
- Flexas, J., and H. Medrano. 2002. Drought-inhibition of photosynthesis in C-3 plants: Stomatal and non-stomatal limitations revisited. *Annals of Botany* **89**:183-189.
- Flexas, J., M. Ribas-Carbo, J. Bota, J. Galmes, M. Henkle, S. Martinez-Canellas, and H. Medrano. 2006b. Decreased Rubisco activity during water stress is not induced by decreased relative water content but related to conditions of low stomatal conductance and chloroplast CO<sub>2</sub> concentration. *New Phytologist* **172**:73-82.
- Florinsky, I. V., and G. A. Kuryakova. 1996. Influence of topography on some vegetation cover properties. *Catena* **27**:123-141.
- Florinsky, I. V., S. McMahon, and D. L. Burton. 2004. Topographic control of soil microbial activity: a case study of denitrifiers. *Geoderma* **119**:33-53.
- Foley, J. A., I. C. Prentice, N. Ramankutty, S. Levis, D. Pollard, S. Sitch, and A. Haxeltine. 1996. An integrated biosphere model of land surface processes, terrestrial carbon balance, and vegetation dynamics. *Global Biogeochemical Cycles* **10**:603-628.

- Forkutsa, I., R. Sommer, Y. I. Shirokova, J. P. A. Lamers, K. Kienzler, B. Tischbein, C. Martius, and P. L. G. Vlek. 2009. Modeling irrigated cotton with shallow groundwater in the Aral Sea Basin of Uzbekistan: II. Soil salinity dynamics. *Irrigation Science* **27**:319-330.
- Franklin, J. 1998. Predicting the distribution of shrub species in southern California from climate and terrain-derived variables. *Journal of Vegetation Science* **9**:733-748.
- Gagnon, J. S., S. Lovejoy, and D. Schertzer. 2006. Multifractal Earth topography. *Nonlinear Processes in Geophysics* **13**:541-570.
- Galmes, J., H. Medrano, and J. Flexas. 2006. Acclimation of Rubisco specificity factor to drought in tobacco: discrepancies between in vitro and in vivo estimations. *Journal of Experimental Botany* **57**:3659-3667.
- Galmes, J., H. Medrano, and J. Flexas. 2007. Photosynthetic limitations in response to water stress and recovery in Mediterranean plants with different growth forms. *New Phytologist* **175**:81-93.
- Gao, Q., P. Zhao, X. Zeng, X. Cai, and W. Shen. 2002. A model of stomatal conductance to quantify the relationship between leaf transpiration, microclimate and soil water stress. *Plant Cell and Environment* **25**:1373-1381.
- Gardiner, G. W. 1990. *Handbook of stochastic methods for physics, chemistry and the natural sciences*, 2nd edition. Springer, Berlin.
- Geerts, S., and D. Raes. 2009. Deficit irrigation as an on-farm strategy to maximize crop water productivity in dry areas. *Agricultural Water Management* **96**:1275-1284.
- Genty, B., J. M. Briantais, and N. R. Baker. 1989. The relationship between the quantum yield of photosynthetic electron-transport and quenching of chlorophyll fluorescence. *Biochimica Et Biophysica Acta* **990**:87-92.
- Georgiou, P. E., and D. M. Papamichail. 2008. Optimization model of an irrigation reservoir for water allocation and crop planning under various weather conditions. *Irrigation Science* **26**:487-504.
- Ghannoum, O., J. P. Conroy, S. P. Driscoll, M. J. Paul, C. H. Foyer, and D. W. Lawlor. 2003. Nonstomatal limitations are responsible for drought-induced photosynthetic inhibition in four C-4 grasses. *New Phytologist* **159**:599-608.

- Gimenez, C., V. J. Mitchell, and D. W. Lawlor. 1992. Regulation of photosynthetic rate of two sunflower hybrids under water-stress. *Plant Physiology* **98**:516-524.
- Gleick, P. H. 2003. Water use. *Annual Review of Environment and Resources* **28**:275-314.
- Goodin, D. G., P. A. Fay, and M. J. McHugh. 2003. Climate variability in tallgrass prairie at multiple time scales: Konza Prairie Biological Station. Pages 411-424 *in* D. Greenland, D. G. Goodin, and R. C. Smith, editors. *Climate variability and ecosystem response at Long-Term Ecological Research sites*. Oxford University Press, New York.
- Grassi, G., and F. Magnani. 2005. Stomatal, mesophyll conductance and biochemical limitations to photosynthesis as affected by drought and leaf ontogeny in ash and oak trees. *Plant Cell and Environment* **28**:834-849.
- Grayson, R. B., A. W. Western, F. H. S. Chiew, and G. Bloschl. 1997. Preferred states in spatial soil moisture patterns: Local and nonlocal controls. *Water Resources Research* **33**:2897-2908.
- Griffiths, H., and M. A. J. Parry. 2002. Plant responses to water stress - Preface. *Annals of Botany* **89**:801-802.
- Groisman, P. Y., T. R. Karl, D. R. Easterling, R. W. Knight, P. F. Jamason, K. J. Hennessy, R. Suppiah, C. M. Page, J. Wibig, K. Fortuniak, V. N. Razuvaev, A. Douglas, E. Forland, and P. M. Zhai. 1999. Changes in the probability of heavy precipitation: Important indicators of climatic change. *Climatic Change* **42**:243-283.
- Gutschick, V. P., and H. BassiriRad. 2003. Extreme events as shaping physiology, ecology, and evolution of plants: toward a unified definition and evaluation of their consequences. *New Phytologist* **160**:21-42.
- Halpin-Healy, T., and Y. C. Zhang. 1995. Kinetic roughening phenomena, stochastic growth directed polymers and all that - Aspects of multidisciplinary statistical-mechanics. *Physics Reports-Review Section of Physics Letters* **254**:215-415.
- Hanna, A. Y., P. W. Harlan, and D. T. Lewis. 1982. Soil available water as influenced by landscape position and aspect. *Agronomy Journal* **74**:999-1004.
- Hanna, A. Y., P. W. Harlan, and D. T. Lewis. 1983. Effect of landscape position and aspect on soil-water recharge. *Agronomy Journal* **75**:57-60.

- Hanson, A. D., and W. D. Hitz. 1982. Metabolic responses of mesophytes to plant water deficits. *Annual Review of Plant Physiology and Plant Molecular Biology* **33**:163-203.
- Harley, P. C., and T. D. Sharkey. 1991. An improved model of C<sub>3</sub> photosynthesis at high CO<sub>2</sub> - Reversed O<sub>2</sub> sensitivity explained by lack of glycerate reentry into the chloroplast. *Photosynthesis Research* **27**:169-178.
- Hillel, D. 2004. *Introduction to environmental soil physics*. Elsevier Academic Press, Amsterdam.
- Hook, P. B., and I. C. Burke. 2000. Biogeochemistry in a shortgrass landscape: Control by topography, soil texture, and microclimate. *Ecology* **81**:2686-2703.
- Hsiao, T. C. 1973. Plant responses to water stress. *Annual Review of Plant Physiology and Plant Molecular Biology* **24**:519-570.
- Igbadun, H. E., A. Tarimo, B. A. Salim, and H. F. Mahoo. 2007. Evaluation of selected crop water production functions for an irrigated maize crop. *Agricultural Water Management* **94**:1-10.
- Istanbulluoglu, E., and R. L. Bras. 2005. Vegetation-modulated landscape evolution: Effects of vegetation on landscape processes, drainage density, and topography. *Journal of Geophysical Research-Earth Surface* **110**.
- Ivanov, V. Y., R. L. Bras, and E. R. Vivoni. 2008. Vegetation-hydrology dynamics in complex terrain of semiarid areas: 1. A mechanistic approach to modeling dynamic feedbacks. *Water Resources Research* **44**.
- Jarvis, P. G. 1976. The interpretation of the variations in leaf water potential and stomatal conductance found in canopies in the field. *Philosophical Transactions of the Royal Society of London - Series B* **273**:593-610.
- Jones, H. G. 1992. *Plants and microclimate: a quantitative approach to environmental plant physiology*, 2nd edition. Cambridge University Press, Cambridge.
- Jones, H. G. 2004. Irrigation scheduling: advantages and pitfalls of plant-based methods. *Journal of Experimental Botany* **55**:2427-2436.
- Jury, W. A., and H. J. Vaux. 2007. The emerging global water crisis: Managing scarcity and conflict between water users. *Advances in Agronomy* **95**:1-76.

- Kaiser, W. M. 1987. Effects of water deficit on photosynthetic capacity. *Physiologia Plantarum* **71**:142-149.
- Kalapos, T., R. vandenBoogaard, and H. Lambers. 1996. Effect of soil drying on growth, biomass allocation and leaf gas exchange of two annual grass species. *Plant and Soil* **185**:137-149.
- Kang, S. Z., L. Zhang, Y. L. Liang, X. T. Hu, H. J. Cai, and B. J. Gu. 2002. Effects of limited irrigation on yield and water use efficiency of winter wheat in the Loess Plateau of China. *Agricultural Water Management* **55**:203-216.
- Karam, F., R. Kabalan, J. Breidi, Y. Roupael, and T. Oweis. 2009. Yield and water-production functions of two durum wheat cultivars grown under different irrigation and nitrogen regimes. *Agricultural Water Management* **96**:603-615.
- Karl, T. R., J. M. Melillo, and T. C. Peterson, editors. 2009. *Global climate change impacts in the United States*. Cambridge University Press, Cambridge, MA.
- Katul, G., R. Leuning, and R. Oren. 2003. Relationship between plant hydraulic and biochemical properties derived from a steady-state coupled water and carbon transport model. *Plant Cell and Environment* **26**:339-350.
- Knapp, A. K., P. A. Fay, J. M. Blair, S. L. Collins, M. D. Smith, J. D. Carlisle, C. W. Harper, B. T. Danner, M. S. Lett, and J. K. McCarron. 2002. Rainfall variability, carbon cycling, and plant species diversity in a mesic grassland. *Science* **298**:2202-2205.
- Knapp, A. K., and M. D. Smith. 2001. Variation among biomes in temporal dynamics of aboveground primary production. *Science* **291**:481-484.
- Kocacinar, F., and R. F. Sage. 2003. Photosynthetic pathway alters xylem structure and hydraulic function in herbaceous plants. *Plant Cell and Environment* **26**:2015-2026.
- Kottegoda, N. T., and Rosso. 1998. *Statistics, probability and reliability for civil and environmental engineers*. McGraw-Hill, New York.
- Krall, J. P., and G. E. Edwards. 1992. Relationship between photosystem-II activity and CO<sub>2</sub> fixation in leaves. *Physiologia Plantarum* **86**:180-187.
- Krug, J. 1997. Origins of scale invariance in growth processes. *Advances in Physics* **46**:139-282.

- Kumar, L., and A. K. Skidmore. 2000. Radiation-vegetation relationships in a Eucalyptus forest. *Photogrammetric Engineering and Remote Sensing* **66**:193-204.
- Laherrere, J., and D. Sornette. 1998. Stretched exponential distributions in nature and economy: "fat tails" with characteristic scales. *European Physical Journal B* **2**:525-539.
- Laio, F., A. Porporato, L. Ridolfi, and I. Rodriguez-Iturbe. 2001. Plants in water-controlled ecosystems: active role in hydrologic processes and response to water stress - II. Probabilistic soil moisture dynamics. *Advances in Water Resources* **24**:707-723.
- Lal, A., and G. E. Edwards. 1996. Analysis of inhibition of photosynthesis under water stress in the C-4 species *Amaranthus cruentus* and *Zea mays*: Electron transport, CO<sub>2</sub> fixation and carboxylation capacity. *Australian Journal of Plant Physiology* **23**:403-412.
- Lal, A., M. S. B. Ku, and G. E. Edwards. 1996. Analysis of inhibition of photosynthesis due to water stress in the C-3 species *Hordeum vulgare* and *Vicia faba*: Electron transport, CO<sub>2</sub> fixation and carboxylation capacity. *Photosynthesis Research* **49**:57-69.
- Lambers, H., F. S. Chapin, and T. L. Pons. 1998. *Plant physiological ecology*. Springer, New York.
- Larcher, W. 1995. *Physiological plant ecology*, 3rd edition. Springer, Berlin.
- Lauenroth, W. K., and O. E. Sala. 1992. Long-term forage production of North-American Shortgrass Steppe. *Ecological Applications* **2**:397-403.
- Lawlor, D. W. 1995. The effects of water deficit on photosynthesis. Pages 129-160 *in* N. Smirnoff, editor. *Environment and plant metabolism: flexibility and acclimation*. BIOS Scientific, Oxford.
- Lawlor, D. W. 2002. Limitation to photosynthesis in water-stressed leaves: Stomata vs. metabolism and the role of ATP. *Annals of Botany* **89**:871-885.
- Lawlor, D. W., and G. Cornic. 2002. Photosynthetic carbon assimilation and associated metabolism in relation to water deficits in higher plants. *Plant Cell and Environment* **25**:275-294.

- Leuning, R. 1995. A critical-appraisal of a combined stomatal-photosynthesis model for C-3 plants. *Plant Cell and Environment* **18**:339-355.
- Longuet-Higgins, M. S. 1957. Statistical properties of an isotropic random surface. *Philosophical Transactions of the Royal Society of London - Series A* **250**:157-174.
- Loreto, F., G. Dimarco, D. Tricoli, and T. D. Sharkey. 1994. Measurements of mesophyll conductance, photosynthetic electron-transport and alternative electron sinks of field-grown wheat leaves. *Photosynthesis Research* **41**:397-403.
- Lu, C. M., and J. H. Zhang. 1998. Effects of water stress on photosynthesis, chlorophyll fluorescence and photoinhibition in wheat plants. *Australian Journal of Plant Physiology* **25**:883-892.
- Lu, C. M., and J. H. Zhang. 1999. Effects of water stress on photosystem II photochemistry and its thermostability in wheat plants. *Journal of Experimental Botany* **50**:1199-1206.
- Luo, Y. H. 1991. Changes of Ci/Ca in association with stomatal and nonstomatal limitation to photosynthesis in water stressed *Abutilon-Theophrasti*. *Photosynthetica* **25**:273-279.
- Maggioni, M., and U. Gruber. 2003. The influence of topographic parameters on avalanche release dimension and frequency. *Cold Regions Science and Technology* **37**:407-419.
- Mahler, R. L., D. F. Bezdicek, and R. E. Witters. 1979. Influence of slope position on nitrogen-fixation and yield of dry peas. *Agronomy Journal* **71**:348-351.
- Manzoni, S., and A. Porporato. 2007. A theoretical analysis of nonlinearities and feedbacks in soil carbon and nitrogen cycles. *Soil Biology & Biochemistry* **39**:1542-1556.
- Massacci, A., A. Battistelli, and F. Loreto. 1996. Effect of drought stress on photosynthetic characteristics, growth and sugar accumulation of field-grown sweet sorghum. *Australian Journal of Plant Physiology* **23**:331-340.
- McCaig, T. N. 1997. Temperature and precipitation effects on durum wheat grown in southern Saskatchewan for fifty years. *Canadian Journal of Plant Science* **77**:215-223.

- McGraw, D. K., and J. F. Wagner. 1968. Elliptically symmetric distributions. *Ieee Transactions on Information Theory* **IT14**:110-120.
- Milly, P. C. D. 2001. A minimalist probabilistic description of root zone soil water. *Water Resources Research* **37**:457-463.
- Monteith, J. L. 1977. Climate and efficiency of crop production in Britain. *Philosophical Transactions of the Royal Society of London Series B-Biological Sciences* **281**:277-294.
- Montgomery, D. R. 2001. Slope distributions, threshold hillslopes, and steady-state topography. *American Journal of Science* **301**:432-454.
- Moore, I. D., P. E. Gessler, G. A. Nielsen, and G. A. Peterson. 1993. Soil attribute prediction using terrain analysis. *Soil Science Society of America Journal* **57**:443-452.
- Morgan, J. A., D. R. LeCain, J. J. Read, H. W. Hunt, and W. G. Knight. 1998. Photosynthetic pathway and ontogeny affect water relations and the impact of CO<sub>2</sub> on *Bouteloua gracilis* (C-4) and *Pascopyrum smithii* (C-3). *Oecologia* **114**:483-493.
- Morison, J. I. L., and R. M. Gifford. 1984. Plant-growth and water-use with limited water-supply in high CO<sub>2</sub> concentrations .1. Leaf-area, water-use and transpiration. *Australian Journal of Plant Physiology* **11**:361-374.
- Munro, D. S., and L. J. Huang. 1997. Rainfall, evaporation and runoff responses to hillslope aspect in the Shenchong Basin. *Catena* **29**:131-144.
- Musick, J. T., O. R. Jones, B. A. Stewart, and D. A. Dusek. 1994. Water-yield relationships for irrigated and dryland wheat in the US southern plains. *Agronomy Journal* **86**:980-986.
- Nilsen, E. T., and D. M. Orcutt. 1998. *Physiology of plant under stress: abiotic factors*. John Wiley and Sons, New York.
- Norman, J. M. 1982. Simulation of microclimates. Pages 65-99 *in* J. L. Hatfield and I. Thompson, editors. *Biometeorology and integrated pest management*. Academic Press, New York.

- O'Toole, J. C., R. K. Crookston, K. J. Treharne, and J. L. Ozbun. 1976. Mesophyll resistance and carboxylase activity - Comparison under water stress conditions. *Plant Physiology* **57**:465-468.
- Oliphant, A. J., R. A. Spronken-Smith, A. P. Sturman, and I. F. Owens. 2003. Spatial variability of surface radiation fluxes in mountainous terrain. *Journal of Applied Meteorology* **42**:113-128.
- Oviatt, C. G. 1998. Geomorphology of Konza Prairie. Pages 35-47 in A. K. Knapp, J. M. Briggs, D. C. Hartnett, and S. L. Collins, editors. *Grassland dynamics: Long-term ecological research in tallgrass prairie*. Oxford University Press, New York.
- Oweis, T., and A. Hachum. 2009. Optimizing supplemental irrigation: Tradeoffs between profitability and sustainability. *Agricultural Water Management* **96**:511-516.
- Pachepsky, Y. A., D. J. Timlin, and W. J. Rawls. 2001. Soil water retention as related to topographic variables. *Soil Science Society of America Journal* **65**:1787-1795.
- Pacific, V., B. McGlynn, D. Riveros-Iregui, D. Welsch, and H. Epstein. 2008. Variability in soil respiration across riparian-hillslope transitions. *Biogeochemistry* **91**:51-70.
- Pankovic, D., Z. Sakac, S. Kevresan, and M. Plesnicar. 1999. Acclimation to long-term water deficit in the leaves of two sunflower hybrids: photosynthesis, electron transport and carbon metabolism. *Journal of Experimental Botany* **50**:127-138.
- Parry, M. A. J., P. J. Andralojc, S. Khan, P. J. Lea, and A. J. Keys. 2002. Rubisco activity: Effects of drought stress. *Annals of Botany* **89**:833-839.
- Parton, W. J., D. S. Schimel, C. V. Cole, and D. S. Ojima. 1987. Analysis of factors controlling soil organic-matter levels in Great-Plains Grasslands. *Soil Science Society of America Journal* **51**:1173-1179.
- Payero, J. O., S. R. Melvin, S. Irmak, and D. Tarkalson. 2006. Yield response of corn to deficit irrigation in a semiarid climate. *Agricultural Water Management* **84**:101-112.
- Pearcy, R. W., and J. Ehleringer. 1984. Comparative ecophysiology of C-3 and C-4 plants. *Plant Cell and Environment* **7**:1-13.

- Peters-Lidard, C. D., E. Blackburn, X. Liang, and E. F. Wood. 1998. The effect of soil thermal conductivity parameterization on surface energy fluxes and temperatures. *Journal of the Atmospheric Sciences* **55**:1209-1224.
- Polley, H. W., J. M. Norman, T. J. Arkebauer, E. A. Waltershea, D. H. Greigor, and B. Bramer. 1992. Leaf gas-exchange of *Andropogon-Gerardii* Vitman, *Panicum-Virgatum* L, and *Sorghastrum-Nutans* (L) Nash in a tallgrass prairie. *Journal of Geophysical Research-Atmospheres* **97**:18837-18844.
- Pope, D. J., and P. S. Lloyd. 1975. Hemispherical photography, topography and plant distribution. Pages 385-408 *in* G. C. Evans, R. Bainbridge, and O. Rackham, editors. *Light as an ecological factor II* Blackwell Scientific Publications, Oxford.
- Porporato, A., P. D'Odorico, F. Laio, and I. Rodriguez-Iturbe. 2003. Hydrologic controls on soil carbon and nitrogen cycles. I. Modeling scheme. *Advances in Water Resources* **26**:45-58.
- Porporato, A., E. Daly, and I. Rodriguez-Iturbe. 2004. Soil water balance and ecosystem response to climate change. *American Naturalist* **164**:625-632.
- Porporato, A., F. Laio, L. Ridolfi, and I. Rodriguez-Iturbe. 2001. Plants in water-controlled ecosystems: active role in hydrologic processes and response to water stress - III. Vegetation water stress. *Advances in Water Resources* **24**:725-744.
- Porporato, A., G. Vico, and P. A. Fay. 2006. Superstatistics of hydro-climatic fluctuations and interannual ecosystem productivity. *Geophysical Research Letters* **33**.
- Prosser, I. P., and M. Soufi. 1998. Controls on gully formation following forest clearing in a humid temperate environment. *Water Resources Research* **34**:3661-3671.
- Protopapas, A. L., and A. P. Georgakakos. 1990. An optimal-control method for real-time irrigation scheduling. *Water Resources Research* **26**:647-669.
- Reich, P. B., M. G. Tjoelker, J. L. Machado, and J. Oleksyn. 2006. Universal scaling of respiratory metabolism, size and nitrogen in plants. *Nature* **439**:457-461.
- Ridolfi, L., P. D'Odorico, A. Porporato, and I. Rodriguez-Iturbe. 2000. Impact of climate variability on the vegetation water stress. *Journal of Geophysical Research-Atmospheres* **105**:18013-18025.
- Ridolfi, L., P. D'Odorico, A. Porporato, and I. Rodriguez-Iturbe. 2003. Stochastic soil moisture dynamics along a hillslope. *Journal of Hydrology* **272**:264-275.

- Rigby, J. R., and A. Porporato. 2006. Simplified stochastic soil-moisture models: a look at infiltration. *Hydrology and Earth System Sciences* **10**:861-871.
- Rinaldo, A., I. Rodriguez-Iturbe, and R. Rigon. 1998. Channel networks. *Annual Review of Earth and Planetary Sciences* **26**:289-327.
- Robertson, G. W. 1974. Wheat yields for 50 years at Swift Current, Saskatchewan in relation to weather. *Canadian Journal of Plant Science* **54**:625-650.
- Rodriguez-Iturbe, I., and A. Porporato. 2004. *Ecohydrology of water-controlled ecosystems - Soil moisture and plant dynamics*. Cambridge University Press, Cambridge.
- Rodriguez-Iturbe, I., A. Porporato, L. Ridolfi, V. Isham, and D. R. Cox. 1999. Probabilistic modelling of water balance at a point: the role of climate, soil and vegetation. *Proceedings of the Royal Society of London Series A-Mathematical Physical and Engineering Sciences* **455**:3789-3805.
- Rodriguez-Iturbe, I., and A. Rinaldo. 1997. *Fractal river basins: Chance and self-organization*. Cambridge University Press, Cambridge.
- Rogers, A., D. S. Ellsworth, and S. W. Humphries. 2001. Possible explanation of the disparity between the in vitro and in vivo measurements of Rubisco activity: a study in loblolly pine grown in elevated pCO<sub>2</sub>. *Journal of Experimental Botany* **52**:1555-1561.
- Rosenbloom, N. A., S. C. Doney, and D. S. Schimel. 2001. Geomorphic evolution of soil texture and organic matter in eroding landscapes. *Global Biogeochemical Cycles* **15**:365-381.
- Sage, R. F., and D. S. Kubien. 2003. Quo vadis C-4? An ecophysiological perspective on global change and the future of C<sub>4</sub> plants. *Photosynthesis Research* **77**:209-225.
- Sage, R. F., D. A. Wedin, and M. Li. 1999. The biogeography of C<sub>4</sub> photosynthesis: patterns and controlling factors. Pages 597 *in* R. F. Sage and R. K. Monson, editors. *C<sub>4</sub> plant biology*. Academic Press, San Diego.
- Schoups, G., J. W. Hopmans, C. A. Young, J. A. Vrugt, W. W. Wallender, K. K. Tanji, and S. Panday. 2005. Sustainability of irrigated agriculture in the San Joaquin Valley, California. *Proceedings of the National Academy of Sciences of the United States of America* **102**:15352-15356.

- Schulze, E. D., F. M. Kelliher, C. Korner, J. Lloyd, and R. Leuning. 1994. Relationships among maximum stomatal conductance, ecosystem surface conductance, carbon assimilation rate, and plant nitrogen nutrition - A global ecology scaling exercise. *Annual Review of Ecology and Systematics* **25**:629-662.
- Sellers, P. J., D. A. Randall, G. J. Collatz, J. A. Berry, C. B. Field, D. A. Dazlich, C. Zhang, G. D. Collelo, and L. Bounoua. 1996. A revised land surface parameterization (SiB2) for atmospheric GCMs .1. Model formulation. *Journal of Climate* **9**:676-705.
- Sellers, W. D. 1965. *Physical climatology*. The University of Chicago Press, Chicago.
- Seneweera, S., O. Ghannoum, and J. P. Conroy. 2001. Root and shoot factors contribute to the effect of drought on photosynthesis and growth of the C-4 grass *Panicum coloratum* at elevated CO<sub>2</sub> partial pressures. *Australian Journal of Plant Physiology* **28**:451-460.
- Sepaskhah, A. R., and D. Akbari. 2005. Deficit irrigation planning under variable seasonal rainfall. *Biosystems Engineering* **92**:97-106.
- Sepaskhah, A. R., A. Azizian, and A. R. Tavakoli. 2006. Optimal applied water and nitrogen for winter wheat under variable seasonal rainfall and planning scenarios for consequent crops in a semi-arid region. *Agricultural Water Management* **84**:113-122.
- Sharkey, T. D., J. A. Berry, and R. F. Sage. 1988. Regulation of photosynthetic electron-transport in *Phaseolus-Vulgaris* L, as determined by room-temperature Chlorophyll a Fluorescence. *Planta* **176**:415-424.
- Shi, B., B. Vidakovic, G. G. Katul, and J. D. Albertson. 2005. Assessing the effects of atmospheric stability on the fine structure of surface layer turbulence using local and global multiscale approaches. *Physics of Fluids* **17**.
- Siddique, M. R. B., A. Hamid, and M. S. Islam. 2000. Drought stress effects on water relations of wheat. *Botanical Bulletin of Academia Sinica* **41**:35-39.
- Sornette, D. 2003. *Critical phenomena in natural sciences*, 2nd edition. Springer, New York.
- Sornette, D., and Y. C. Zhang. 1993. Nonlinear Langevin model of geomorphic erosion processes. *Geophysical Journal International* **113**:382-386.

- Speight, J. G. 1971. Log-normality of slope distribution. *Zeitschrift für Geomorphologie* **15**:290-311.
- Sperry, J. S., U. G. Hacke, R. Oren, and J. P. Comstock. 2002. Water deficits and hydraulic limits to leaf water supply. *Plant Cell and Environment* **25**:251-263.
- Stieglitz, M., J. Shaman, J. McNamara, V. Engel, J. Shanley, and G. W. Kling. 2003. An approach to understanding hydrologic connectivity on the hillslope and the implications for nutrient transport. *Global Biogeochemical Cycles* **17**.
- Sun, H. Y., C. M. Liu, X. Y. Zhang, Y. J. Shen, and Y. Q. Zhang. 2006. Effects of irrigation on water balance, yield and WUE of winter wheat in the North China Plain. *Agricultural Water Management* **85**:211-218.
- Tardieu, F., and W. J. Davies. 1993. Integration of hydraulic and chemical signaling in the control of stomatal conductance and water status of droughted plants. *Plant Cell and Environment* **16**:341-349.
- Tardieu, F., and T. Simonneau. 1998. Variability among species of stomatal control under fluctuating soil water status and evaporative demand: modelling isohydric and anisohydric behaviours. *Journal of Experimental Botany* **49**:419-432.
- Tezara, W., M. D. Fernandez, C. Donoso, and A. Herrera. 1998. Seasonal changes in photosynthesis and stomatal conductance of five plant species from a semiarid ecosystem. *Photosynthetica* **35**:399-410.
- Tezara, W., V. Mitchell, S. P. Driscoll, and D. W. Lawlor. 2002. Effects of water deficit and its interaction with CO<sub>2</sub> supply on the biochemistry and physiology of photosynthesis in sunflower. *Journal of Experimental Botany* **53**:1781-1791.
- Tezara, W., V. J. Mitchell, S. D. Driscoll, and D. W. Lawlor. 1999. Water stress inhibits plant photosynthesis by decreasing coupling factor and ATP. *Nature* **401**:914-917.
- Tucker, G. E., S. T. Lancaster, N. M. Gasparini, and R. L. Bras. 2001. The channel-hillslope integrated landscape development model. Pages 349-388 *in* R. S. Harmon and W. W. Doe, editors. *Landscape erosion and evolution modeling*. New York, Berlin.
- Turner, C. L., J. M. Blair, R. J. Scharz, and J. C. Neel. 1997. Soil N and plant responses to fire, topography, and supplemental N in tallgrass prairie. *Ecology* **78**:1832-1843.

- Turner, N. C., E. D. Schulze, and T. Gollan. 1985. The responses of stomata and leaf gas-exchange to vapor-pressure deficits and soil-water content .2. in the mesophytic herbaceous species *Helianthus-Annuus*. *Oecologia* **65**:348-355.
- Tuzet, A., A. Perrier, and R. Leuning. 2003. A coupled model of stomatal conductance, photosynthesis and transpiration. *Plant Cell and Environment* **26**:1097-1116.
- van der Tol, C., A. J. Dolman, M. J. Waterloo, and K. Raspor. 2007. Topography induced spatial variations in diurnal cycles of assimilation and latent heat of Mediterranean forest. *Biogeosciences* **4**:137-154.
- Vanmarcke, E. 1983. *Random fields: Analysis and synthesis*. MIT Press, Cambridge.
- Vico, G., and A. Porporato. 2008. Modelling C<sub>3</sub> and C<sub>4</sub> photosynthesis under water-stressed conditions. *Plant and Soil* **313**:187-203.
- Vico, G., and A. Porporato. 2009a. Irrigation with stochastic soil moisture. *Water Resources Research*.
- Vico, G., and A. Porporato. 2009b. Probabilistic description of topographic slope and aspect. *Journal of Geophysical Research* **114**:doi:10.1029/2008JF001038.
- Vitousek, P. M., and R. W. Howarth. 1991. Nitrogen limitation on land and in the sea - How can it occur. *Biogeochemistry* **13**:87-115.
- von Caemmerer, S. 2000. *Biochemical models of leaf photosynthesis*. CSIRO, Collingwood VIC.
- von Caemmerer, S., and R. T. Furbank. 1999. Modeling C<sub>4</sub> photosynthesis. Pages 173-211 *in* R. F. Sage and R. K. Monson, editors. *C<sub>4</sub> plant biology*. Academic Press, San Diego.
- Wang, S., W. J. Chen, and J. Cihlar. 2002. New calculation methods of diurnal distribution of solar radiation and its interception by canopy over complex terrain. *Ecological Modelling* **155**:191-204.
- Ward, J. K., D. T. Tissue, R. B. Thomas, and B. R. Strain. 1999. Comparative responses of model C<sub>3</sub> and C<sub>4</sub> plants to drought in low and elevated CO<sub>2</sub>. *Global Change Biology* **5**:857-867.

- Warren, C. R. 2008. Soil water deficits decrease the internal conductance to CO<sub>2</sub> transfer but atmospheric water deficits do not. *Journal of Experimental Botany* **59**:327-334.
- Warren, C. R., and M. A. Adams. 2006. Internal conductance does not scale with photosynthetic capacity: implications for carbon isotope discrimination and the economics of water and nitrogen use in photosynthesis. *Plant Cell and Environment* **29**:192-201.
- Weltzin, J. F., M. E. Loik, S. Schwinning, D. G. Williams, P. A. Fay, B. M. Haddad, J. Harte, T. E. Huxman, A. K. Knapp, G. H. Lin, W. T. Pockman, M. R. Shaw, E. E. Small, M. D. Smith, S. D. Smith, D. T. Tissue, and J. C. Zak. 2003. Assessing the response of terrestrial ecosystems to potential changes in precipitation. *BioScience* **53**:941-952.
- Western, A. W., R. B. Grayson, G. Bloschl, G. R. Willgoose, and T. A. McMahon. 1999. Observed spatial organization of soil moisture and its relation to terrain indices. *Water Resources Research* **35**:797-810.
- Wigmosta, M. S., L. W. Vail, and D. P. Lettenmaier. 1994. A Distributed Hydrology-Vegetation Model for Complex Terrain. *Water Resources Research* **30**:1665-1679.
- Willgoose, G., R. L. Bras, and I. Rodriguez-Iturbe. 1991. A coupled channel network growth and hillslope evolution model 1. Theory. *Water Resources Research* **27**:1671-1684.
- Williams, D. G., V. Gempko, A. Fravolini, S. W. Leavitt, G. W. Wall, B. A. Kimball, P. J. Pinter, R. LaMorte, and M. Ottman. 2001. Carbon isotope discrimination by *Sorghum bicolor* under CO<sub>2</sub> enrichment and drought. *New Phytologist* **150**:285-293.
- Wisser, D., S. Frohking, E. M. Douglas, B. M. Fekete, C. J. Vorosmarty, and A. H. Schumann. 2008. Global irrigation water demand: Variability and uncertainties arising from agricultural and climate data sets. *Geophysical Research Letters* **35**.
- Wolinsky, M. A., and L. F. Pratson. 2005. Constraints on landscape evolution from slope histograms. *Geology* **33**:477-480.
- Wong, S. C., I. R. Cowan, and G. D. Farquhar. 1979. Stomatal conductance correlates with photosynthetic capacity. *Nature* **282**:424-426.

- Wright, I. J., P. B. Reich, M. Westoby, D. D. Ackerly, Z. Baruch, F. Bongers, J. Cavender-Bares, T. Chapin, J. H. C. Cornelissen, M. Diemer, J. Flexas, E. Garnier, P. K. Groom, J. Gulias, K. Hikosaka, B. B. Lamont, T. Lee, W. Lee, C. Lusk, J. J. Midgley, M. L. Navas, U. Niinemets, J. Oleksyn, N. Osada, H. Poorter, P. Poot, L. Prior, V. I. Pyankov, C. Roumet, S. C. Thomas, M. G. Tjoelker, E. J. Veneklaas, and R. Villar. 2004. The worldwide leaf economics spectrum. *Nature* **428**:821-827.
- Wullschleger, S. D. 1993. Biochemical limitations to carbon assimilation in C(3) Plants - A retrospective analysis of the A/Ci curves from 109 species. *Journal of Experimental Botany* **44**:907-920.
- Zhan, X. W., Y. K. Xue, and G. J. Collatz. 2003. An analytical approach for estimating CO<sub>2</sub> and heat fluxes over the Amazonian region. *Ecological Modelling* **162**:97-117.
- Zhang, H. P., and T. Oweis. 1999. Water-yield relations and optimal irrigation scheduling of wheat in the Mediterranean region. *Agricultural Water Management* **38**:195-211.

## Biography

Giulia Vico was born in Torino (Italy) in 1979. She earned a MS degree in environmental engineering at Politecnico di Torino (Italy) on May 19<sup>th</sup>, 2004, graduating Magna Cum Laude with a dissertation on the role of hydrologic processes on soil moisture and vegetation dynamics. Under the supervision of Dr. A. Porporato at Duke University, Durham, NC, she is now investigating the impact of water stress on dynamics vegetation at different time scales, and the role of hydroclimatic forcing and topographic position.

## List of publications

### Papers in published on peer-reviewed international journals

Vico G., and A. Porporato (2009), Probabilistic description of topographic slope and aspect, *Journal of Geophysical Research – Earth Surface*, 114, F01011

Vico G., and A. Porporato (2008), Modelling C<sub>3</sub> and C<sub>4</sub> photosynthesis under-water stressed conditions, *Plant and Soil*, 313, 1-2, 187-203

Viola F., Daly E., Vico G., Cannarozzo M., and A. Porporato (2008), Transient soil-moisture dynamics and climate change in Mediterranean ecosystems, *Water Resources Research*, 44, 11, W11412

Porporato A., Vico G., and P.A. Fay (2006), Superstatistics of hydro-climatic fluctuations and interannual ecosystem productivity, *Geophysical Research Letters*, 33, L15402

### **Papers submitted or in preparation**

Vico G. and Porporato A., Irrigation with stochastic soil moisture, *Water Resources Research*, under revision

Vico G. and Porporato A., From rainfed agriculture to stress-avoidance irrigation: optimizing crop yield and net profit under intra- and inter-annual stochastic hydrologic variability, in preparation

Vico G., Manzoni S., Daly E., Katul G.G., and A. Porporato, Effect of soil water content on soil thermal conductivity under field conditions, in preparation

Manzoni S., Vico G., Katul G.G., Fay P.A., Polley W. and A. Porporato, Leaf economics under water stress, in preparation

### **Presentation at scientific meetings**

Vico G., Daly E., Manzoni S., and A. Porporato (2008), Effect of soil water content on soil thermal conductivity under field conditions *Eos Trans. AGU*, 89, 53, Fall Meet. Suppl., Abstract H13A-0877

Vico G., and A. Porporato (2007), Linking slope, aspect and river network probabilistic structures, *Eos Trans. AGU*, 88, 23, Jt. Assem. Suppl., Abstract H53D-04

Vico G., and A. Porporato (2005), Variability at multiple time scales and statistics of hydrologic extremes, *Eos Trans. AGU*, 86, 18, Jt. Assem. Suppl., Abstract H43A-06

Vico G., Porporato A., Katul G., Albertson J., and I. Rodriguez-Iturbe (2003), Strategies of plant water use under stochastic hydrologic conditions, *Eos Trans. AGU*, 84, 46, Fall Meet. Suppl., Abstract B52A-1033

### **Academic honors, professional activities and memberships**

2004: Magna Cum Laude distinction, Polytechnic of Turin, Italy.

Reviewer for peer-reviewed journals, including *Water Resources Research*, *Geophysical Research letters* and *Annals of Botany*.

Member of the American Geophysical Union (AGU) since 2005.